An aerial photograph of a beach. The top half of the image shows dark blue-green ocean water with white foam from breaking waves. The bottom half shows a wide, reddish-brown sandy beach. A semi-transparent dark grey box is overlaid on the top half of the image, containing text.

R.N.P. Hobbelen

Mapping sub-annual beach growth using terrestrial laser scanning

*A study on the application of terrestrial laser scanning on small scale beach
variability, to quantify beach resilience on sub-annual time scale*

Mapping sub-annual beach growth using terrestrial laser scanning

A study on the application of terrestrial laser scanning on small scale beach
variability, to quantify beach resilience on sub-annual time scale

By

R.N.P. Hobbelen

in partial fulfilment of the requirements for the degree of

Master of Science
in Civil Engineering

at the Delft University of Technology,
to be defended publicly on Thursday October 11, 2018.



Supervisor:	Dr. S. Vos	TU Delft
Thesis committee:	Prof. dr. ir. S.G.J. Aarninkhof,	TU Delft
	Dr. ir. S. de Vries,	TU Delft
	Dr. R.C. Lindenberg	TU Delft

This thesis is confidential and cannot be made public until October 2018.

An electronic version of this thesis is available at <http://repository.tudelft.nl/>.

Preface

This thesis is submitted in partial fulfilment of the requirements for the degree of Master of Science in Civil Engineering at Delft University of Technology. The research was carried for the Coastal Engineering section at Delft University of Technology.

I would like to thank my graduation committee for providing feedback and guidance throughout the composing of this thesis. In particular, I would like to thank Sander Vos for helping me improve this report, guiding me in my ideas and teaching me about laser scanners and the processing of laser scanner data. I would also like to thank Sierd de Vries for taking the time to look at my intermediate results and providing his ideas on how to improve them. I would like to thank Stefan Aarninkhof and Roderik Lindenbergh for their suggestions during our meetings.

Finally, I would like to thank my fellow students and friends, Lindert, Niek and Mario for providing me with support, criticism and suggestions during the writing of this report. A word of gratitude also goes out to my family, friends and girlfriend for supporting me all these years.

*Rik Hobbelen
Delft, September 2018*

Abstract

This thesis presents a case study on beach growth of a South Holland beach located slightly north of the Sand Motor over the course of six months, which was measured using a terrestrial laser scanner (TLS). This device was set up to continuously take hourly full coverage measurements of a one kilometre stretch of beach from a hotel rooftop.

As sea-levels rise, interest in the morphological processes that take place on beaches is growing, so that coastal safety can be continued to be guaranteed in the future. As a result, it becomes increasingly relevant to understand the transport of sediment towards the beach. Existing studies on the subject focus on timescales of years to decades, often making use of GPS measurements. However, no thorough research has been performed on sub-annual timescales in over a decade, leading to the following main research question for this thesis: How is beach volume growth distributed on sub-annual time scale, both in spatial and temporal dimensions?

To validate the data obtained by the TLS, an accuracy check was performed which proved the standard deviation of the measurements to be much smaller than the observed morphological change. A rotational instability of the scanning device was discovered and corrected, however a higher measurement accuracy could be obtained by developing a more detailed correction method. The applied correction method did however no longer allow for the study of smaller fluxes such as aeolian transport, as they are overruled by it. It was investigated how the raw 3D data obtained from the TLS should be processed to obtain a clean timeseries of cross-sections. A framework is presented that includes noise detection and removal, object filtering, interpolation and subsampling. Subsequently, timeseries of 132 cross-sections were extracted from the data by selecting a daily low tide scan for 132 days along 4 different transects.

The resulting timeseries clearly display morphological activity such as intertidal bar migration and storm erosion, and volumetric computations have displayed periods of beach growth. These periods generally occur between storms, during calm wind and wave conditions. The main driver for this growth is the onshore migration of intertidal bars. As bars enter the intertidal zone, they migrate onshore and grow, increasing the volume of the beach. A swash bar that formed high in the intertidal zone during neap tide was found to migrate at increased rate during the neap-spring tidal cycle and welded to the beach, as compared to a different bar which migrated during the spring-neap cycle. Following spring tide, the bar ceased onshore migration and an offshore expansion occurred. This offshore expansion had a great effect on the volumetric growth of the total beach profile and showcases the influence of tide in the migration of swash bars. However, due to the great number of factors that influence beach growth, only few significant correlations were found between beach volume changes and boundary conditions such as tide, and wave and wind forcing.

Over the entire research period, only limited growth of the beach has occurred (2.6 m³ over all transects). Periods of growth (up to 20 m³ in under a month) were followed by storms, which eroded the gained volume. No general linear trend in growth was observed, indicating the dominance of variability over trend on the regarded time scale. This result contradicts findings of studies that use monthly or yearly data. When regarding daily data for several months, the beach volume is very much influenced by bar migration and storm erosion which lead to much more variation in the volumetric signal.

Contents

Preface	3
Abstract	4
Contents	5
1. Introduction	7
1.1. Problem definition	8
1.2. Objective	9
1.3. Thesis outline	10
2. Theoretical background.....	11
2.1. Definitions.....	11
2.1.1. The coastal region	11
2.1.2. Spatial-temporal scale of beach growth	11
2.2. Beach erosion/accretion	12
2.3. Morphological processes	13
2.3.1. Aeolian transport	13
2.3.2. Swash zone sediment transport.....	13
2.3.3. Tide	15
2.3.4. Sand bar migration	16
2.3.5. Sediment armouring	17
2.4. Terrestrial laser scanning.....	18
2.4.1. Influences on laser scanner accuracy	20
2.5. Data processing techniques.....	21
2.5.1. Progressive morphological filtering	21
2.5.2. Noise detection.....	22
2.6. Data analysis techniques	23
2.6.1. Pearson's correlation	23
2.6.2. Linear least squares trend analysis.....	23
2.6.3. Fourier analysis	24
3. Approach	25
3.1. Data gathering and study area.....	25
3.1.1. Data gathering	25
3.1.2. Study area	28
3.2. Accuracy and consistency check	29
3.2.1. Laser specifications	29
3.2.2. Accuracy check	29
3.2.3. Consistency check.....	30
3.3. Data processing.....	31
3.4. Cross-section extraction	32
3.5. Analysis	32
4. Results.....	33

4.1.	Accuracy check	33
4.1.1.	Summary and cross-check	37
4.2.	Consistency check.....	39
4.3.	Data processing.....	41
4.4.	Cross-section extraction	45
4.5.	Analysis	46
4.5.1.	Envelope and variability	48
4.5.2.	Depth contour variation.....	50
4.5.3.	Beach volume distribution.....	52
4.5.4.	Results all transects.....	56
5.	Conclusions, discussion and recommendations	61
5.1.	Conclusions	61
5.2.	Discussion	62
5.3.	Recommendations.....	63
	Bibliography	66
	Appendix A: Individual analysis results transects 2-4.....	70
	Transect 2.....	70
	Transect 3.....	76
	Transect 4.....	82

1. Introduction

Like in many other coastal regions in the world, the Dutch shore is mainly protected by sandy beaches and dunes. Most of the Dutch population lives in the west of The Netherlands (CBS, 2018), where much of the land lies below mean sea level (AHN, 2017). Due to the rising sea-level, the interest in these natural defences has increased. Contrary to traditional (hard) engineering solutions, beaches and dunes provide a natural (soft) protection against the sea, whilst simultaneously supplying flora and fauna with habitat and humans with recreational areas. Soft protection measures often come in the form of sand nourishments. Beaches and dunes are however, dynamic as they are continuously subjected to various hydrodynamic and aeolian processes (Cowell et al, 2003). Currently, many engineering analyses focus on engineering time scales (years to decades) to predict coastal behaviour. Existing studies often make use of the JARKUS beach measurements that are performed once a year (Southgate, 2011). However, many processes that influence beaches act on much smaller time scales.

Beach growth on sub-annual time scale is a subject that has not been thoroughly researched in the last decade. With the increasing amount of 'soft' shoreline protections in the form of sand nourishments, it's becoming more and more relevant to develop an increased understanding of the transport of sediment towards the beach. Existing studies are mainly based on relatively few measurements, usually obtained by GPS over several days, that do not provide 3D data. A promising new technique is found in terrestrial laser scanning. Using such a scanner, continuous, full coverage measurements can be taken of a stretch of beach of up to 1 km. length in longshore direction. 3D elevation data can be obtained on hourly time scale, allowing for a much greater level of detail in beach growth studies. Since growth rates can be closely monitored, changes in these rates can be attempted to be linked to variability in the known main sediment transport drivers: waves, tide and wind.

In an attempt to supplement the knowledge on long term shoreline predictions, the CoastScan project was set up. This project will especially focus on the (aeolian) dune ward transport of sand and recovery of the coast after storms (Vos et al, 2017), which are currently challenging to predict. To this cause, a terrestrial laser scanner (TLS) has been set up to measure a stretch of coastline near Kijkduin, The Netherlands. The TLS has taken hourly scans of the beach and dunes for about 130 days, with an accuracy of around 1-2 cm. This level of accuracy allows the smaller time scale processes to be captured, which has previously been impossible with the yearly LIDAR measurements performed by the Dutch government (Southgate, 2011). The TLS data will have to be checked for consistency and accuracy, to guarantee correct analysis results. This also includes data processing, which can help remove non-terrain disturbances (such as pedestrians) in the measurement results. The data can then be used to quantify volumetric change on time scales of down to hourly, so that morphological change can be studied.

In this thesis, the data obtained by the TLS is processed to investigate the growth of the beach over a period of several months, during the stormy season. The aim is to investigate the feasibility of this application, develop a framework to process the TLS data and quantify morphological change to obtain new insights in the recovery mechanisms and time scales of the coast.

1.1. Problem definition

Coastal behaviour is subject to various processes (Cowell et al, 2003). Some of the larger scale processes include for example sea-level rise, shore profile change and beach rotation. These processes develop on both a large spatial and temporal scale and can therefore be monitored using for example yearly measurement data such as JARKUS (Southgate, 2011). Some of the processes that cannot be investigated in this fashion include storm erosion and recovery. These processes act on much smaller spatial and temporal scales, that cannot fully be captured using yearly measurement data. The lack of understanding of the effects of these processes makes it challenging to accurately predict coastal behaviour (Vos et al, 2017). This prediction is of importance to guarantee coastal safety in the future, and to be able to accurately act if this safety cannot be guaranteed. The safety level is greatly influenced by storm erosion (Vellinga, 1982), and the coast's natural ability to recover from this erosion through beach growth. This growth mainly takes place through dune-ward aeolian transport of sand that is washed ashore (de Vries, 2013), which is a flux in the order of mm-cm (depending on the considered temporal scale). This, combined with the fact that post storm recovery is very much dependent on local 3D morphology, makes measurement by LIDAR or satellite, both methods that are used frequently, unsuitable, since the spatial and/or temporal resolution of these techniques are too large to analyse this problem (Vosselman et al, 2010) and do not by default provide a 3D image.

The importance of post-storm beach growth is stressed by Castelle et al (2017), which states that relatively little quantitative research has been performed on the subject. Perpetual sediment imbalance caused by storms and following recovery process drives long-term shoreline change. Therefore, a quantification of this process is of relevance to predict this change and accompanying safety levels. Full recovery after a stormy season is slow and can take many years, however initial growth can occur rather fast, sometimes already in the waning phase of the storm. It is therefore of importance to study this process on small temporal scales, with sufficient spatial accuracy to achieve this.

According to Houser (2009), the ability to predict spatial-temporal behaviour of beach-dune systems is still quite limited. An argument that is presented to support this statement is the lack of understanding of transport potential and supply synchronization. It was found that dune evolution strongly correlated to sand bar migration towards the shore. However, various wind model studies simply assume delivery of sediment to the beach, to then quantify aeolian transport. Instead of assuming an unlimited supply of sediment available to be transported by wind, Houser (2009) argues that variations in beach morphology should be considered that define sediment availability. Houser's hypothesis about the link between transport potential and supply synchronization has been proven by multiple articles, such as de Vries (2013), proving that aeolian transport can indeed be limited by supply.

Houser et al (2008) describes the lack of understanding of growth variation drivers. Variations in growth rates of shorelines have been documented, yet the mechanisms that are responsible for these variations have not been identified. Boundary conditions such as wave and wind properties, in combination with sediment availability could be responsible. However, bathymetry and vegetation density are also mentioned as a potential cause of variation.

Concluding from the above text, the main problem is the fact that current knowledge on post-storm beach growth is insufficient and cannot be studied using currently available data obtained by widely used land surveying techniques. The spatial and temporal resolutions of these techniques are not suitable to accurately study storm erosion and recovery. This negatively affects the accuracy of coastal safety forecasts and the effectiveness of sand nourishments.

This thesis aims to further this knowledge by researching beach growth on sub-annual time scale, and simultaneously investigate how data obtained from a TLS can contribute to this cause. By analysing the change in beach volume with daily frequency for nearly six months, an understanding will be developed about the time scale of the growth process, as well as its spatial-temporal distribution. The problem will mainly be analysed through beach volume monitoring after reset events (storms). This monitoring will be done using the data obtained by the TLS, through the reconstruction of the local terrain. The change in volume will then be attempted to be linked to various boundary conditions (such as wave conditions), that are known to be relevant in calm periods after storms.

1.2. Objective

This thesis aims to develop a better understanding of beach growth on sub-annual time scale by looking to achieve three main goals: validation of the application of the TLS on this subject (1), quantification of volumetric change in the dynamic intertidal zone (2), and linking the volumetric change in the intertidal zone to volumetric change of the backshore and foredune (3). Such understanding can further aid the development of accurate nourishment plans, thereby making a positive contribution towards coastal safety. The data obtained by the TLS is quite unique for this application. Its applicability for the mapping of beach variability has already been shown in Vos et al, 2017, however there is currently only one other project in the world where a sandy beach is continuously being monitored using a TLS (Brodie et al, 2012). In this thesis, a framework to process the TLS data for this application will therefore be developed.

The main research question this thesis will aim to answer is as follows:

- **How is beach volume growth distributed on sub-annual time scale, both in spatial and temporal dimensions?**

To help answer this main research question, the following sub questions will be researched:

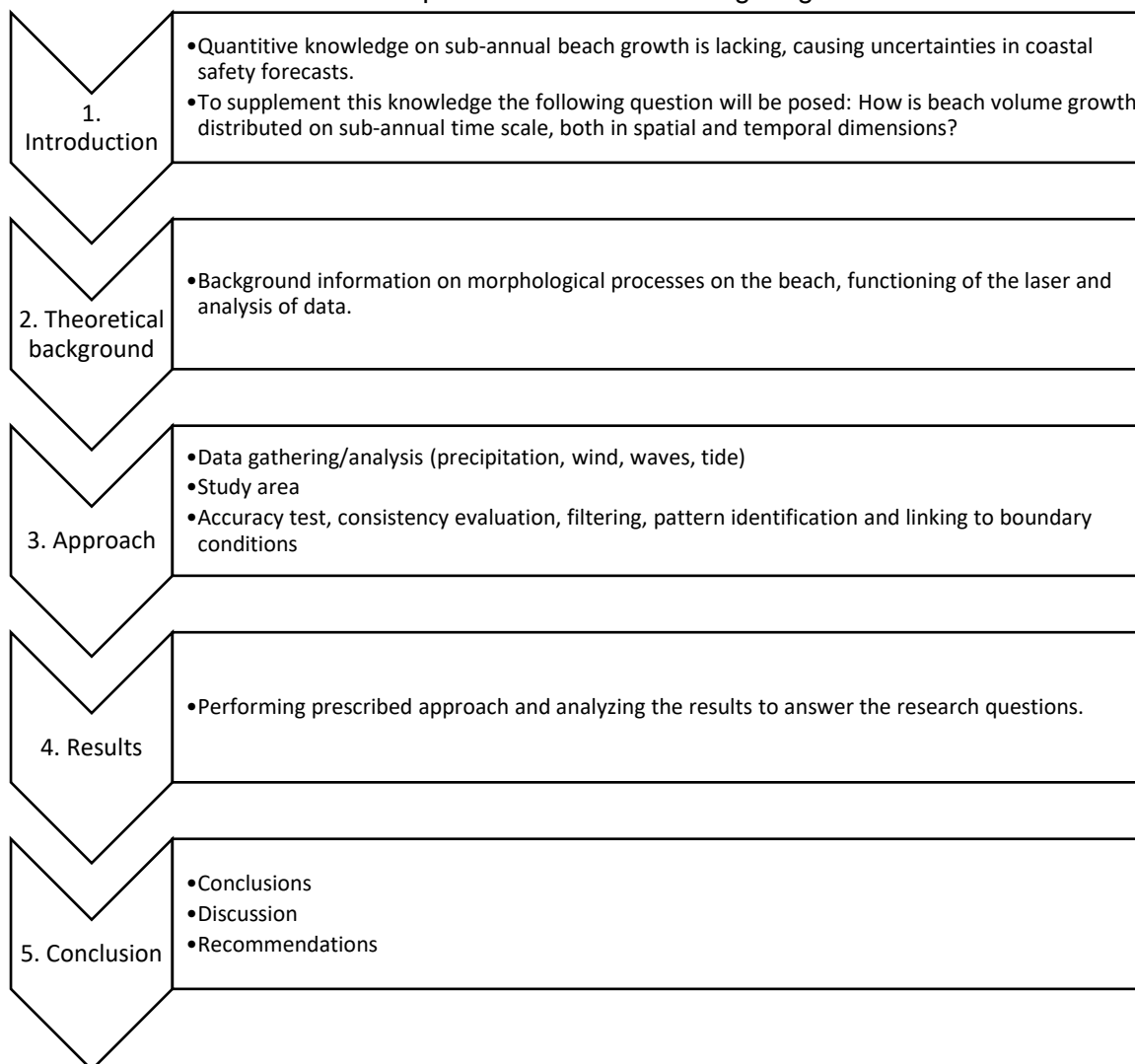
- How should the data obtained from the terrestrial laser scanner be processed to detect morphological indicators?
- Can patterns in beach variability be identified and if so, how do they contribute to beach growth?
- What is the relative importance of waves, tide and aeolian processes when regarding beach growth?

The first sub question will provide a framework for the processing of the data, so that it becomes usable for the intended research method that will be described in chapter 3, and possibly for future research of this kind of data. Correct processing of the data is necessary to be able to accurately answer the main research question. The second sub question will attempt to identify patterns in

sources and sinks of sediment within the research area, if they are at all present. By identifying where transported sand originated from and where it's going, insight will be gained in the growth process. To further this understanding even more, the uncovered patterns will be attempted to be matched to boundary conditions in the final sub question. Answering this question will lead to insight in the conditions that influence beach growth on sub-annual time scale. After answering these sub questions, the main research question will be answered, and the objectives of this thesis accomplished.

1.3. Thesis outline

The main outline of this thesis is presented in the following diagram:



2. Theoretical background

This chapter presents a literature study on various subjects relevant to this research.

2.1. Definitions

This paragraph presents the definitions used for various subjects throughout this research.

2.1.1. The coastal region

The coastal region is made up out of various, universal elements (Masselink & Gehrels, 2014). Some relevant elements have been graphically represented in Figure 2-1.

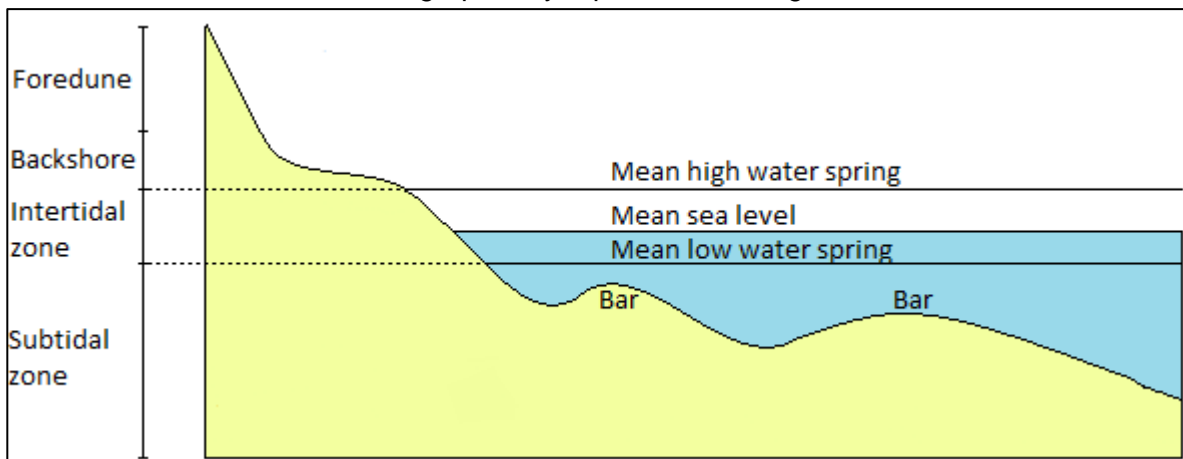


Figure 2-1: Graphical representation of coastal region. Adapted from Masselink & Gehrels, 2014.

The area that is permanently submerged is called the subtidal zone. The area between mean high-water spring (MHWS) and mean low-water spring (MLWS) is called the intertidal zone and is alternately submerged/emerged as the tide rises and falls. The area above the intertidal zone reaches from MHWS until the fore-dune and is called the backshore. Though there is no general definition for the transition point between backshore and fore-dune, the position for the Dutch dune foot is nowadays often assumed to be at +3 meters above mean sea level (MSL) (Ruessink & Jeuken, 2002). A berm (nearly horizontal plateau) may be present on backshore or upper intertidal zone. Another zone of interest is called the swash zone. This is the zone that is influenced by wave runup and backwash and is located around the sea level. It therefore moves up and down with the sea level rather than being fixed to one location. The TLS in its current setup can only consistently measure land elevation of the dry part of the beach. It cannot penetrate water; therefore, the subtidal zone cannot be measured. The part of the beach that will be analysed will reach from a point in the intertidal zone that is consistently measured in the data, which can only be measured during ebb, to a boundary that is set on the fore-dune.

2.1.2. Spatial-temporal scale of beach growth

Cowell et al (2003) describes the temporal scale of storm erosion and recovery to be of the order hours-months, and its spatial scale in the order of 1 mm-100 m. Since this thesis focuses on sub-annual beach growth effects, only processes that also act on these scales will be regarded. This means not all processes will be considered, as their spatial-temporal scales do not all match the one of storm erosion. The analysis of the data will therefore also be executed at these scales.

2.2. Beach erosion/accretion

Due to the dynamic environment they are in, beaches constantly undergo volumetric changes (Davidson-Arnott & Law, 1990). When boundary conditions such as wave action are unfavourable and sediment supply is limited, the coast erodes. When the conditions are favourable, and supply is plentiful, the coast accretes. Generally, beach volumes reach an annual maximum in summer when weather conditions are milder than in winter. The more severe winter storms cause surges and are accompanied by more energetic wave and wind conditions. These lead to erosion of the beach, decreasing its volume and increasing the beach slope (Vellinga, 1982). The sand that is eroded from the beach is not necessarily lost, the majority is stored on the beach itself (see Figure 2-2), a significant portion of it between the dune foot and the low water level. During calmer conditions, it is then slowly transported onshore again.

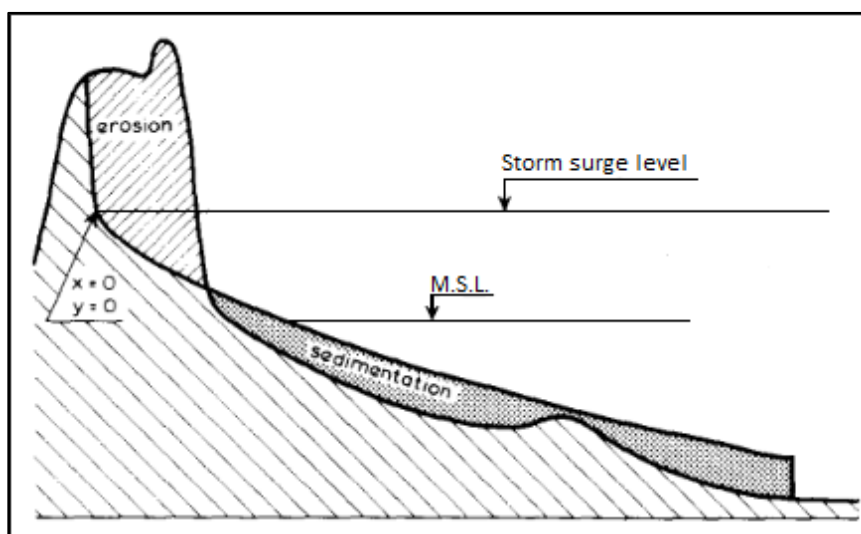


Figure 2-2: Redistribution of sand on the beach due to storm surges. From Vellinga, 1982.

Several studies have described and researched the recovery process of beaches (e.g. Suarez et al, 2012; Houser, 2009; Houser et al, 2015). The recovery process starts immediately after the storm. It can take several weeks to years for a beach to fully recover from severe storm erosion. The first stage of recovery is marked by the onshore migration of the innermost submerged sandbar. The bar eventually welds to the beach, driven by waves shoaling over it (Hsu et al, 2006). This welding of the bar to the beach is the main provider of sediment supply to the beach. The bar attaches itself to the backshore, extending it. It allows for more sediment to become available for aeolian transport towards the dune face. According to Houser (2009), welding is the primary source of sediment for the beach. Onshore directed winds transport the dry sand from the beach until the sand becomes trapped (by vegetation) in the dunes (van der Wal, 1999), restoring their volume. The transport is optimal for beaches with low gradients, wide beaches and surf zones, and high wave energy. These beaches allow for the development of the largest foredunes. A factor that greatly influences the aeolian transport is soil moisture content (Davidson-Arnott et al, 2008). Wet sediment cannot be transported by the wind, and wet spots on the beach resulting from local depressions act as sediment traps (Wiggs et al, 2004). The moisture content is influenced by the water level (tide) and precipitation, both wetting the sand and raising the water table. If the sand cannot dry between two high tides, dune ward aeolian transport cannot be initiated since the sand in the intertidal zone is the only supply of sediment to the beach.

The recovery process of a beach after a storm is also described in Morton et al (1994). Recovery starts immediately after the high energy storm conditions start to fade. Sand bar systems will start migrating onshore. This process can take anywhere from several months to a year. The berm volume will restore to its pre-storm values, increasing the beach slope. This initial recovery primarily concerns the onshore transport of sand from sand bars that were created during the storm. Due to the large influence of marine processes on this migration, the initial recovery takes place relatively fast. The water line will shift back to its original position due to the large deposits of sand in the intertidal zone. Erosion that has taken place higher up in the profile is not yet recovered. Recovery of the backshore only happens in a later stage, where aeolian transport plays a significant role.

2.3. Morphological processes

This paragraph will focus on the morphological processes that act on the same time scale as storm erosion/recovery and thereby influence it. These are the following: aeolian transport, swash zone sediment transport, tide, sand bar migration and sediment armouring.

2.3.1. Aeolian transport

Aeolian transport plays a major role in beach growth. It is the mechanism that transports sand that is washed ashore towards the dunes (van der Wal, 1999), and is thereby the only mechanism that leads to accretion of the supratidal zone. Onshore directed winds set sand particles in motion due to their uplifting force (Bauer & Davidson-Arnott, 2003).

There have been several researchers who have derived expressions for the transport rates of sand by wind. Perhaps the most widely used, well-known and one of the earliest, is Bagnold (1941). Bagnold proposed a relation to estimate transport rates based on sediment properties. The first to introduce a threshold shear velocity to this process was Kawamura (1951). The threshold velocity makes it so that there is no transport at lower velocities. When the threshold shear stress is reached, sand particles are set in motion.

2.3.2. Swash zone sediment transport

The swash zone is the region on the beach face that is not permanently submerged, but alternately exposed and covered by runup and backwash caused by incoming waves (Masselink & Puleo, 2006). Flow in the swash zone is highly dynamic and very turbulent, leading to relatively large sediment transport rates. Due to these high transport rates and the transitional location of the zone between water and land, it plays a vital role in shoreline change (Masselink & Hughes, 1998). Swash erosion and accretion contribute to the shaping of the beach. A substantial portion of longshore sediment transport also occurs in the swash zone. On reflective and calm beaches, the swash motion time scale is in the order of seconds. On highly energetic and dissipative beaches, the time scale can go up to minutes. Various modes of transport occur in this region, such as suspended load, bed load and sheet flow. The high variety in which swash zone motion can occur makes it a rather difficult mechanism to perform measurements on (Masselink & Puleo, 2006).

A typical swash cycle is described in Masselink & Puleo, 2006 and Elfrink & Baldock, 2002 (see Figure 2-3). A bore approaches the beach and collapses when it meets the beach face. The pressure and turbulence generated by the collapse accelerate the water up the beach face (uprush or runup). During this uprush, the velocity is directed onshore over the entire depth of the uprush

layer. As the uprush pushes over the beach face, depending on the saturation levels of the beach, water may start infiltrating the soil below. The uprush will eventually be slowed down to a halt by friction and gravity. As this maximum landward extension is reached, the lower swash layer velocity will have already started to reverse, thinning the swash layer as a result. The upper swash layer will now also accelerate back down the slope, and possibly still infiltrate the soil. As the fluid flows back offshore, it will then start to interact with the next incoming bore and decelerate, possibly forming a retrogressive bore in the process due to the still incoming retreating swash layer. Due to the special shape the swash runup takes, as a thin sheet with uniform flow direction, the classic concept of water particles having orbital trajectories no longer applies. Besides swash resulting from incoming bores, another mechanism that causes swash runup exists. Swash runup can also be the result of low-frequency standing motions (Masselink & Puleo, 2006).

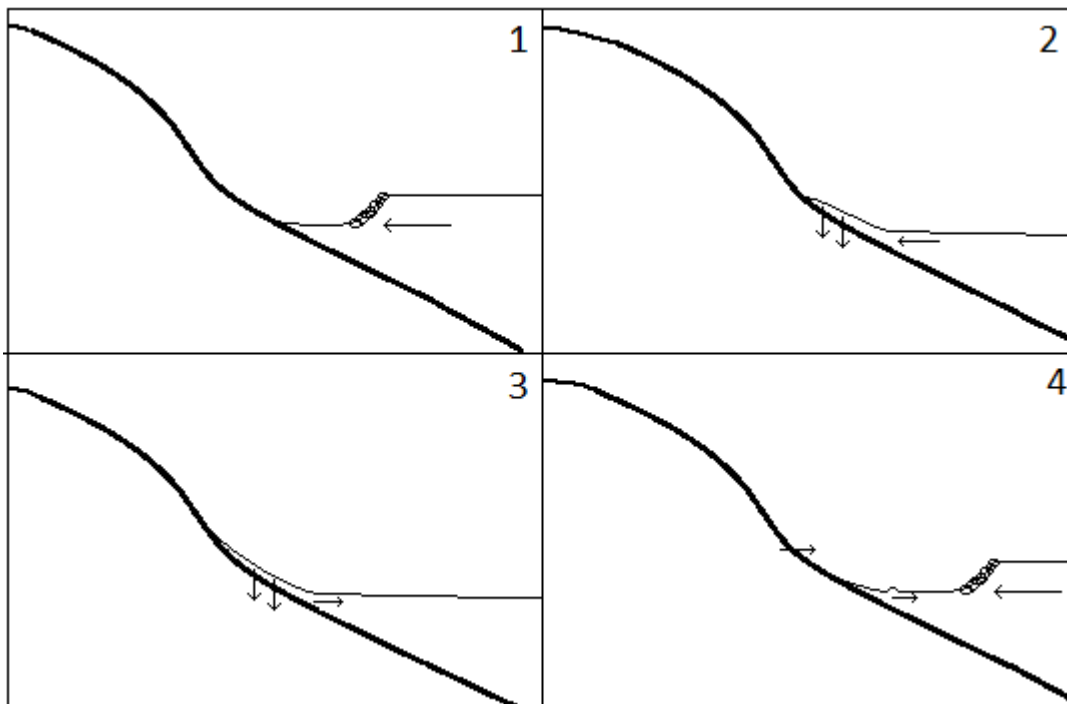


Figure 2-3: Schematic of swash cycle, adapted from Masselink & Puleo, 2006. Thick curve indicates foreshore surface. Thin curve indicates water surface. Arrows indicate flow direction.

The response of a beach to swash sediment transport depends on, amongst other things, the steepness of the beach face (Masselink & Puleo, 2006). This steepness is related to the natural equilibrium slope of the beach. Accretion occurs when the current slope is gentler than the equilibrium slope, and vice versa. The slope increases due to accretion and decreases if erosion occurs, largely due to the influence of gravity. If the slope is too steep, more sediment is eroded by the backwash than is accreted by the runup. Similarly, when the slope is below the equilibrium slope, the runup accretes more sand than the backwash can erode. Morphological change due to swash will not halt until the equilibrium situation is reached. Beach face erosion that occurs during storms though, is generally not the result of swash interactions. Surf zone processes dominate this situation. Due to increased storm surge water levels these processes now operate on the part of the beach that has already been shaped by swash motion. During major storm events however, the beach face is completely submerged and relatively unaffected by the waves.

2.3.3. Tide

The tide plays a vital role when it comes to beach morphology. Whereas many studies focus on the influence of either waves or tide individually, the interaction between the two is crucial (Masselink & Short, 1993). In dated studies, tide used to play an indirect role in sediment transport. The only function it had was to alternately submerge and expose a section of the beach. By submerging a section of the beach, it would allow surf zone processes into this region and transport sediment. Nowadays, it is recognised that tide plays a more significant role. Not only does it submerge/expose sections of the beach, it also shifts the locations of the surf zone, shoaling zone and swash zone. By doing so, the degree to which different sections of the beach are exposed to these different processes is dictated by the tide.

The tidal range, and with it the amount of time different sections of the beach are exposed to different surf zone processes, varies on multiple time scales. If one considers one location for a month, the tide will vary during this month due to the change in orientation between primarily the earth, sun and moon (Bosboom & Stive, 2015). Twice a month, the earth, sun and moon will line up, causing a spring tide with an increased tidal amplitude. Also, twice a month, the earth, sun and moon will be out of phase and a so-called neap tide occurs, with decreased tidal ranges (see Figure 2-4). In between spring and neap tide, the tidal amplitude will increase/decrease towards the next spring/neap tide. The Dutch coasts experience two tidal cycles per day (two high water, two low waters). A daily inequality can however be observed between these two cycles. One high water will have a higher tidal amplitude than the other, due to the difference in declination of the sun. Twice a year, in March and September, the sun's declination is zero, resulting in maximum tidal levels for semi-diurnal tides. In summer on the northern hemisphere, the declination reaches a maximum. The declination is minimum in winter. The solar daily inequality therefore has a cycle time of one year. A lunar daily inequality also exists, with a cycle time of 27.3 days.

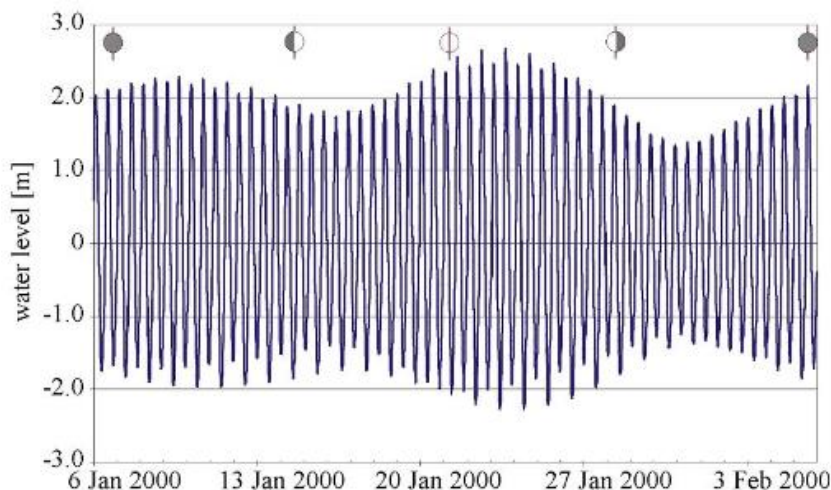


Figure 2-4: Tidal variations with spring and neap tide, from Bosboom & Stive (2015).

The tidal range and its synchronization with wave conditions is crucial when it comes to sand bar migration. The degree to which a sand bar is exposed to waves is dictated by the local water depth. This local water depth is in turn determined by the tidal range. An onshore migrating bar will move slower when it is in deep water, than it would in shallower water. On top of this, the tide itself also generates several three-dimensional flows in the nearshore zone (Masselink & Short, 1993). A

shore parallel flow can be generated on beaches with large tidal ranges, that influences sediment transport in the subtidal and intertidal zones. Bosboom & Stive (2015) states that the tidal wave moves from the south to the north along the Dutch coast, indicating such a flow. Furthermore, in shallow water ($O(10\text{ m})$), these velocities can be around 1 m/s and can therefore play a significant role in longshore transport. This effect is strongest when the tidal current flows in the same direction as the wave-induced current.

Generally, tidal ranges around the world can be classified into three groups: micro-tide (mean spring tidal range $< 2\text{ m}$), meso-tide (mean spring tidal range 2-4 m) and macro-tide (mean spring tidal range $> 4\text{ m}$) (Bosboom & Stive, 2015). The Dutch coast falls into the second category. The corresponding tidal range then determines the exposure time of the beach to the beforementioned surf zone processes. In macro-tidal zones for example, the influence of shoaling waves may completely outweigh the influence of other processes (Masselink & Short, 1993). If mean wave conditions are small however, the tide will dominate the sediment transport. Tide dominated coasts show wide, low-gradient tidal flats consisting of fine sediment, whereas wave dominated coasts are much steeper and coarser.

2.3.4. Sand bar migration

Sand bars are a significant source of sediment for aeolian transport (Houser, 2009). During a storm, substantial amounts of sediment that were eroded from the beach (and dunes) are deposited in the form of bars, on the subtidal part of the beach. When the storm ends, water levels drop. At the location of the newly formed bar, the water depth will now be reduced as compared to the pre-storm water depth. This local reduction in water depth influences the shoaling process of waves (Hsu et al, 2006), and they become more skewed. The waves pitch forward, creating a steeper front and gentler rear face (see Figure 2-5). As these asymmetric waves pass over the bar, the rapid change in orbital velocity caused by the passing wave causes a fluid acceleration that is onshore directed. This fluid acceleration is maximum near the crest (Hoefel & Elgar, 2003), and in turn sets the sediment into motion and transports it in the wave direction. In this fashion, the bar moves onshore until it reaches the beach, where it will weld to it, extending it significantly. Sand bars do not always move onshore during calm conditions. If the bar is at a location where the water depth is still too high compared to the wave height, the bar will not migrate.

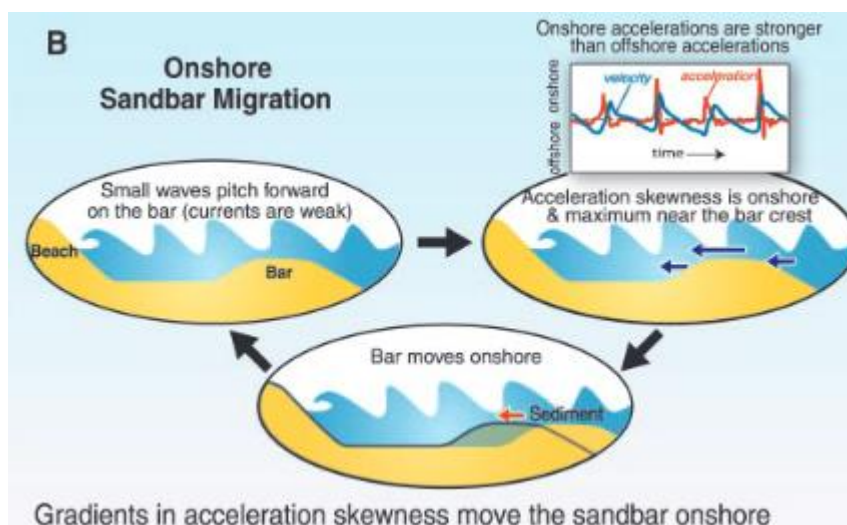


Figure 2-5: Schematic of onshore bar migration from Hoefel & Elgar, 2003.

When subtidal bars migrate onshore they can reach the intertidal zone, where they will turn into swash bars (Houser et al, 2006). In the intertidal zone, the rate (and direction) of migration primarily depends on the local wave height and water depth. When the crest of the bar emerges from the water, the migration of the bar will become dictated by swash. Swash motion will erode sediment from the seaward face of the bar, and deposit it on the landward face of the bar as it overtops it, leading to a net onshore movement. Swash bars can also form around the high tide level, where swash motion deposits sand on the beach face (Kroon & Masselink, 2002). Furthermore, a coupling of swash bar migration and water level variation caused by the neap-spring tidal cycle is suggested. The location of the surf zone, which is governed by the tide, plays a dominant role in the migration of swash bars. Onshore migration of these bars was found to coincide with the rising tide and cease during the falling tide. As the bar is exposed to surf zone effects during rising tide, the bar migrates onshore through erosion of the seaward face and deposition on the landward face. As the bar migrates, the tidal range will increase daily in the neap to spring tidal cycle, shifting the location of the surf zone onshore. In this period, swash bars are found to migrate with the increasing tidal range, following the surf zone. During the spring to neap cycle, migration of these bars then halts but accretion continues as swash effects and surf zone bores dominate.

Onshore bar migration is usually observed when mean currents are relatively weak and wave energy is moderate. Hsu et al (2006) discusses the onshore migration of a sand bar near Duck, North Carolina. The sand bar moved 25 m onshore, in a time span of just 5 days. This goes to show how fast sand bars can migrate. The process usually takes longer than this, and onshore migration is set back by the occurrence of new storms. In this case, the bars will reduce wave energy during the storm, which in turn reduces beach erosion (Houser, 2009). To this day, it remains unclear how exactly sand bar welding and aeolian transport are synchronized (Houser, 2009). Generally, transport capacity of wind is higher with higher velocity. However, with higher wind velocity often come elevated water levels, submerging the welding bar. This would not allow for dune accretion by aeolian transport to occur.

2.3.5. Sediment armouring

Sediment armouring is the formation of a top layer in sediment, that increases the threshold of motion. By trapping sediment containing finer grains under this top layer, sediment supply for transport is limited. Sediment armouring can occur in numerous ways. When considering sediment transport by flow of water, so-called bed armouring can occur (Wiberg et al, 1994). The average flow velocity will transport the finer grains but is unable to transport heavier grains. After all fine grains have been transported away from a location with a mixed grain size distribution, a top layer of heavy grains remains, that cannot be transported by mean flow. This layer will prevent the potential transport of finer grains underneath the layer. This process will however not occur in the intertidal zone, which is alternately forced by wind and flow. The energetic conditions in this area during submergence stir up and mix the sediment (de Vries, 2013).

Sediment armouring can also occur due to aeolian transport (Iversen and Rasmussen, 1994). When the wind has transported all fine grains that were available on a sandy surface, the heavier grains which cannot be transported will remain on the surface and trap underlying sediment. This is often observed on the upper beach, which is not a source of sediment but merely stores sediment that is transported from the intertidal zone. When aeolian sediment supply from the intertidal zone is

stopped (e.g. due to high tide), fine grains blow out of the upper beach, leaving the heavier particles behind.

2.4. Terrestrial laser scanning

The CoastScan project makes use of a Riegl-VZ2000 laser scanner that is mounted on a frame (Vos et al, 2017). During the performed measurements, the laser was never moved from its original location and continuously scanned the same section of beach. Such a setup is also referred to as Permanent Laser Scanning (PLS). The laser that is used makes use of single pulse ranging and time of flight measurement (Riegl Laser Measurement systems GmbH, 2017). A pulse is sent out by the laser, and the reflection of that pulse is captured by the scanner as well (see Figure 2-6). Using the time gap between sending and receiving the pulse, a distance can be computed. By measuring the strength of the reflected signal, soil properties can be derived. According to the specifications of the laser, the accuracy is 5 mm with a precision of 3 mm, with a maximum range of up to 2500 m.

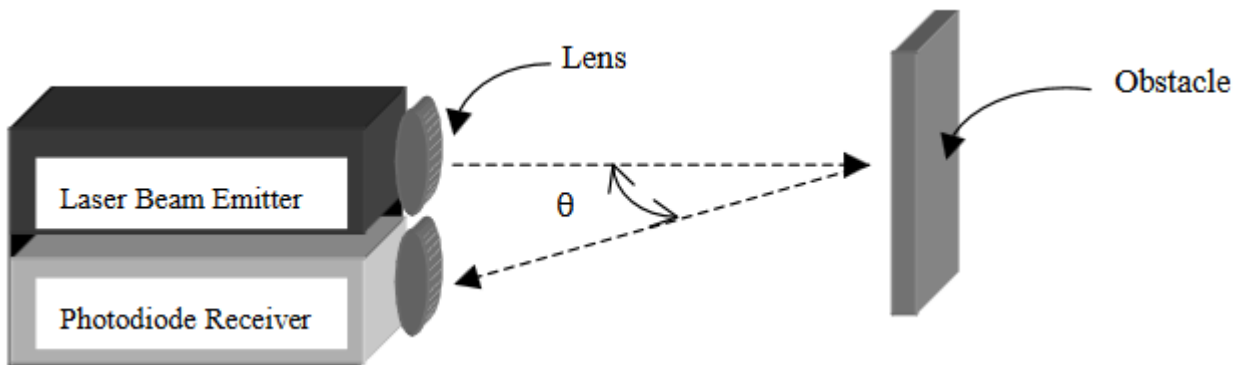


Figure 2-6: Functioning of laser scanner. From Angelopoulou & Wright, 1999.

Light emitted by laser (Light Amplification by Stimulated Emission of Radiation) is, compared to natural light sources, much more spatially coherent (Vosselman et al, 2010). This coherence allows for a focussed surface projection. Several mechanisms can be distinguished (gas, solid-state and semiconductor) for the generation of the light pulse (Angelopoulou & Wright, 1999). Light is generated by sending a photon into a high energy atom, which then releases its energy in the form of light and sets a cascade into motion causing other high energy atoms to release their energy as well.

The generated light then passes through a lens, through a transmission medium (air, water, vacuum) and onto the object that is to be scanned. The reflected signal then also passes through a lens and into a photodetection mechanism (Vosselman et al, 2010). Because the medium can vary over the distance that is measured, corrections can be made to the refraction to account for these variations. For example, when measuring downwards from an elevated position, temperature differences between point of measurement and laser location may influence the received signal. Different materials and object shapes lead to different reflectivity. By making use of this characteristic, distinction between different materials and objects can be made from reflectivity maps.

The Riegl-VZ2000 laser makes use of mirrors and a rotating base to produce a 3D scan of its environment (Riegl Laser Measurement systems GmbH, 2017). Various properties of the received signal can be analysed, but in this case the angle of the incoming signal and the time lag are extracted, as well as the reflectivity. The angle and time lag can then be used to compute a distance for all measured points, as is demonstrated in Lindenbergh et al, 2011. The resulting data format is composed by a 3D point cloud, which includes the reflectivity measured for all points.

By interpreting the signal shape that is received by the scanner after reflection, additional information can be obtained (Hofton et al, 2000). The shape that returns to the scanner contains information from its interacting with the surface it reflected off. The signal can have a shape similar to the single-mode shape of the outgoing signal, but it can also be multi-modal. A multi-modal signal contains several single-modes that each represent a form of reflection from the surface. Single-mode return signals are often found when analysing bare soil or water bodies. Multi-modal signals often indicate the presence of vegetation. To separate underlying terrain from vegetation, a multi-modal signal can be decomposed to identify the single-mode (Gaussian) signals that are present. Therefore, by decomposing a multi-modal signal, extra information on the terrain properties is gained.

The laser device itself does not by default know its position in space. Therefore, reflectors are set up around the device. The position of these reflectors is determined by GPS. The laser scanner uses these reflectors and their known positions to orientate itself in space with an accuracy of 3-5 cm, allowing for coordinated measurements (Vos et al, 2017).

Two main types of errors exist in terrestrial laser scanning (Vosselman et al, 2010): individual errors and systematic errors. Individual errors are often seen in the data as noise and can be eliminated using statistical outlier removal tools. Such tools remove points that are further than a certain distance (e.g. 1 standard deviation) from the mean. Systematic errors originate from product imperfections or position offset. Product imperfections arise from the manufacturer not being able to realise the theoretical design in which all 3 axes (X, Y, Z) of the scanner are perfectly orthogonal to each other. Position offset errors arise from inaccuracies in the orientation process of the laser using the reflectors around it. If the laser places itself at a false location, all measurements will be erroneously computed relative to this location. It is also possible for the scanning device to have an error in its levelling, creating shifted measurements.

Before a change map can be made, the data will have to be cleaned. Often, noise from external sources such as rain or fog obstruct the view of the laser scanner. Objects on the terrain also interfere with a terrain map. To eliminate these elements from the data, the data will need to be filtered to separate terrain points from off-terrain points. This process will allow off-terrain objects such as vegetation or pedestrians to be removed from the data. Several different filtering methods are available.

Scan data obtained from a laser scanner can be relatively large and processing these large datafiles can be quite a chore. Downsizing of data is therefore preferred. A way to do this is to subsample the data to a grid and compare the spatial data at various times on these fixed grid points (Lindenbergh et al, 2011). Data reduction can be done efficiently, as to maintain a high level of accuracy.

2.4.1. Influences on laser scanner accuracy

In real life situations, there are a multitude of factors that can affect the scan accuracy. As the producer already mentioned, bright sunlight is one of these factors (Riegl Laser Measurement systems GmbH, 2017). The ideal conditions the producer has used for the specifications of the laser are hardly ever present in realistic measuring locations. According to Soudarissanane et al (2011), four main factors exist that influence scan quality: scan geometry, instrument mechanism, atmospheric conditions and object surface properties. These four factors will be examined further to investigate which are applicable to this research.

Scan geometry depends on the orientation and range of the measured surface relative to the laser scanner. An effect with large influence on measurement accuracy is the so-called angle of incidence effect (Soudarissanane et al, 2011). In the producer's ideal conditions, the angle of incidence was 90° . This ensures that as much of the reflected laser beams are received by the scanner as possible. In practice this is rarely the case. In its application in the CoastScan project, the angle of incidence is much lower than 90° as the beach is relatively horizontal and is being measured from the roof of a hotel behind the dunes. When a laser beam hits an object, depending on the objects material properties and angle of incidence, the light is scattered in several directions. Only part of the scattered reflections is reflected back towards the scanner and captured. When the captured energy exceeds a threshold energy level, an image can be created of the object. In the application in the CoastScan project, calm, flat water is therefore hardly measured, as it scatters too much of the incoming laser beam to get an accurate reflection. Some reflections are however obtained from incoming waves and bores. With increasing angle of incidence (increasing defined as moving away from 90° in either direction), scatter increases and energy levels decrease due to footprint deformation. When a laser beam hits a flat perpendicular object, its footprint is a circle. If the flat object is placed under an angle, the footprint becomes an oval. In other words, the footprint is stretched. The incoming energy that is available for reflection is therefore spread over a larger surface, leading to weaker reflections. This effect is further enhanced by non-flat surfaces and increasing distance from the scanner. The latter is responsible for decreasing point density with increasing range. Measurement accuracy decreases linearly with increasing range (Vosselman et al, 2010). An additional effect that occurs due to footprint deformation, especially when measuring objects over a large distance, is that the footprint of the laser beam can be (much) wider than the object that is measured. When this happens, part of the laser beam will hit the object and reflect, and part of the laser beam will continue travelling past the object and reflect off of an object behind it. The resulting reflection is however averaged over the entire footprint and is therefore not an accurate representation of the first object hit by the beam. This phenomenon can lead to misplacement of objects, as the reflection of especially the object's edges contains points of objects in the background.

The amount of laser beam divergence is related to the second factor, the instrument mechanism. Factors that influence scan accuracy are rotation mechanism aberrations, mirror centre offset, scanner mechanism precision, angular resolution and beam width divergence (Hejbudzka et al, 2010). Construction the scanner in such a way that its internal mirror is in the perfect position and flawless is impossible due to the machining and assembly process (Zhuang & Roth, 1995). This leads to an offset of the mirrors centre and axis misalignment, causing systematic errors in the measurements. According to Lichti & Jamtsho (2006), angular resolution is the extent to which a scanning device is able to resolve two point sources on adjacent lines of sight that are of the same intensity. This ability is therefore relevant in the identification of objects. Scanning devices come

with different angular resolutions, which thereby affect the accuracy of the measurements. Angular resolution is a function of the laser beam width, making beam divergence a critical parameter for accuracy.

Atmospheric conditions are the third main factor that can influence scan quality. The influence of ambient light is discussed in Voisin et al (2007). Measurements were taken under different lighting conditions, and deviations varied based on these conditions. Deviation also varied with surface colour, as different colours reflect different amounts of light. Systematic errors were even observed for specific colours. Hejbudzka et al (2010), mentions radiation, humidity and temperature as atmospheric conditions that can affect scan accuracy. High intensity precipitation and fog are also known to reduce scan quality by limiting the view range and producing noise in the scan. Results show a significantly reduced point count during fog, when radiation and temperature are at their daily minimum, and relative humidity at 95%. For normal conditions (temperature = 10-18°C, radiation = 10-450 W/m², humidity = 54-92 %) with temperature, radiation and relative humidity increasing simultaneously, point counts increase. Range tests performed by Hejbudzka et al (2010) further show increase of range variation with increasing relative humidity. Furthermore, during normal conditions a relation was found between temperature and range, though it was not further investigated if this trend was caused by scanner bias or actual temperature influence.

The final factor that is mentioned, is object surface properties. As was mentioned in the previous paragraph, surface colour is a factor that affects reflectivity and thereby scanner accuracy. Different colours reflect different amounts of light, with bright colours reflecting more than darker colours (Boehler et al, 2003). The material of the object can also limit reflectivity or increase scatter, as was found in Höfle & Pfeifer (2007). Kersten et al (2005) investigates the influence of object shape on system accuracy. Using a laser scanner, both spherical and square targets were measured, showing different deviations in range.

2.5. Data processing techniques

In this paragraph, several data processing techniques that are used in the research method are elaborated. The techniques concerned are progressive morphological filtering and noise detection.

2.5.1. Progressive morphological filtering

Many different filtering methods exist to separate terrain from non-terrain points, as this is crucial to construct a digital terrain model (DTM) from a point cloud (Zhang et al, 2003). Some examples are given by linear least squares interpolation (Pfeifer et al, 2001), slope-based filtering (Vosselman, 2000) and mathematical morphological filtering (Wang et al, 2014). Filtering has always proven a challenge, due to two basic types of errors that occur in the process. One could compare these errors to the Type I and Type II errors in statistics: classification of terrain points as non-terrain (omission), and classification of non-terrain points as terrain (commission) (Zhang et al, 2003).

Morphological filters make use of techniques that compare individual points to an area, or window, of points around them (Zhang et al, 2003). The success of many of these filters depends on the selection of the optimal window size. When choosing a small window, small objects are removed, but large objects are classified as terrain. The amount of commission errors is high. Vice versa, when selecting a large window, omission errors are common. In dune analysis, this will lead to peaks of dune mounds to be erroneously cut off. To achieve optimal filtering, that is with minimal

(c)omission, an ideal window size must be selected. This, however, differs per area, as the same window that was optimal on the beach could lead to serious errors in the dunes. Due to the large volume of data that usually needs to be analysed, manual selection of the window is not preferable.

Progressive morphological filtering improves on this issue by gradually increasing the window size for each individual scan, allowing for a point level filtering of terrain and non-terrain points. The filter starts out with a small window, successfully removing small objects. After applying this first window and removing the small non-terrain objects, the window size is increased. This, in turn, will remove larger objects than the previous iteration. This process of increasing window size continues until all non-terrain points have been filtered. By utilising this method, objects of various sizes are removed from the data, and a smooth surface remains. A drawback of this method is that the filtering process creates an error in the z-direction. The filtered surface lies lower than the original surface, removing many terrain points in the process (omission). To counter this effect, an elevation difference threshold is introduced. Since the elevation of the terrain varies gradually, a distinction can be made between terrain and objects using this knowledge. The elevation difference of for

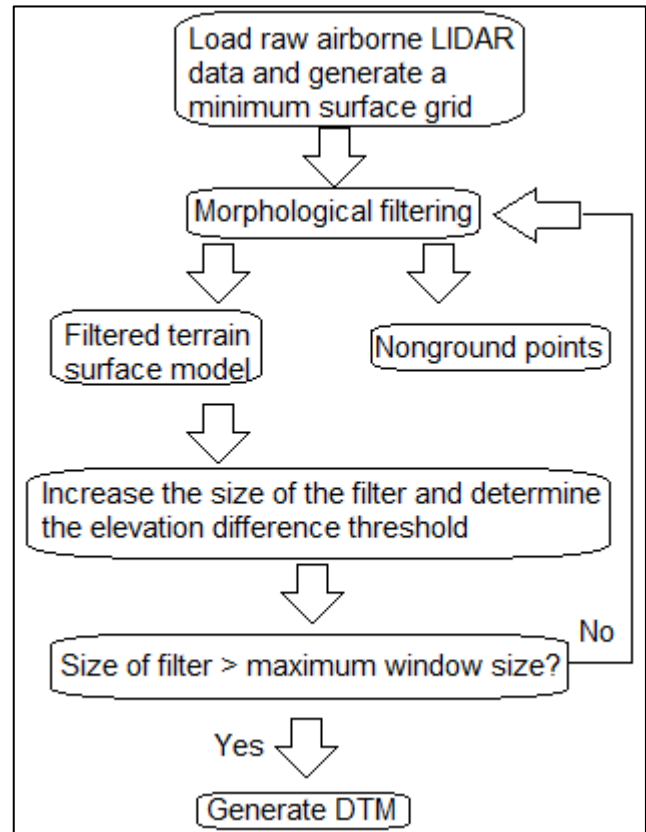


Figure 2-7: Progressive morphological filtering loop, adapted from Zhang et al, 2003.

example a building is much more abrupt and pronounced. When a point's elevation difference is smaller than the threshold, it will be classified as terrain and vice versa. If a threshold is selected so that the maximum height difference between original and filtered surface is smaller than this value, the laser measurements for the terrain will be retained. The threshold is determined per window size iteration, by taking the minimum height of the objects in this iteration. This way, the threshold accurately increases with increasing window size. The full loop is presented in Figure 2-7.

The proposed method does not fully eliminate (c)omission errors, but does reduce them significantly, compared to regular morphological filters (Zhang et al, 2003). Steep mounds were still erroneously omitted due to their rapid elevation change. When some trees were removed, strange patterns emerged for the terrain below them. This was possibly caused by lower bush under the trees. However, tests showed that the method did successfully deal with both vegetated and urban areas in the same scan, because of the increasing window size. Furthermore, the results show that only 3% of the points in a sample of 648 points were erroneously committed.

2.5.2. Noise detection.

Noise is a commonly occurring feature in point cloud data. Noise has a negative effect on the visualization of point clouds, and can interfere with analysis (Esri, 2018). Removal is often necessary to exclude such points from the visualization, to allow for the intended analysis of the

desired data. Noise can be caused by a variety of factors, including large numbers of small animals, fog or clouds, water bodies and highly reflective objects. Noise data is often of different quality than regular data, which is made use of in the elimination process. A common property to use is point density. The 'good' data usually has a much higher point density than noise in the data. Software can check the point density of entire point clouds by counting the number of points within a spatial window around a point of consideration. If the number of points within this spatial window is too small, the point is marked as noise and rejected from the cloud. The number of points and size of the spatial window can often be defined by the user and should be chosen in a fashion minimizes 'good' data losses. Considerations about computation times should also be made. Smaller spatial windows lead to higher computation times.

2.6. Data analysis techniques

Several techniques that are used in this thesis to analyse data are presented here.

2.6.1. Pearson's correlation

Pearson's correlation coefficient is commonly used for the identification of linearity between two variables (Sedgwick, 2012). A straight line is plotted through a scatter plot of the two variables that represents the best linear representation of the data that exists. How close the data points lie to this line is expressed by correlation. The Pearson's correlation coefficient r corresponding to the variables x and y is given by:

$$r = \sum_{i=1}^N \frac{(x_i - \bar{x})(y_i - \bar{y})}{\sqrt{\sum_{i=1}^N (x_i - \bar{x})^2 \sum_{i=1}^N (y_i - \bar{y})^2}} \quad \text{Equation 1}$$

The coefficient r can vary between -1 and 1. The closer the value is to 0, the less correlation there is between variables x and y . A value close to 1 means there is a positive correlation between both variables. This would imply an increase of variable x will also lead to an increase of variable y . A value close to -1 represents a negative correlation between the variables. This implies a larger value of x leads to a smaller value of y . A confidence interval of 95% around r is given to test if a correlation is significant. P-values of less than 0.05 correspond to statistically significant results, whereas values larger than 0.05 represent insignificant results. P-values are the statistical chance of occurrence of a certain result. When p-values are large, found correlations cannot be explained by the trend in the data, but rather could be fully explained by chance.

2.6.2. Linear least squares trend analysis

Linear least squares trend analysis is used to plot a straight line through a dataset of scattered points. This line identifies the trend in the data. The linear function is chosen based on the smallest possible sum of the squared distances of all points to this line. The smaller this sum is, the better the line fits the data. The residual sum of squares S between variables x and y is given by:

$$S = \sum_{i=1}^n (y_i - x_i^T b)^2 \quad \text{Equation 2}$$

The value of b is responsible for minimizing the sum. A means of measuring the distance of the data to the fitted line is through the R^2 parameter. R^2 , or the coefficient of determination, ranges from 0 to 1 and represents the amount of data that is represented by the fitted line. Values close to 0 therefore indicate a bad fit, which does not represent the data any better than a horizontal line through the mean of the variable on the y-axis. Low values do not necessarily mean that the fit is bad, just that the behaviour of the data is hard to predict. Conclusions can still be drawn from linear fits with low R^2 values. Values close to 1 represent very small distances of the data points to the fitted line and a near perfect representation of the fit.

2.6.3. Fourier analysis

Fourier analysis is used to decompose a signal into a number of trigonometric functions, the sum of which represents the original function. In Fourier analysis, it is common to generate a spectrum in which the sum of trigonometric functions is plotted. The peak of the spectrum is determined by the trigonometric function with the highest degree of similarity to the original function. This function represents the original function the best. Connected to the spectrum peak is the peak frequency, which is an indicator of the oscillatory motion of the trigonometric function. This frequency is given in Hz, or the number of cycles per unit sample time of the data that is fed into the analysis. This peak frequency gives an indication of the cycle time of the periodic components within the original function.

3. Approach

In this chapter, the chosen research approach is elaborated. The subjects that are present in this chapter are largely based on the research questions.

3.1. Data gathering and study area

3.1.1. Data gathering

The main piece of data used in this research, the laser scans, have been obtained in the period 19/10/2016 - 26/05/2017. The output data of the scanning device was made available by TU Delft for the purpose of this research. This data comes in the form of a horizontal angle, a vertical angle and the range to the point that was measured, which can be converted to 3D XYZ point clouds. The aim of the CoastScan project was to have hourly measurements of the beach, for several months (Vos et al, 2017). Especially during several months in 2016 though, the uptime of the laser was hindered due to a bug. Starting 2017, the laser was once again fully up and running, providing hourly measurements. For the purpose of this research, a continuous data series has been selected starting 01/01/2017 and lasting until 25/05/2017. Several storms have been identified in this time window, from wave and wind data. During this period, a daily low tide scan is selected, so that the largest possible beach surface area can be analysed, resulting in a timeseries of 132 days. In some cases however, obtained scans were of insufficient quality and could not be used. When possible, these scans have been replaced by other scans during low tide on that day. As example, Figure 3-1 displays a bird's eye view of the result of the January 24 scan and a typical low tide scan, after converting the laser output data points to XYZ-coordinates. As can be seen, hardly any points were measured during the scan of January 24. As of yet, no definite explanation for this result is available. It is known that bad weather conditions such as intense rain fall and fog can obstruct the view of the scanner, however the typical noise in the data that accompanies these events is absent.

Wind velocity and direction data was obtained from the Royal Netherlands Meteorological Institute (KNMI). These wind characteristics were obtained just off the coast of Kijkduin (52.057-52.081 latitude, 4.175-4.213 longitude), at an elevation of 10 m and with a frequency of 10 minutes. The timeseries was then reduced to the beforementioned period of interest and plotted (see Figure 3-2 and Figure 3-3). This data was used to identify storms. It is later also used to help explain variability in beach accretion rates. The KNMI wind data is freely and openly available through the KNMI database. Other data that was also obtained from the KNMI in this fashion includes precipitation, temperature, radiation and relative humidity. This data is also used to clarify trends and observations in the laser scan data.

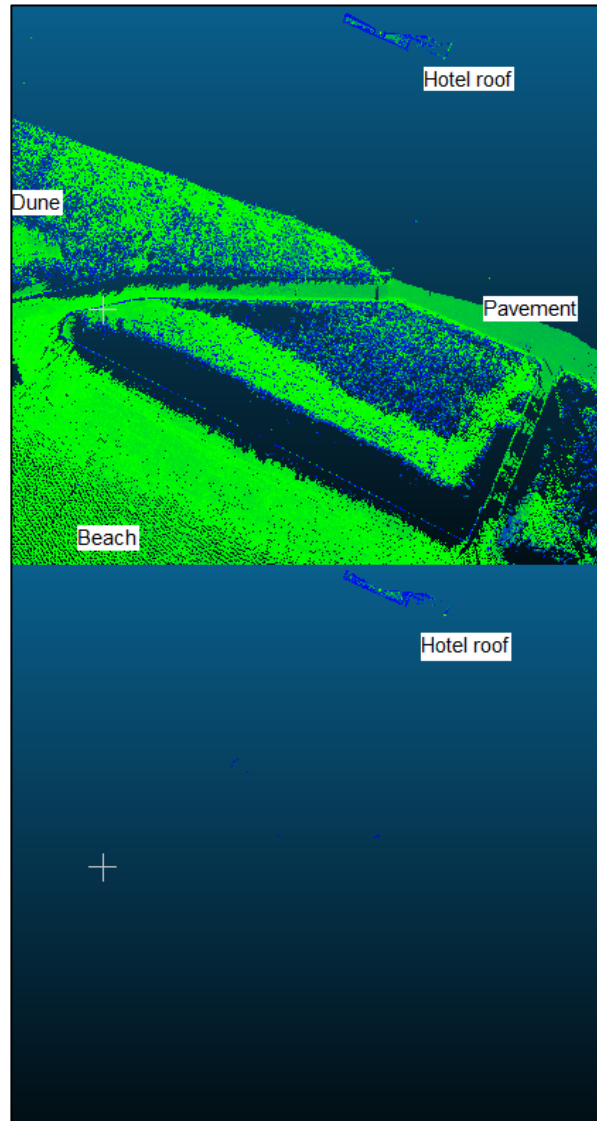


Figure 3-1: Top view of a typical low tide scan (top) vs. the January 24 low quality scan (bottom). Hardly any points were measured in the January 24 scan.

Tidal elevation data has been obtained from a station in Scheveningen, the Netherlands. This data was recorded and provided by Rijkswaterstaat. The data is plotted in Figure 3-4. To obtain this data for the period of interest, a data request was submitted to Rijkswaterstaat. Through use of this data, the daily low tides could be selected as to select laser scans of that particular time. It is also used to help clarify observed beach accretion rate variability, if applicable.

Wave height (Figure 3-5), direction (Figure 3-6) and period (Figure 3-7) data was obtained through TU Delft. Data from the offshore Euro platform in the North Sea was translated to nearshore conditions (depth of 11 m.) near the Sand Motor using a transformation matrix. The peaks in wave height correspond to the previously discussed storm. Similarly to the wind and tide data, the wave data will be attempted to be linked to beach accretion. During calm conditions, wave heights average about 0.5 m. During storms, a significant wave height of 4 m was exceeded.

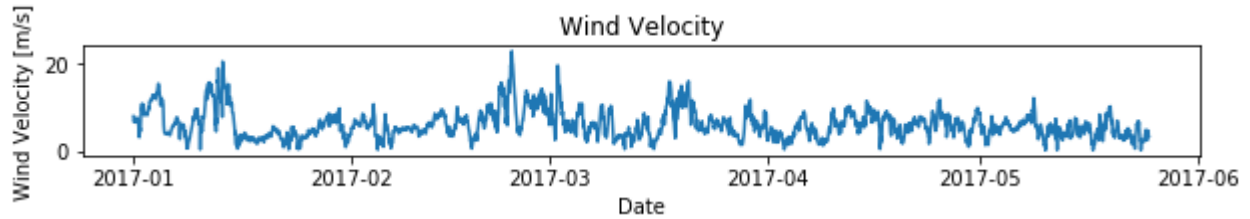


Figure 3-2: Wind velocity at Kijkduin, from KNMI.

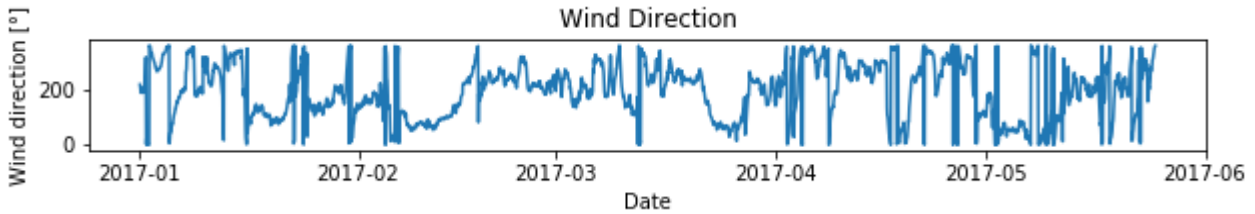


Figure 3-3: Wind direction at Kijkduin, from KNMI.

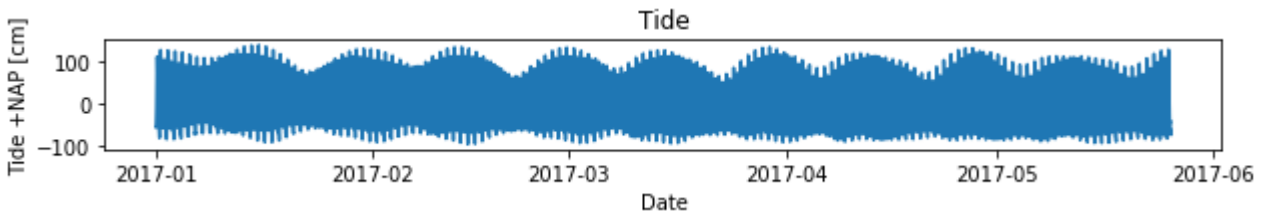


Figure 3-4: Tidal elevation at Scheveningen, from Rijkswaterstaat.

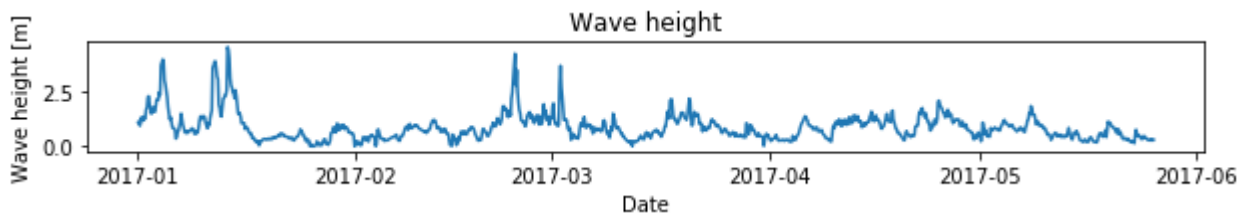


Figure 3-5: Wave height, translated from Euro Platform to a water depth of 11 m.

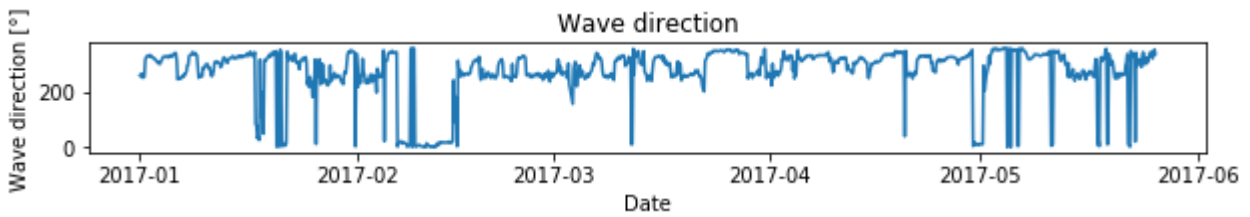


Figure 3-6: Wave direction, translated from Euro Platform to a water depth of 11 m.

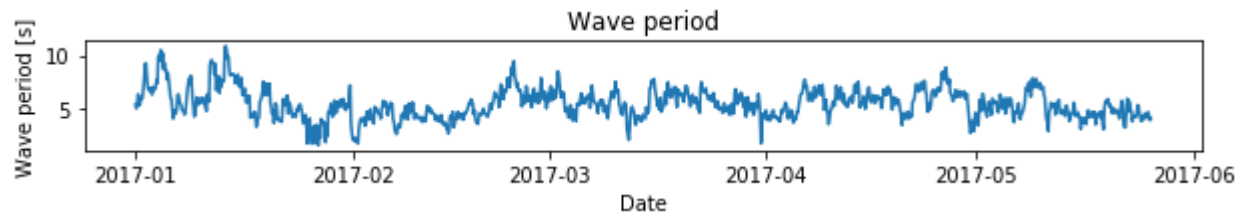


Figure 3-7: Wave period, translated from Euro Platform to a water depth of 11 m.

3.1.2. Study area

The area that is studied is located in the touristic region of Kijkduin, the Netherlands (see Figure 3-8). The beach is part of the South-Holland coast and lies along the North Sea. The beach is sandy and is located just north of the Sand Motor near The Hague. In the past, sand was nourished near this beach in order to combat naturally occurring erosion, as is still the case for other beaches along the Dutch coast (Rijkswaterstaat, 2018a). After the construction of the Sand Motor in 2011, it has been providing the Kijkduin beach with sand, widening it in the process. This due to the net northward longshore sediment transport along the Dutch coast. The area of the beach that is measured in the CoastScan project spans a total of about 2 km in longshore direction and covers sea, beach and foredune. Compared to other beaches along the Dutch coast, the Kijkduin beach is now quite wide. The dune height along the entire section easily exceeds +10 m above mean sea level and form a natural protection against the sea. In the period between March and October, beach pavilions and other buildings fill the beach to service beach visitors (The Hague Marketing Bureau, 2018). Several permanent buildings are present on top of and just behind the dunes. The laser scanner was mounted on top of a measuring frame on one of the hotels just behind the dunes, so that it had a clear view of the beach (Vos et al, 2017). The Riegl-VZ2000 laser scanner was shielded by a protective housing, and a total of 5 reflectors had been placed in its vicinity, on the roof and on objects on the beach, to aid the scanner in the process of positioning.

The average tidal range at the study site is about 1.8 m (Rijkswaterstaat, 2018b). This range creates an intertidal zone that stretches about 70-80 m. in cross-shore direction. Along the Dutch coast, both swell waves and locally generated wind waves are observed. The average wave height during calm conditions at the site is about 0.5 m, usually coming in from a north-north-westerly direction. The British land mass protects the Dutch coast from exposure to swell waves from the west. Particularly during winter, the beach is hit by storms in which wave heights can exceed 4 m. Several groynes are present on the beach, that are fully submerged during high tide. During low tide, the groynes are more exposed, though partially covered in sand. Several kilometres north of the study site, a dam has been placed to protect the inlet of a small harbour.



Figure 3-8: Study area, from google maps.

3.2. Accuracy and consistency check

In this paragraph, the accuracy of the measurements will be investigated, and checked versus the accuracy indicated by the laser producer. The data obtained by the laser will also be checked for consistency.

3.2.1. Laser specifications

In order to obtain measurements that represent small scale change, a measuring device of sufficient accuracy needs to be utilised. The producer of the Riegl-VZ2000 laser scanner claims the accuracy of the measurements to be 5 mm. at a distance of 100 m., and the precision to be 3 mm. (Riegl Laser Measurement systems GmbH, 2017). Accuracy is defined as the degree in which a measurement corresponds to the true value, whereas precision is defined as the degree to which additional measurements display the same result as the initial measurement. According to the specifications, the angular step width should be smaller than 0.6° in vertical direction (between consecutive laser beams) and smaller than 0.62° in horizontal direction (between consecutive scan lines). The divergence of the laser beam should be equal to 0.27 mrad, which translates to 27 mm. at a distance of 100 m. These specifications are, according to the producer, measured under average conditions. This means the measured target is bigger than the laser beam divergence at that distance and positioned perpendicular to the laser so that there are no inaccuracies caused by low angles of incidence. Atmospheric visibility under these conditions was 23 km. The producer further indicates that the maximum range of the laser is reduced on days with bright sunlight, relative to overcast sky.

3.2.2. Accuracy check

To obtain an indication of the accuracy of the laser scans, several tests are performed. By running the tests at various time levels, the data can be checked for temporal patterns that may arise due to scanner malfunction. First, the rotational accuracy of the laser scanner is examined. As was discussed earlier, the scanner measures in a horizontal angle ϕ , a vertical angle θ and a time lag between the outgoing and incoming beam. These three variables can then be converted to XYZ-coordinates. Before this conversion, the angles themselves can be analysed. To do so, a reflector in the dunes has been selected. This reflector has a diameter of 5 cm. and is used for the location of the scanning device. This reflector is mounted on a light post roughly 86 meters from the laser scanner, which should be relatively stable. In other words, it is expected that the reflector's position does not change over time. The reflector is made of a material with much higher reflectivity than its surroundings. The point of

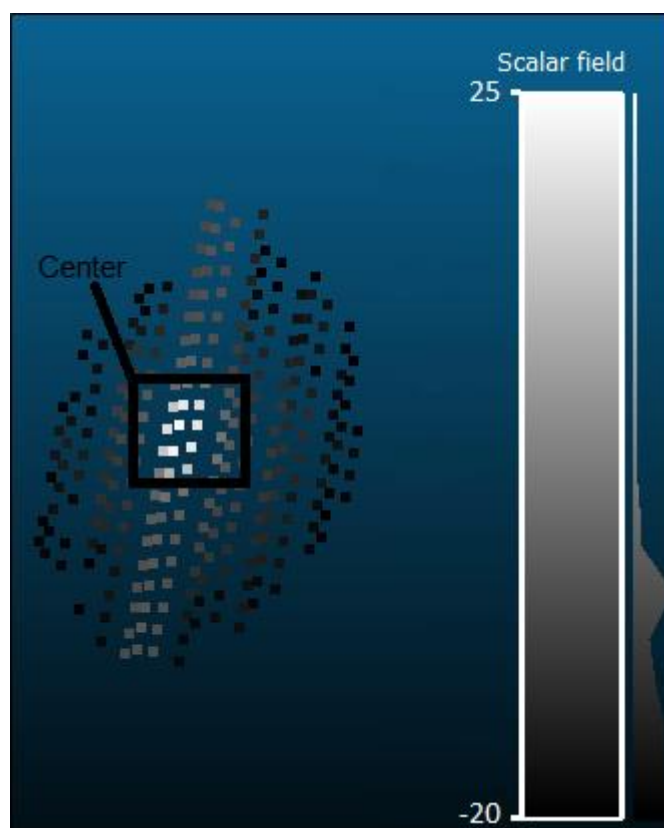


Figure 3-9: High resolution representation of reflector. Scalar field represents reflectivity.

maximum reflectivity of the reflectors is expected to be in its centre, as is observed in high resolution scans of the reflectors (see Figure 3-9). The scans that were used for this analysis were of lower resolution, making the image of the reflector less clear. These scans are available with an hourly frequency, whereas the high-resolution scans were only performed once a day. The point of maximum reflectivity on this particular reflector is determined for timeseries at the following intervals:

- Hourly for two consecutive days.
- Daily for the duration of two weeks.
- Daily for the duration of a month.

Several variables were analysed to determine the position of the centre point of the reflector. Both angles (φ and θ) are analysed to check the rotational spread. Additionally, the range or distance from the scanner to the centre point is analysed. In some cases, the obtained reflection was of poor quality, in the sense that the point of highest reflectivity at a certain time had a low reflectivity compared to centre points at different times. This could be caused by the footprint of the laser not completely lying within the reflector but partially off the side. The scanner averages the value obtained from the footprint, which then includes points of terrain behind the reflector, leading to a lower reflectivity value for the centre point. To isolate this effect, the prescribed test has also been performed using only times that had a centre point with a reflectivity higher than a threshold level. To verify the resulting rotational spread, a different reflector in the dunes has been selected to perform the same tests on.

A similar test was set up to determine the accuracy of the scanner in vertical direction. A segment of pavement (20 m²) was analysed by taking the average z-value of the section for the same abovementioned timeseries. The pavement is part of a path in the dunes at a distance of 100 m from the scanner, and should, besides the occasional minor sand deposit, not change position over time. The pavement is covered by rectangular concrete bricks, with a rough surface. In rare cases, temporary objects were present on the segments which were removed so that only the elevation of the terrain would be evaluated.

Observed discrepancies in both tests were noted and cross-tested, and the mean, range and standard deviation values for both tests were determined. This standard deviation will later be used in the determination of beach volumes. Correcting the found standard deviation to range allows for expression of the uncertainty in the found volumes.

3.2.3. Consistency check

The data obtained by the laser scanner needs to be checked for consistency, to make sure no gaps in the data are present at crucial locations (both in spatial and temporal dimensions). For the data that was used in this research, this was done visually. The data is also checked for other irregularities.

3.3. Data processing

Before the data can be analysed, several processing steps need to be performed. The input data for this research consists of 3D point clouds where all points have designated x, y and z-coordinates. Additional information such as reflectivity and range can be included in the point clouds. Before cross-sections can be extracted from these point clouds, they need to be cleaned to exclude noise and objects on the beach. An example of a raw point cloud is displayed in Figure 3-10.

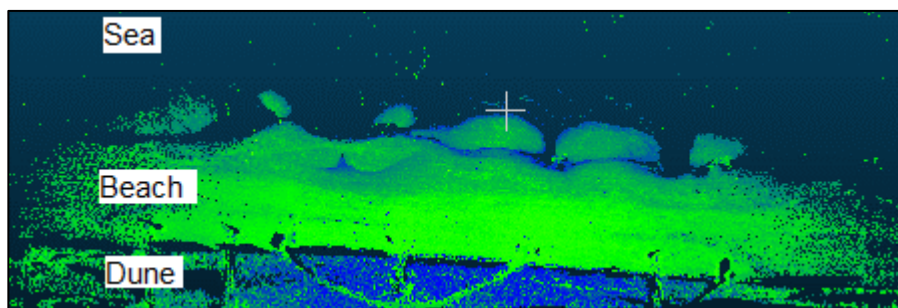


Figure 3-10: Top view of raw beach scan. Color scale represents reflectivity.

Even when only regarding the top view (therefore unable to observe elevation differences in z-direction), noise can be seen in the sea and behind the dunes. In order to properly execute future processing steps, this noise needs to be removed. In the same figure, several gaps can be observed on the beach. These gaps are essentially shadows of objects that stand between the gap and the laser scanner. Objects that have been observed in the raw data include relatively large objects such as buildings and smaller ones such as humans and posts. To extract cross-sections that represent the terrain, these objects need to be removed. Several methods are evaluated and optimised in order to achieve object and noise removal. Judging which method is most effective is done visually, by observing which method accomplishes the job the best without generating too many negative side effects, and by comparing the result to a result that was obtained by hand.

Before cross-sections can be extracted from the point cloud, the gaps between the points need to be interpolated to form a 3D layer that covers the entire research area. The processing of the data was mainly done using Python 3. Several interpolation methods that are offered by Python are evaluated by looking at how well they represent the data, both visually and by comparing the area under the cross-section, and by considering the computation time. Another factor that is evaluated is the number of points to interpolate over a cross-section. Increasing the amount of points leads to more accurate results, but higher computation times. When handling data sets such as this one, computation time is a factor that needs to be considered as it can get notably large. A way to further reduce the computation time is by reducing the amount of points in the data. This can be done in several ways. One way is through cropping the data to only consider a section of interest. Another way is through subsampling of the point cloud. It is known that subsampling reduces the accuracy of the data. Therefore, the remaining point cloud after subsampling still needs to be representative of the original data. This is evaluated by considering different levels of subsampling and comparing the area under the cross-section, as well as the gain in computation time.

3.4. Cross-section extraction

After completing the processing of the data, cross-sections can now be extracted from the point clouds. To do so, a set of points is chosen, between which all elevation data on the line connecting the two points is collected from the processed point clouds (see Figure 3-11). At these transects, one cross-section per day is extracted during low tide, for 132 days starting 01-01-2017. These locations were selected for several reasons, the first being that during the research period, there were no large structures such as buildings located here. These buildings would hinder the analysis of volume behaviour as they both trap sediment that is travelling dune ward and leave a gap in the data after removal from the cloud that is linearly interpolated and therefore contains no information on the actual beach terrain. The second reason for selecting these location is the presence of sand bars, so that their behaviour can be included in this study. The cross-sections are cut off at an elevation of NAP+5 m, just before the data gap between beach and dune. No limit is imposed on the sea ward end of the cross-sections. A total of 4 transect locations are chosen, within a longshore range of 300 m.

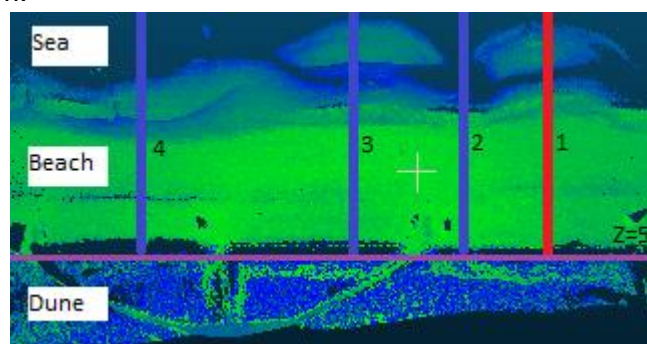


Figure 3-11: Top view of point cloud, red line indicates initial transect. Blue lines indicate remaining transects. Purple line indicates NAP+5 m. line.

3.5. Analysis

In order to arrive at answers to the research questions, several analyses are performed. A detailed analysis is first performed on transect 1, after which a general analysis is performed on the combined data of all transects. For starters, a time stack image is constructed, so that the behaviour of the beach at location of the transect is visualized throughout the research period and can be studied. Such an image takes the cross-sectional distance and plots it versus the date of measurement. Elevation levels of the cross-sections are expressed in colour, visualizing the morphological change in time at this location. A mean in time and envelope of all cross-sections at this location are also computed, as well as a variability plot. Further description of morphological change is provided by plotting the location of various NAP +X positions (e.g. the cross-shore position of the mean sea-level, NAP+0 m), so that their movement in time can be tracked. By computing the area under the cross-sections and multiplying it by 1 m. longshore, the volume of a 1 m. wide strip on the beach bordering the extracted cross-sections is determined. This volume is both computed for the entire cross-section, as well as for spatial zones of interest within the cross-sections. These zones are intertidal zone, backshore and foredune. After computing and plotting the volumes in time, trends in volume and volume change are determined using linear trend analysis, as well as Pearson correlations between volume change and boundary conditions such as wind and wave data, and correlations between volume change in the different areas of interest. A Fourier analysis is also performed on the beach volume and boundary conditions, to identify the spectrum of the signal and peak frequency.

4. Results

In this chapter, the results of the prescribed approach are discussed.

4.1. Accuracy check

The use of the prescribed elimination method using a reflectivity threshold significantly reduced the amount of remaining points. This leads to more accurate results; however temporal patterns can no longer be studied. An example of the effect of elimination is presented in Figure 4-1. In this figure, the range between TLS and reflector has been plotted over two consecutive days, with an hourly frequency. After elimination of the weaker reflections (b), many patterns that were visible pre-elimination (a) are no longer visible. Only the marked pattern is still recognisable. Since these patterns provide insight in the stability of the TLS, only pre-elimination plots are displayed in the remainder of this paragraph.

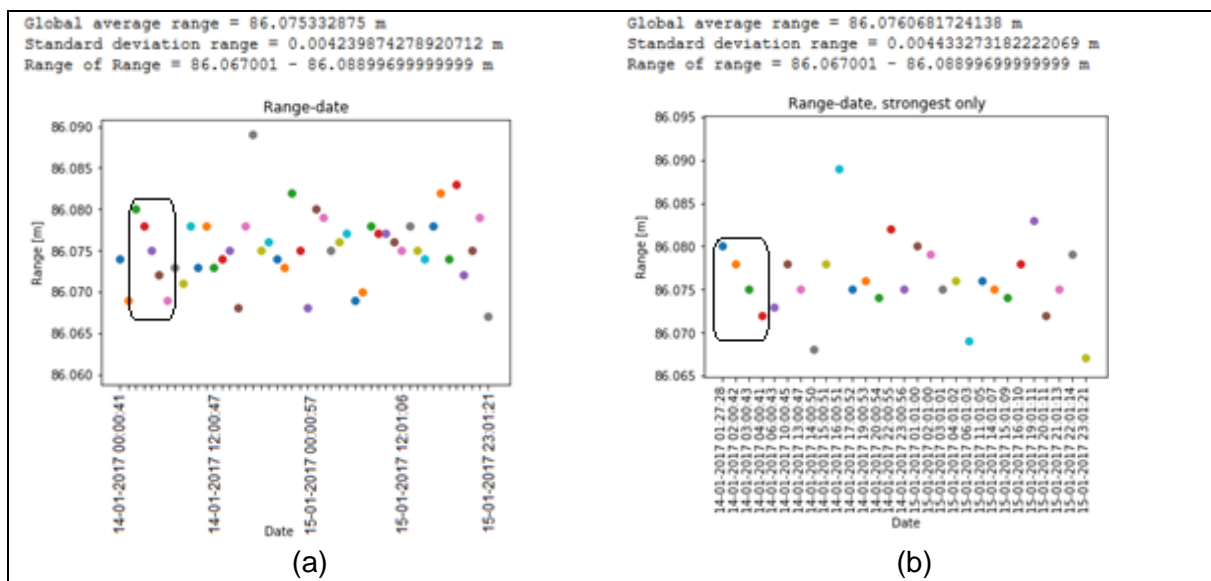


Figure 4-1: Comparison of accuracy test pre-elimination (a) and post elimination of weakly reflective points (b). Box gives example of temporal pattern.

Figure 4-2a-c display the results of the accuracy tests with a time step of one hour for two consecutive days (14 and 15 January 2017). In Figure 4-2a, the vertical angle θ corresponding to the point of maximum reflection has been plotted versus the date and time of the measurement. No structural temporal patterns can be observed in this plot besides a slight positive trend as time progresses. A feature that does stand out can be seen starting at 14-01-2017 02:00:00 and lasts until 14-01-2017 06:00:00 and has been circled in the plot. The centre of reflectivity follows a slight downward trend at this interval. This feature is not observed in the night of 15-01-2017. Analysing the obtained meteorological data did not show any particular cause for this effect. The pattern may be caused by an error in the scanning device, causing to drift in a certain direction for a few days before correction itself. In general, wave, wind and precipitation data were higher on 14-01-2017 than on 15-01-2017. To be able to say for certain there is a relation between the decrease in these meteorological variables and the slight positive trend in Figure 4-2a, further detailed investigation is required. Conditions were however decreasing throughout the day of 14-01-2017, whereas this pattern is only observed within a particular time frame. All observed values of θ in these two days lie within a range of 0.0584° , with a standard deviation of 0.0147° . Since the range to the reflector is

Mapping sub-annual beach growth using terrestrial laser scanning: Results

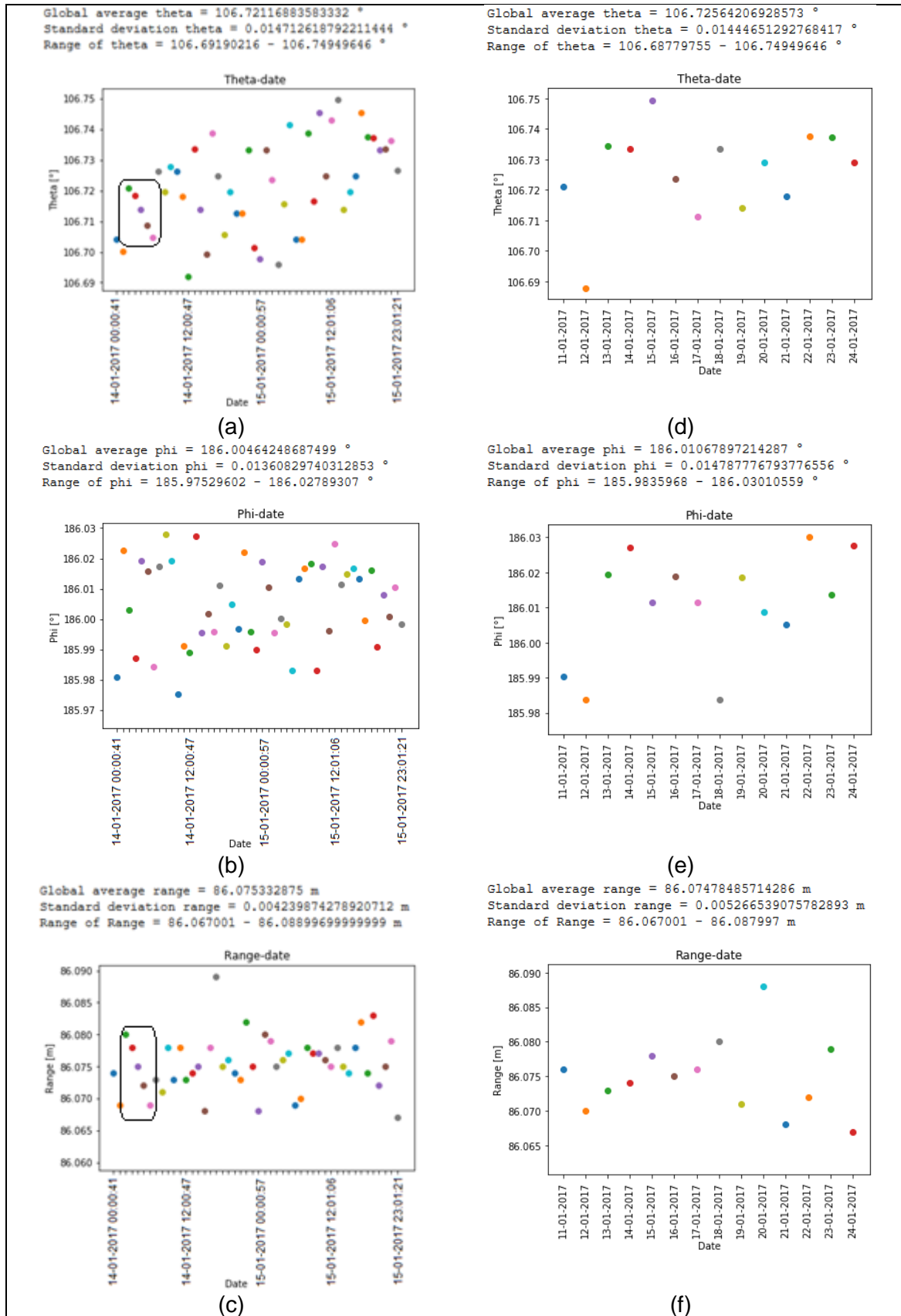


Figure 4-2: Results of rotational accuracy test on hourly time scale for two consecutive days (a-c) and daily time scale for two consecutive weeks (d-f). Several observed patterns have been marked per example.

known, the standard deviation can be translated from degrees to cm. using basic trigonometry ($0.0147^\circ = 2.27$ cm).

The horizontal angles φ that were found for the point of maximum reflection have been plotted in Figure 4-2b. The feature that was observed in the night of 14-01-2017 in Figure 4-2a is not present in this data. The range of the angle does seem to slightly decrease as time passes (and meteorological conditions become less energetic). All observed values of φ in these two days lie within a range of 0.0526° , with a standard deviation of 0.0136° (2.1 cm).

The distance between laser scanner and point of maximum reflection have been plotted in Figure 4-2c. The downward trend in the night of 14-01-2017 is also observed in this plot. Since the vertical angle θ is related to the computation of the distance to the target, this is expected. In this plot, several consecutive points are visible that follow the same upward or downward trend. In some cases when the trend is interrupted, the following points display the same trend, but have experienced a vertical translation. It is possible that in these cases the point of maximum reflection was captured by a laser beam above or below the one that captured this point at the previous time. The value of the received footprint containing the point is now averaged over a different surface and therefore the point is slightly displaced. The range of values for the range parameter was 2.2 cm, with a standard deviation of 0.42 cm.

The results of the rotational accuracy tests with a time step of 1 day for two consecutive weeks are displayed in Figure 4-2d-f. The days that have been plotted are 11 January 2017 - 24 January 2017. A storm occurred on 13/14 January. In Figure 4-2d, the vertical angle θ corresponding to the point of maximum reflection has been plotted versus the date of the measurement. No structural temporal patterns can be observed in this plot. All observed values of θ in these two weeks lie within a range of 0.0617° , with a standard deviation of 0.0144° (2.22 cm). The horizontal angles φ that were found for the point of maximum reflection have been plotted in Figure 4-2e. No temporal patterns can be observed in this plot. All observed values of φ in these two weeks lie within a range of 0.0617° , with a standard deviation of 0.0148° (2.28 cm). The distance between laser scanner and point of maximum reflection have been plotted in Figure 4-2f. Again, no temporal pattern is observed in this plot. The range of values for the distance is 2.1 cm, with a standard deviation of 0.53 cm.

The results of the rotational accuracy tests with a time step of 1 day for one month are displayed in Figure 4-3a-c. The days that have been plotted are 11 January 2017 - 05 February 2017. The storm occurred on 13/14 January. In Figure 4-3a, the vertical angle θ corresponding to the point of maximum reflection has been plotted versus the date of the measurement. No structural temporal patterns can be observed in this plot. All observed values of θ in this month lie within a range of 0.0628° , with a standard deviation of 0.0170° (2.62 cm). The horizontal angles φ that were found for the point of maximum reflection have been plotted in Figure 4-3b. No temporal patterns can be observed in this plot. All observed values of φ in this month lie within a range of 0.0484° , with a standard deviation of 0.0157° (2.42 cm). The distance between laser scanner and point of maximum reflection have been plotted in Figure 4-3c. Again, no temporal pattern is observed in this plot. Noteworthy though are the points for February 1, 2 and 3, which are all at the same range. The range of values for the distance is 2.19 cm, with a standard deviation of 0.49 cm.

Mapping sub-annual beach growth using terrestrial laser scanning: Results

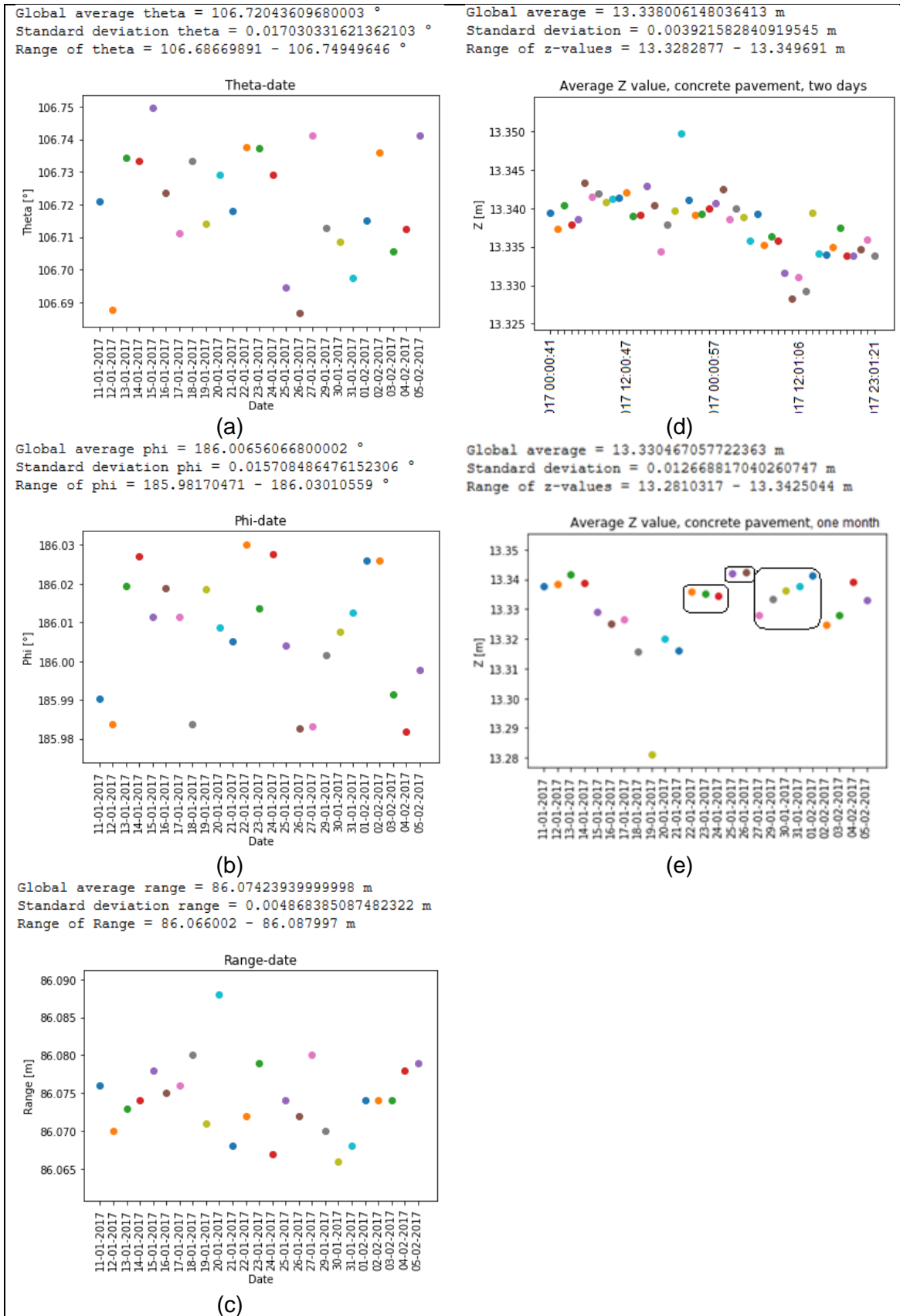


Figure 4-3: Results of rotational accuracy test on daily time scale for one month (a-c) and average z-values of 20 m² pavement cut out, with various time steps (d-e). Several observed patterns have been marked per example.

The results of the vertical accuracy check using the pavement cut-outs are displayed in Figure 4-3d-e. Due to lack of added value, the two-weekly data was left out of this analysis, as its results can also clearly be seen in the monthly analysis. On the hourly timescale Figure 4-3d), a slight negative trend is observed, with one significant outlier. All z-values in this plot lie within a range of 2.14 cm, with a standard deviation of 0.39 cm. In the plot containing the monthly data Figure 4-3e), a general wave-like motion can be observed, with one significant outlier at 19-01-2017. From January 13th until January 18th, a negative trend is observed. When looking into the data, it is observed that this trend does not exist at other locations. Results at other locations display vertical instability, indicating another error in the scanning device. After checking the data, it appears that indeed the data of 19-01-2017 lies lower than data of other days, at location of the concrete pavement until the waterline. However, this has not shown to be true at other locations on the beach on this date. On a location further away from the scanner (in longshore direction), the data of 19-01-2017 is consistently higher than data on other dates, indicating the possibility of an erroneous rotation of the scan on this date. It is known that meteorological factors such as radiation and relative humidity can interfere with scanner accuracy and could therefore be a contributor to the observed effect, however no extreme values were observed for these factors at this date. The slight negative trend that was observed in <FIG3>d can also be seen in this figure. The range of values on this time scale is 6.1 cm, with a standard deviation of 1.27 cm. Several consecutive points can be identified in this plot that appear to follow the same trend. Examples of this are 22-24 January, 25-26 January and 27 January - 01 February.

4.1.1. Summary and cross-check

The results of both tests have been summarised in Table 4-1 and Table 4-2. The results of both the rotational and vertical accuracy checks have been compared and checked for temporally coinciding patterns, however no connection between the observed patterns were found. These results were verified by considering a reflector at a different location (at comparable range). The order of magnitude remained the same for both reflectors.

Elimination of the points with weak reflection leads to a more accurate horizontal and vertical measurement but has shown to have little effect on the measured range to the reflector. Furthermore, temporal patterns could no longer be studied very well, as the number of points that were eliminated was relatively high. Because some plots contain very few remaining points after application of the threshold, the reliability of the results is questionable. This effect could be countered by using a longer timeseries, but this was not performed in this research due to time limitations. It can also be argued that the effect of bad reflections which was eliminated by the threshold, will not only occur for this particular reflector, but will occasionally occur at other locations in the data as well. Even when disregarding Table 4-2, the results of the rotational tests fall well within the specifications of the producer. The range of values for the horizontal and vertical angles are well below the specified angular step width, indicating the scanner is generally working correctly and measuring at its full capability. For all timeseries, the value ranges are of the same order of magnitude, despite the sometimes odd temporal patterns that were observed. These are likely the result of scanner instabilities. Even though the two days that were considered for hourly scans (14 and 15 January) were not during calm wind conditions, they still displayed similar value ranges compared to the other time scales. The results of the vertical accuracy however, are significantly worse than the accuracy indicated by the producer. This is however expected, as the measuring conditions on the beach are far worse than the ideal conditions the producer has used for his specifications. The observed standard deviations are still within acceptable limits for the eventual

computation of beach volumes. To do this conservatively, the least accurate vertical standard deviation from Table 4-1 is selected (1.51 cm). It is assumed this standard deviation scales directly proportional with distance and will be used as such. This is however an assumption, as the distance to the target will usually scale linearly with range (Vosselman et al, 2010), but does not have to be directly proportional. The relation between range and standard deviation should be further studied using a different measuring set up or research method. This has been done by Sander Vos, who personally disclosed having found an accuracy of 1 cm. per 100 m. distance in longshore direction for this dataset.

Timeseries	No reflectivity threshold								Point count #
	Theta		Phi		Range		Z-value		
	Range [°]	St. dev. [°]	Range [°]	St. dev. [°]	Range [cm]	St. dev. [cm]	Range [cm]	St. dev. [cm]	
Hourly data, 2 days	0.058	0.015	0.053	0.014	2.2	0.42	2.14	0.39	48
Daily data, 2 weeks	0.061	0.014	0.062	0.015	2.1	0.53	6.1	1.51	14
Daily data, 1 month	0.062	0.017	0.048	0.016	2.19	0.49	6.15	1.27	24

Table 4-1: Results both tests, without reflectivity threshold.

Timeseries	Including reflectivity threshold							Point count #
	Theta		Phi		Range			
	Range [°]	St. dev. [°]	Range [°]	St. dev. [°]	Range [cm]	St. dev. [cm]		
Hourly data, 2 days	0.043	1.16	0.032	0.95	2.2	0.44	29	
Daily data, 2 weeks	0.026	0.84	0.035	1.19	2	0.56	6	
Daily data, 1 month	0.043	1.36	0.042	1.1	2.19	0.59	12	

Table 4-2: Results both tests, with reflectivity threshold.

4.2. Consistency check

After visual evaluation of the data, it was observed that several discrepancies are present. One of these was already observed and described earlier. Several scans are of such poor quality that they could not be used, leading to a discrepancy in the time step in the research. In the extraction of cross-section series, these temporal gaps (usually no more than 1 day) will be visible. Only in one instance did a larger temporal gap of several days exist, due to a system bug. Spatial inconsistencies in the form of data gaps have also been spotted in the data. These data gaps are usually caused by the presence of buildings or other objects, which leave a gap in the data after they are removed, as well as casting a shadow in the data behind the object. The transect locations have been selected to largely avoid these spatial gaps.

Another issue that was discovered after extraction of several test series of cross-sections from the 3D point clouds, is a rotational instability of the laser itself. Consecutive scans were all slightly rotated compared to preceding scans, around a cross-shore axis on the beach, in front of the TLS. These rotations lead to vertical jumps between consecutive cross-sections, as can be seen in Figure 4-4. To counter these jumps, a correction was applied. This correction stabilizes the cross-sections by forcing the z-level of the backshore, where the envelope of the cross-sections was found to be the smallest, to a specified elevation value for all cross-sections. This does reduce the erroneous behaviour that was observed but does not allow for small fluxes such as aeolian transport to be accurately studied, as these fluxes are of smaller magnitude than the applied correction of the cross-sections. This strongly limits the study of accretion of backshore and foredune. The results of this method have been displayed in Figure 4-5. As can be seen, the vertical jumps between consecutive cross-sections are no longer present, and bar migration behaviour and accompanying volume change can be studied more accurately.

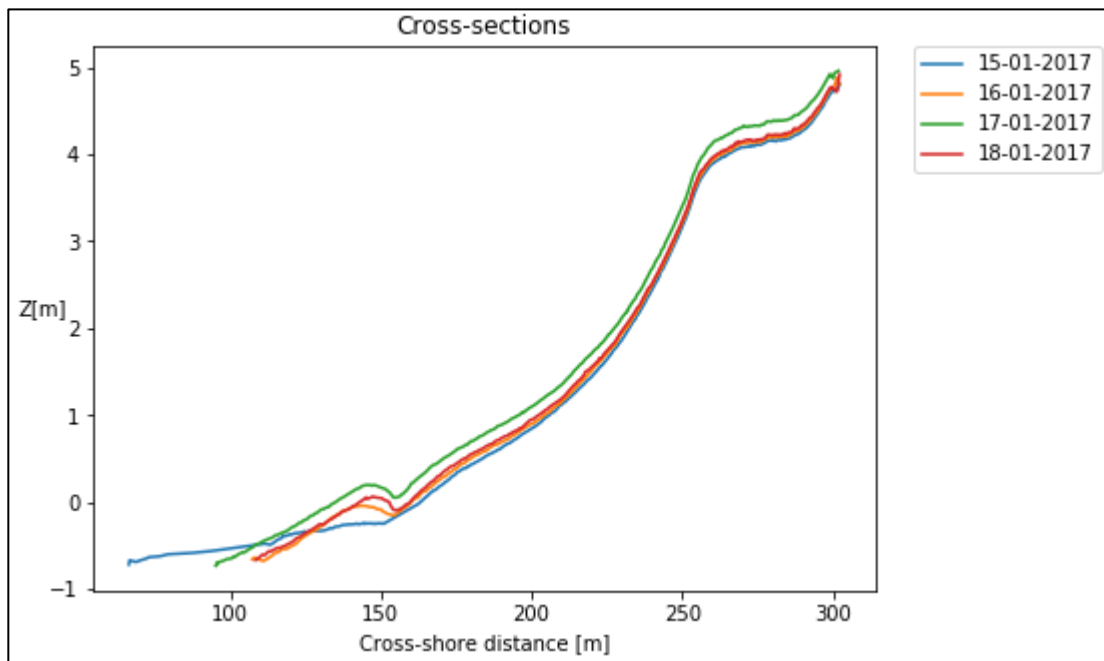


Figure 4-4: Four consecutive cross-sections extracted from the point cloud at the same location. Vertical translations between consecutive days are clearly visible.

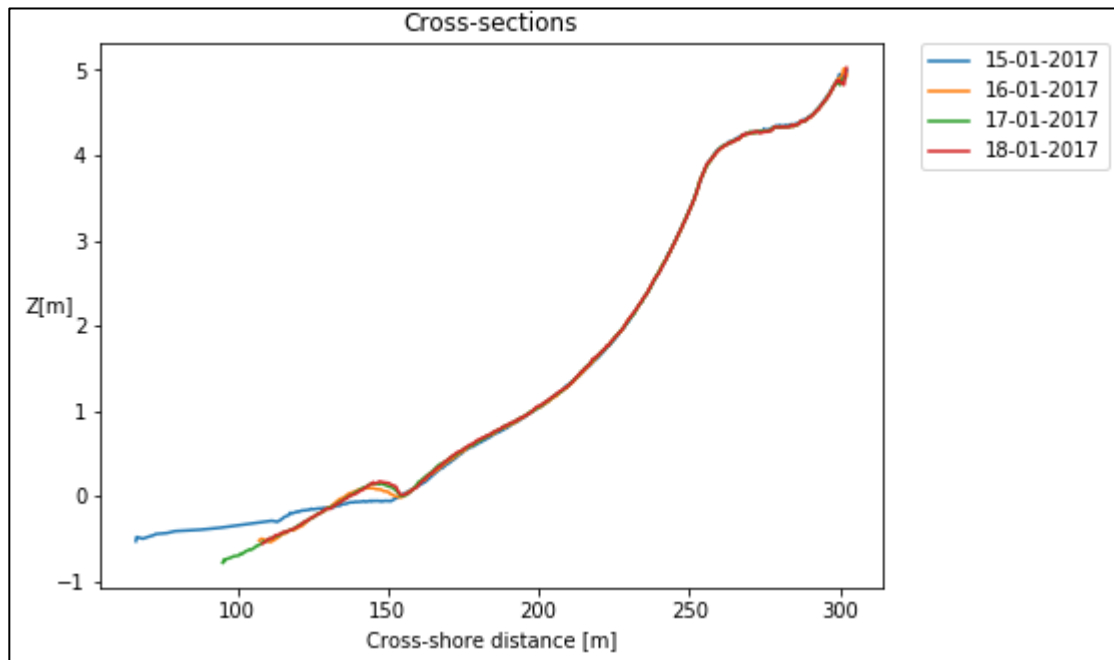


Figure 4-5: Four consecutive cross-sections extracted from the point cloud at the same location. Vertical jumps between consecutive cross-sections have been cancelled by forcing the backshore z-value to be constant for all cross-sections.

It was observed that not all cross-sections are of equal length. In some periods, such as the one displayed in Figure 4-5, the lowest measured point of the cross-section is positioned at a cross-shore distance of around 100-110 m. However, in other periods, the lowest measured point lies upward of 150 m. cross-shore distance. Several possible causes for this phenomenon exist. These include the influence of variations in tidal range, influence of meteorological conditions on scanner performance or scanner malfunctioning. Attempts have been made to find the cause of the varying cross-sectional length, by linear regression between cross-sectional length and tidal range, precipitation, radiation and relative humidity. However, no significant relation between these variables and cross-sectional length were discovered. Since combinations of these variables are known to further influence scanner performance, and these unfavourable combinations often occur at certain times of the day, the cross-sectional length was also checked versus the time of day they were captured at. This also did not lead to any conclusive results. When checking the 3D scans corresponding to these shorter cross-sections, it is observed that the scan is not only shorter at the location of the cross-section, but along the entire beach when compared to the scan of the previous day. Entire sand banks that were captured on a certain day are not captured on the next day. This raises the suspicion that there is indeed a factor interfering with scanner performance.

In the lower reaches of the cross-sections, data quality has been found to depreciate. Figure 4-6 presents the envelope and mean in time of all cross-sections at a location on the beach. As can be seen, starting at a cross-sectional distance of 150 m. and down, the envelope and mean display jagged edges and straight lines, caused by interpolation of low quality data. This effect is no longer observed from a cross-sectional distance of 150 m. and up. Therefore, for all transect locations, the lower reach of the cross-sections is regarded as unreliable and not included in any analyses.

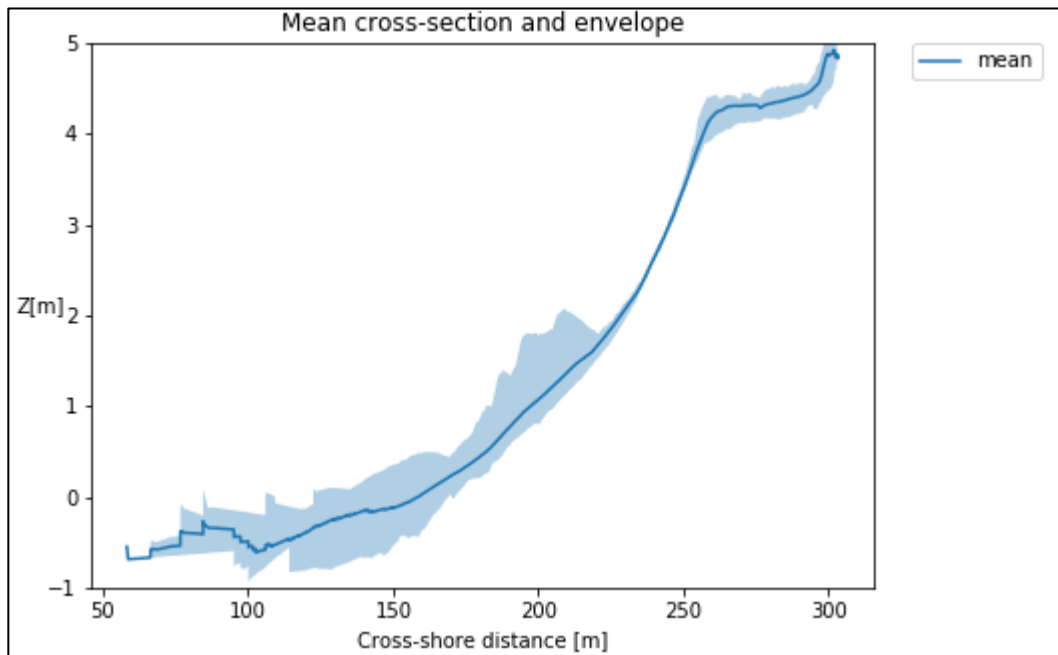


Figure 4-6: Mean in time and envelope of all cross-sections at one transect.

4.3. Data processing

For the removal of noise in the data, two separate techniques were evaluated: a built-in outlier removal tool in CloudCompare and a noise removal tool called Lasnoise that is part of the LAsTools package developed by Rapidlasso. The CloudCompare tool computes the mean distance from a point to its nearest neighbours. It then rejects points that have a larger distance than the average distance plus x times the standard deviation, in which x is a variable that is defined by the user. The Lasnoise tool counts the number of neighbouring points in a cell surrounding a point. Points that have too few points in the cell surrounding them are rejected. Cell size and point count threshold can be set by the user. Both techniques allow for finetuning in the noise removal process, and both techniques show promising results when it comes to the elimination of noise. However, both techniques also erroneously eliminate a portion of low quality beach data by the edges of the point cloud. When both methods are calibrated to remove all noise points in the data, the CloudCompare tool removes more of these beach points than the Lasnoise method (see Figure 4-7). These results have led to selection of the Lasnoise tool for the removal of noise in the data. After comparing the number of remaining points in the Lasnoise cloud to a cloud in which noise was removed by hand, at the location where cross-sections were extracted, Lasnoise was found to have missed only $2.61 \cdot 10^{-4}\%$ of the points that were removed by hand.

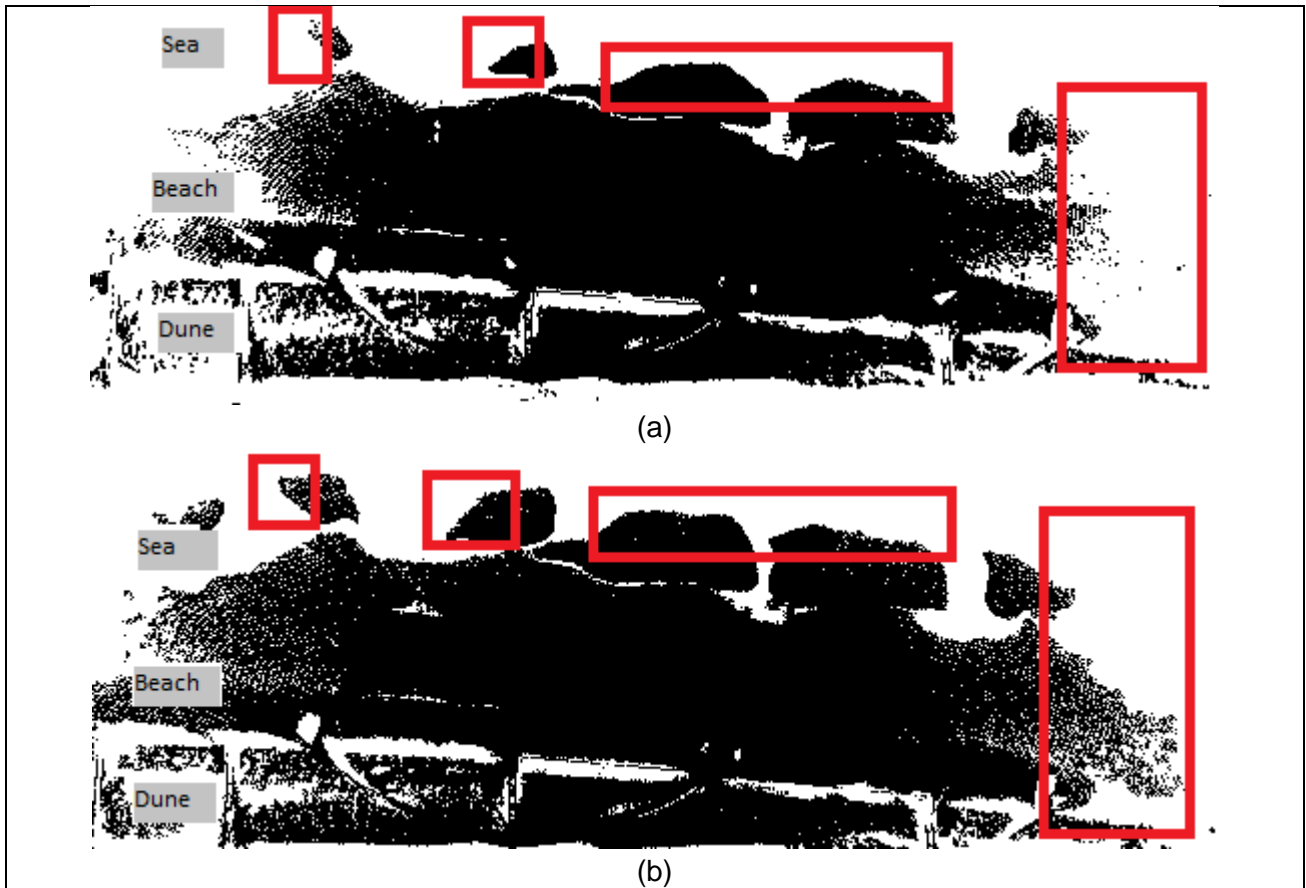


Figure 4-7: Top view of results of noise removal using CloudCompare (a) and Lasnoise (b). Differences in point removal are highlighted

Different methods have been tested for the removal of objects on the beach (see Figure 4-8). The first method makes use of a tool developed by TU Wien, called OPALS. The OPALS package offers a tool called Robfilter, which makes use of robust surface interpolation to separate terrain from non-terrain points. The second method makes use of CloudCompare. The software estimates the roughness of all points based on the distance between the points and the best fitted plane. Points with high roughness can then be removed from the point cloud, leaving only terrain points. The final method that was evaluated is LASground, which makes use of progressive morphological filtering. A sample has been taken from the point cloud that contains terrain as well as objects (see Figure 4-8a). In the top left corner three humans can be seen, as well as a larger mound in the bottom right corner. Several smaller mounds and fence posts are also present. The results of object removal using OPALS Robfilter are displayed in Figure 4-8b. Large amounts of the humans and the large mound have been removed. The smaller mounds are however still present, as well as the edges around the larger mound, the feet of the humans and bottom ends of fence posts. The results of the CloudCompare roughness method (Figure 4-8c) are very similar to the results of the OPALS Robfilter. The remaining portions of the objects are only slightly smaller. The final method, LASground, performs the best and is therefore selected, as can be seen in Figure 4-8d.

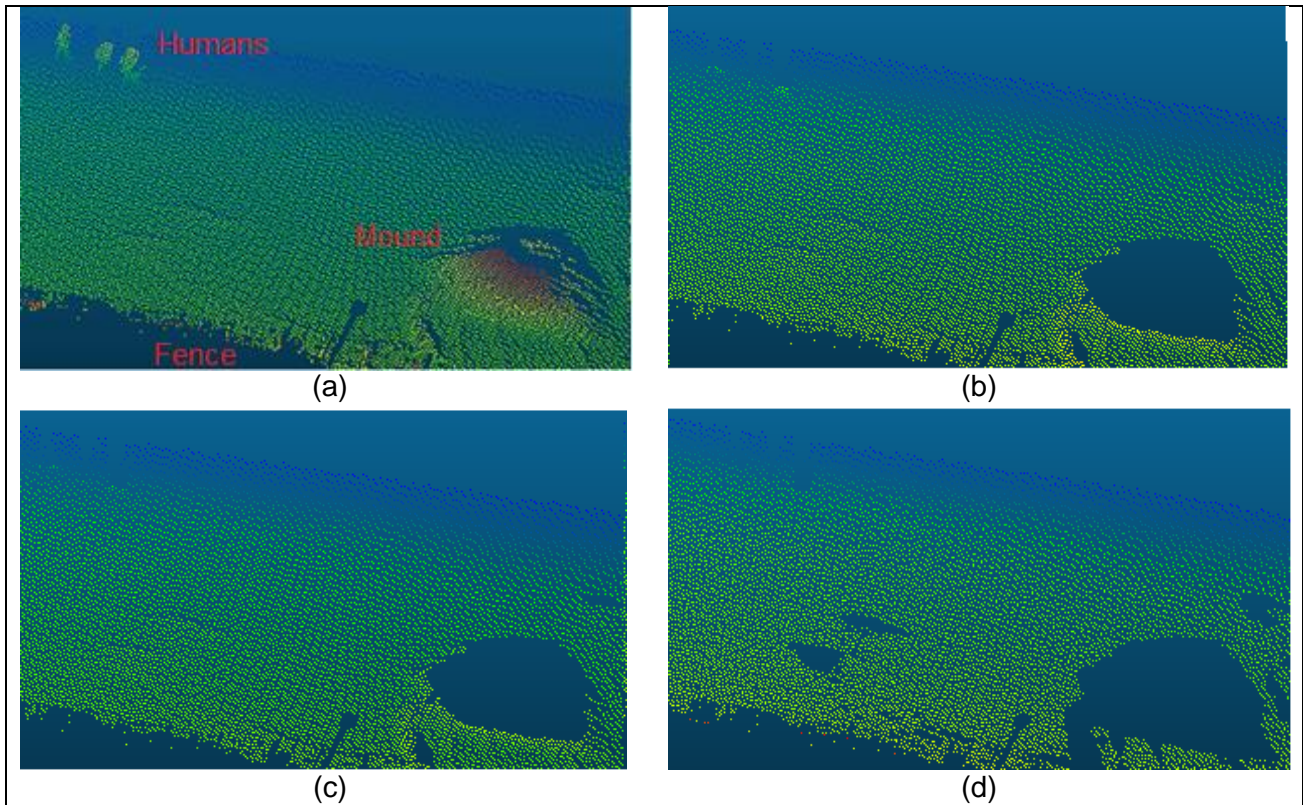


Figure 4-8: Results of object removal methods: Original cloud (a), OPALS Robfilter (b), CloudCompare roughness (c) and LASground (d). In the original cloud, three humans are visible in the top left corner, as well as a fence and a mound in the bottom right corner.

The remaining surface is now completely flat, and no more traces of any of the objects can be observed. This method does however introduce larger spatial holes in the data. When further comparing this result to a cloud which was cleaned by hand, it was found that the chosen method is more accurate than removal by hand, since object points close to the ground are difficult for humans to distinguish from terrain points.

Several interpolation methods were evaluated for the interpolation of the data between the points in the point cloud. By interpolating the data, a continuous cross-section can be taken from any location in the point cloud. For the different interpolation methods (see Table 4-3), a visual check was performed by taking a cross-section through multiple point clouds. The results displayed a very non-smooth looking cross-section using method C. Slopes in the cross-section were represented as blocky stairs. Methods B and E introduced high outliers by the edges of the cross-section. The smoothest looking cross-sections were achieved by the methods using linear interpolation (A and D) which displayed no odd blocky stairs or outliers by the edges. The effect of the outliers in methods B and E can be seen in the second column of Table 4-3. The areas under the cross-section are notably larger than those of the other methods. The final column of Table 4-3 represents the computation time of different methods. The method with the highest computation time is represented as 100%, with the other methods expressed as a percentage of that time.

Method	Area [m ²]	Computation time [%]
Method A (linear)	320.72	92.84
Method B (nearest neighbour)	332.74	78.78
Method C (cubic spline)	322.35	100
Method D (linear)	320.72	93.34
Method E (nearest neighbour)	332.74	78.95

Table 4-3: Area under cross-section and computation times for different interpolation methods. Area represents the area under the cross-section. Computation times are expressed relative to the longest computation time.

As can be seen, the fastest methods are the nearest neighbour interpolations. The linear interpolation methods that resulted in the best visual results are considerably slower but are however still selected as they do not introduce anomalies in the data.

Tests with different amounts of points to interpolate have been performed using the selected interpolation method (see Table 4-4) and were performed on multiple point clouds. Increasing the amount of points to interpolate leads to a more accurate representation of the data but increases computation time. The area under the cross-section of the largest number of interpolation points that was tested is represented by 100%. The areas under the cross-section for the smaller number of points are expressed as a percentage of this area. In similar fashion, the computation times have been expressed as percentages. A consideration was made between accurate data representation and computation time, leading to selection of 100,000 points to interpolate along the cross-section. On average, the area under the curve was only 0.00413% smaller than the highest number of interpolation points, whereas the computation was approximately 10 times faster.

Number of points to interpolate	Area [%]	Computation time [%]
10	69.20	9.70
100	98.11	9.64
1000	99.79	9.22
10000	99.97	9.20
100000	99.99	10.20
1000000	99.99	19.03
10000000	100	100

Table 4-4: Area under cross-section and computation times for different amounts of interpolated points. Area is expressed relative to the result using the most interpolation points. Computations times are expressed relative to the longest computation time.

To further decrease the computation times, the point clouds are subsampled. First, the point clouds of the beach are cropped down to a square in which the cross-section of interest lies. This leads to a reduction of points of roughly 90%. Several different amounts of subsampling have been tested on several of the remaining point clouds (see Table 4-5). The first column gives the interpoint distance after subsampling. As can be seen in the remaining columns, choosing a larger interpoint distance leads to a lower computation time but also to less representative results. This is why the most representative result is chosen, with an interpoint distance of 0.1 m. The area under the cross-section is 0.01128% smaller than the original, but computation times are reduced by roughly 20%.

Interpoint distance [m]	Area [%]	Computation time [%]
Original	100	100
0.1	99.98	81.95
0.25	99.94	75.75
0.5	99.79	48.07
1	99.66	39.79
2	98.55	17.24
3	98.64	14.93

Table 4-5: Results of subsampling. Area represents the area under the cross-section relative to the original point cloud. Computation times are also expressed relative to the computation time of the original cloud.

An overview of the entire processing procedure is presented in Figure 4-9. After processing of the data, cross-sections could be extracted at will.



Figure 4-9: Data processing overview.

4.4. Cross-section extraction

Timeseries of 132 cross-sections from 01-01-2017 until 25-05-2017 have been extracted from the prescribed transects by selecting a daily low tide scan. To illustrate the quality of the obtained cross-sections, an example series of 4 consecutive days has been plotted in Figure 4-10. Preceding this timeseries is a storm, on January 13th/14th. The movement of incoming sand bars can clearly be observed. Contrary to the relatively dynamic intertidal zone, the supratidal beach remains static. No objects remain on the beach, and it is perfectly smooth save for a small perturbation at the upper limit of January 23rd. The initial analysis will be performed on transect 1, however the remaining three transects will also be elaborated.

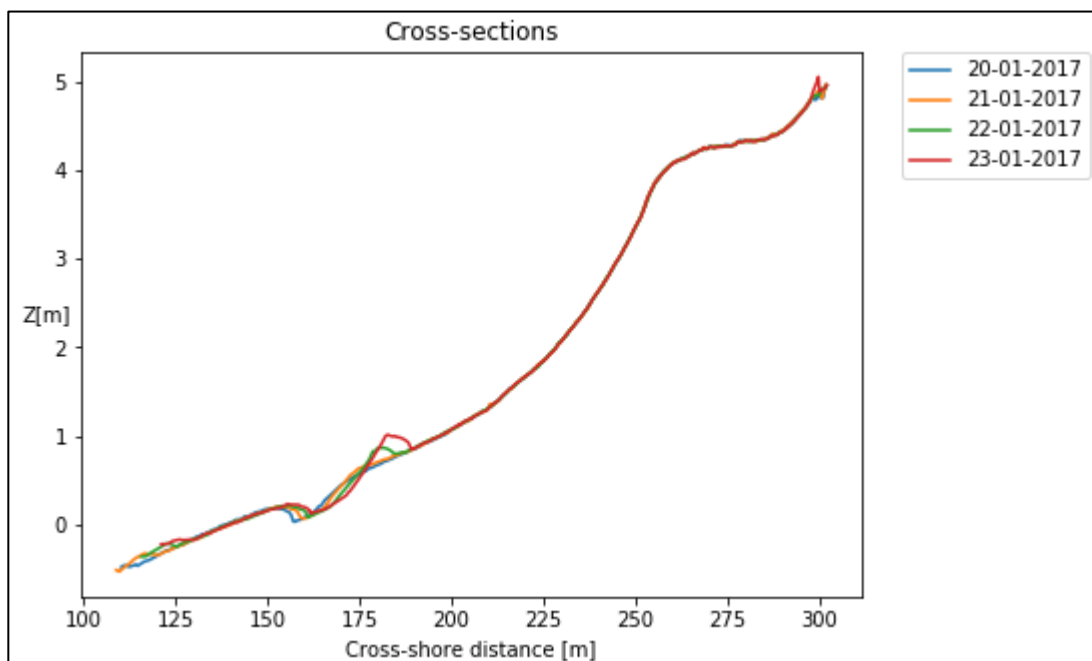


Figure 4-10: Example timeseries of extracted cross-sections from 4 consecutive days. Bar movement is clearly visible.

4.5. Analysis

By exporting the elevation values of all cross-sections to colours and plotting them side by side, a time stack image has been constructed (Figure 4-11). Data concerning the tidal envelope, wave height and wind velocity have been plotted in Figure 4-12. In Figure 4-11 the migration of sand bars as was also seen in Figure 4-10 is visible both through the change in the depth contours and changing colours in the figure. After the storm of January 13th, the NAP+0.5 m. line can be seen moving landward with time. Between the NAP+0 m. and NAP+0.5 m. contour lines in this period, the trailing edge of the bar can also be seen in purple, migrating landward. Until another storm hits at February 23rd, multiple small incoming sand bars are also observed in this area between NAP+0 m. and NAP+0.5 m. This bar migrates at a fairly constant rate, regardless of the tidal neap-spring cycle. The bars observed in the lower intertidal zone are also completely submerged during every high tide, regardless of the tidal neap-spring cycle.

Between the NAP+0.5 m. and NAP+1.5 m. contour lines, little activity is visible right after the storm of January 13th. Starting only around January 22nd, a swash bar starts to develop during neap tide (1), which rapidly grows and moves towards the beach. In only four to five days, this bar grows

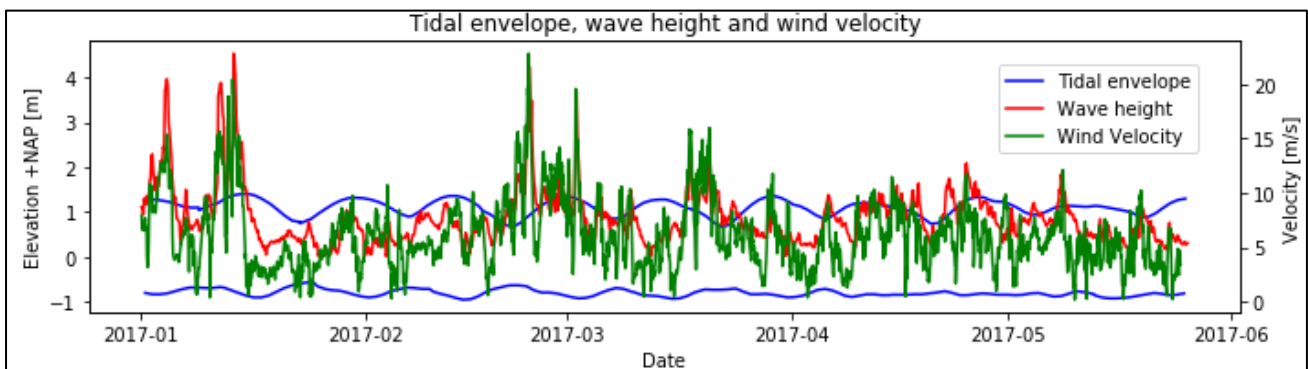


Figure 4-12: Tidal envelope, wave height and wind velocity throughout the research period. Wave height and tidal envelope are plotted on left-hand y-axis, wind velocity on the right-hand y-axis.

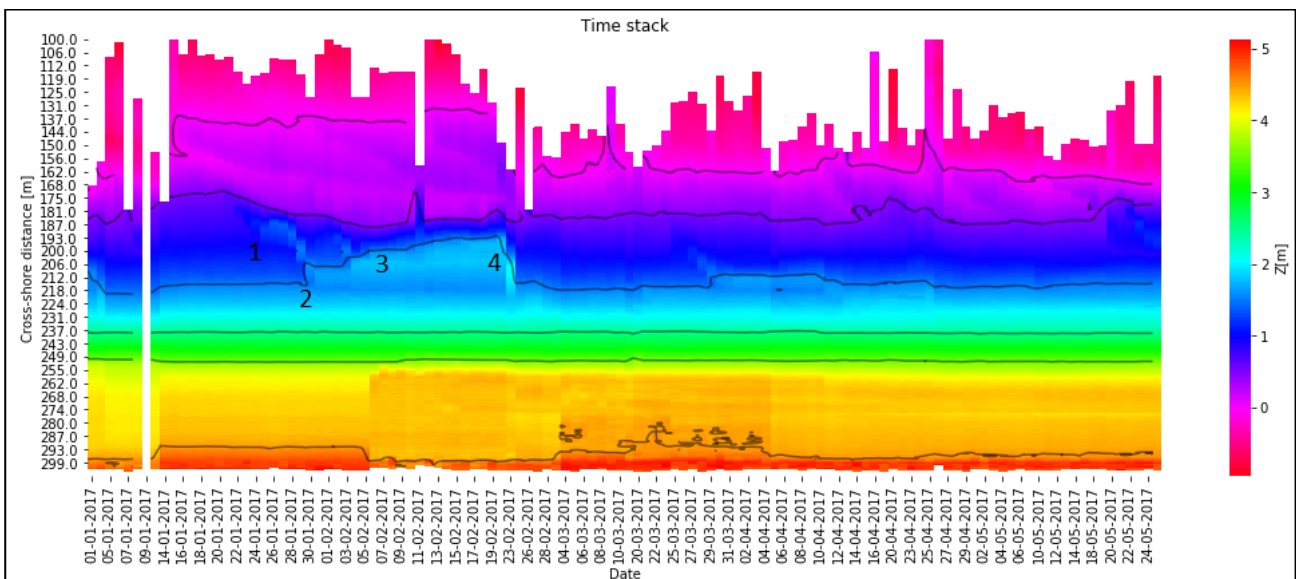


Figure 4-11: Time stack of all cross-sections. Colour scale represents elevation. Contour lines have been added in black, at NAP+0 m., NAP+0.5 m., NAP+1.5 m., NAP+2.5 m., NAP+3.5 m. and NAP+4.5 m. 1: Formation of bar during neap tide. 2: Bar attaches to beach during spring tide. 3: Bar expands in offshore direction. 4: Bar eroded due to storm.

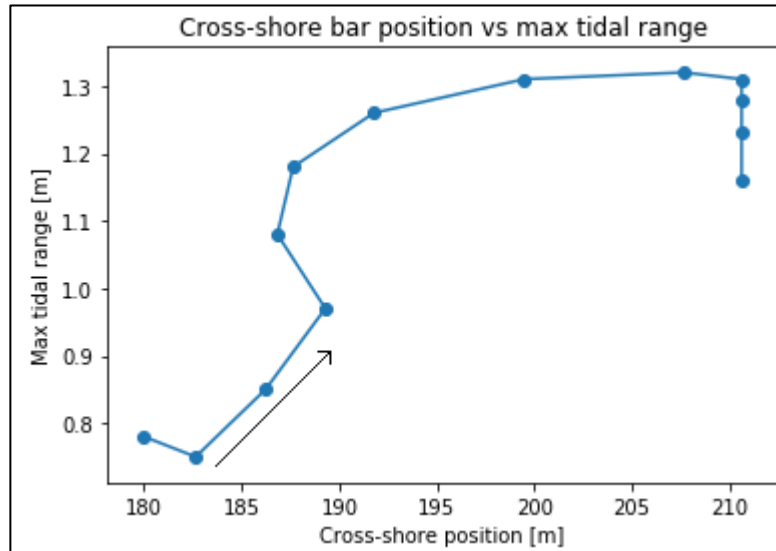


Figure 4-13: Cross-shore position of bar peak versus the increasing maximum of the tidal range in time. Arrow indicates passage of time.

vertically by 0.5 m. After it reaches the beach, it welds to it (2) and extends the beach (3). This can be seen by the NAP+1.5 m. contour line moving offshore until the storm of February 23rd (4). In its migration towards the beach, the bar rises simultaneously with the neap-spring tidal cycle. The bar welds to the beach during spring tide, where it continues to develop offshore, but no longer onshore. This observation is in line with the observations of Kroon & Masselink (2002), which states a relation between onshore movement of bars and the increasing tidal range from neap to spring tide, and the effect of swash in the spring-neap cycle. The migration in time of the peak of this bar has been plotted versus the increasing tidal range in Figure 4-13, for 13 consecutive days. The bar can be seen migrating onshore as the tidal range increases. The one instance of offshore movement that can be seen in the figure is not an actual movement of the sand bar, but rather a steepening of the bar which displaced its peak. The days before spring tide, the bar migrates at an increased rate, before coming to a halt as the tidal range starts dropping. During its migration, the peak of the bar is always located above the maximum high water level, indicating the migration occurs as a result of swash motion. Besides the increasing tidal range, wave and wind conditions also show a positive trend during the migration of the bar. At the end of March, another small intertidal bar migrates onshore and welds to the beach. The bar is smaller, grows less and migrates slower than the bar from Figure 4-13. When checking the conditions in Figure 4-12, the bar migrates onshore during the tidal cycle from spring to neap tide whilst wind and wave conditions display a sudden increase. These observations suggest the tidal cycle has a significant effect on the migration of intertidal bars, influencing both migration and growth rates.

The higher elevation contour lines display little variation in the period of January 13th–February 23rd, however an odd feature can be observed on February 5th, where the area between the NAP+3.5 m. and NAP+4.5 m. lines abruptly changes. After examination of the cross-sections, it was found that the upper section of the beach was flattened. Checking the point cloud on this date confirmed the presence of bulldozers on the beach, which could be seen actively moving around sand.

After the storm of February 23rd, the NAP+0 m. contour line has significantly moved onshore. The bars that were present between the NAP+0 m. and NAP+0.5 m. contours have disappeared, and the extension of the beach around the NAP+1.5 m. line has also eroded. Once again, the contour lines at higher elevations remain largely unchanged. Remarkable is the NAP+0.5 m. line that does

not change position much as compared to prior to the storm. It is possible that the large volume of sand that was eroded from the beach extension has contributed to keeping this line at the same position. A second storm on March 1st erodes the last remaining portion of the beach extension but has little effect on other contours as the time between the two storms was quite short. After this storm, some small incoming sand bars can once again be observed, be it much smaller and shorter lasting than the bars prior to the February 23rd storm. These bars move independently of the tidal cycle. From the NAP+4.5 m. line can be concluded that the sand on the flattened section of the beach is also shifting.

The various sand bars that are visible in the data are of various sizes and migrate at different speeds. Ruessink et al (2009) describes the relation between sand bar migration and water depth. Water depth influences the cross-shore position where waves break and thereby sand bar migration. In deeper water, the influence of the waves passing over the bar is smaller than in shallower water. This is observed in the data by a much slower bar migration rate in the NAP-1 m. to NAP+0 m. region where the average water depth is larger than in the NAP+0 m. to NAP+1 m region. In the period between January 20th and February 5th, a relatively small bar migrates onshore and displaces the NAP+0.5 m. depth contour shoreward by 16 m. At a higher elevation, a larger bar migrates onshore by 30 m. in 9 days between January 20th and 29th, between the NAP+0.5 m. and NAP+1.5 m depth contours. These migration rates are smaller than the onshore migration that was observed at Duck (Hsu et al, 2006), yet are still quite high. Ruessink et al (2009) proposes a relation between water level and sand bar migration for a shoreline in the northern Gold Coast region: a shift in sand bar position of 10-15 m. is accompanied by a change in water level of 1 m. Similar rates are not observed in Figure 4-11, where the larger bar between January 20th and 29th moves at a faster rate than this relation, and the smaller bar between January 20th and February 5th moves at a slower rate. Due to these large differences, such a relation could at best only be applicable between adjacent depth contours but could not be applied to compare bars at significantly different elevation levels at this beach.

Ruessink et al (2009) also states a suspicion about bar variability being dominated by storm response. A recommendation is made to further investigate influencing factors on this behaviour, as they are still unknown. Based on this data, one could both agree and disagree with the suspected relation. It is clearly true that storm events reset sand bar position and thereby greatly influence their variability. However, between consecutive storms, sand bars can both migrate and grow at considerable rates and even weld to the beach. This underlines the influence of calm conditions on the variability of sand bars.

4.5.1. Envelope and variability

The mean in time and envelope of all cross-sections are presented in Figure 4-14. As is expected, the envelope is very slim around the backshore, where the cross-sections were corrected to. The intertidal zone, where much of the bar migration takes place, displays a much wider envelope. The contours of the various sand bars are clearly visible. The green lines in this plot indicate chosen zones of interest (the intertidal zone, the backshore and the foredune). The lower reach of the intertidal zone (below $z=0$) is disregarded due to low data quality, which can be seen from the mean profile and envelope at this location. The envelope in the foredune area is wide mostly as a result of the flattening of the terrain that was done by bulldozer. The envelope and the variability plot presented in Figure 4-15 display the range of elevations that have occurred over the research

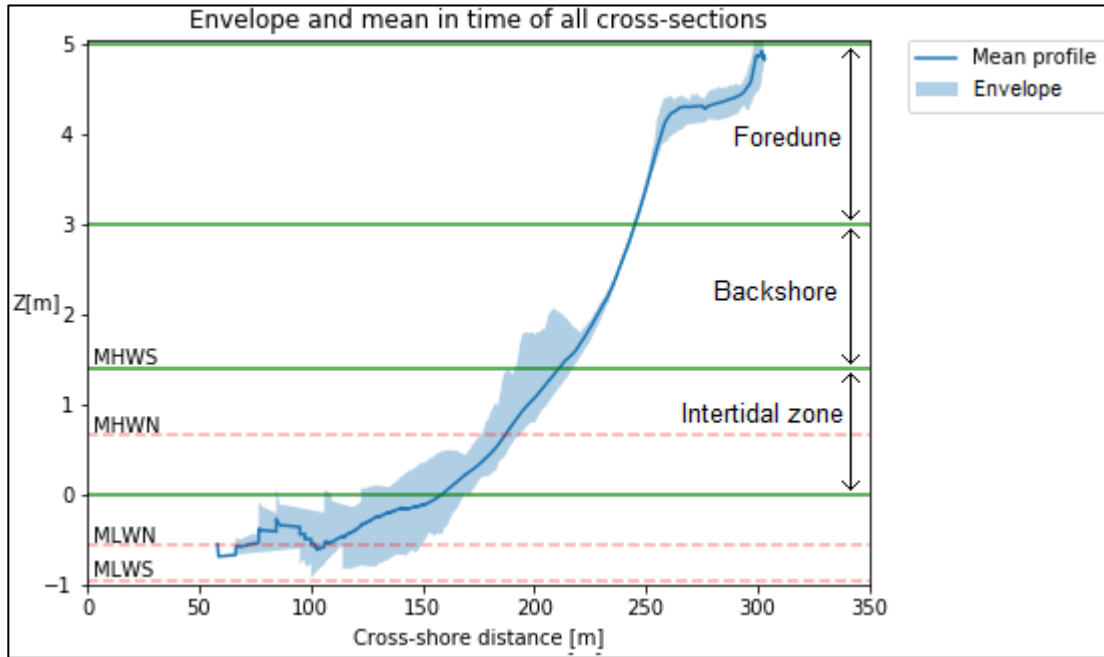


Figure 4-14: Mean in time and envelope of all cross-sections. The green lines divide the cross-section into intertidal zone, backshore and foredune. The lower region of the intertidal zone (below $z=0$) is discarded due to low data quality. Red dotted lines indicate various water levels.

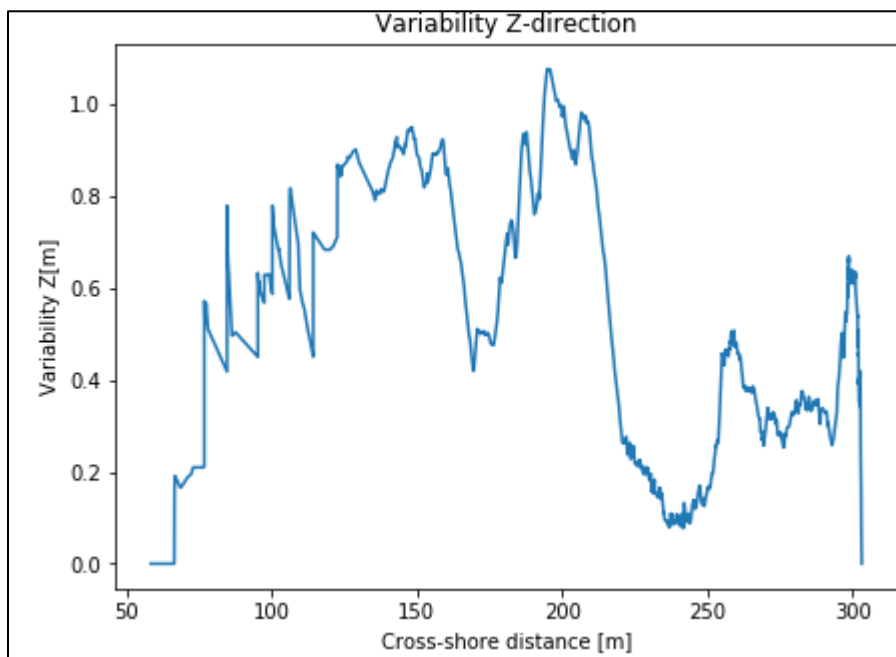


Figure 4-15: Variability plot of the beach.

period. Especially in the intertidal zone, this variation can easily exceed 0.5 m. with extremes of over 1 m. variation in vertical direction. The low variation in the backshore is partially explained by the correction of the profiles that was applied using the average elevation of this zone. It is however also explained by the lack of marine influence in this region and the occurrence of sand armouring, limiting aeolian transport from this region (Iversen and Rasmussen, 1994). It can now clearly be seen that the variability is higher in the foredune area than in the backshore. As was explained, this is likely a consequence of the flattening of the terrain where the volume was redistributed over the area.

The found variability is especially large due to the accurate daily measurement of sand bars. When comparing this variability to the variability on yearly timescale as found by de Vries (2013), it can be seen that the yearly variability is lower than the timescale used in this research. Using yearly measurements, individual migrating sand bars will not be captured nearly as often, thereby reducing the chance of finding a higher variability. This illustrates the influence of sand bars on beach variability (and growth).

4.5.2. Depth contour variation

The changing depth contours that were observed (Figure 4-11) have been studied further by plotting the cross-shore position of various elevation levels (Figure 4-16). The NAP+0 m. contour moves significantly offshore (~20 m.) after the January 13th storm which is indicated by the first red line. This indicates deposition of eroded beach volume from higher up in the profile has outweighed the erosion that actually occurred at this elevation. It then hardly changes position until the second storm hits on February 23rd, where it moves onshore by approximately the same distance. This indicates erosion at this elevation has now outweighed deposition of eroded sand from higher up in the profile. For the remainder of the research period, the NAP+0 m. line hardly changes, despite the occurrence of a third storm on March 1st.

The NAP+0.5 m. contour also moves offshore during the January 13th storm. A steady onshore directed migration can be seen following this storm, which is caused by the incoming sand bar that was identified in Figure 4-11. The February 23rd and March 1st storms do not seem to affect the position of the NAP+0.5 m. contour too much, indicating a balance between erosion at this elevation and accretion due to eroded sand from higher up in the profile. Sine-shaped motions in the cross-shore position of this contour can be seen around April 17th and at the end of the timeseries, indicating another shorter cycle of accretion/erosion caused by sand bar migration.

The NAP+1 m. contour does not move offshore during the January 13th storm as much as the previously discussed contours. A sudden jump in position of this contour is visible at January 22nd, after the incoming swash bar starts to weld to the beach. The cross-shore position shifts by around 15 m. onshore in a day. It then follows the trailing edge of the bar as it continues moving onshore, until the bar has fully welded to the beach around February 4th. Until the February 23rd storm, the NAP+1 m. contour then moves offshore as the beach extension continues to accrete. The following storms then erode the beach extension and push the contour offshore once again.

The pattern in the NAP+1.5 m. contour position is very similar to that of the NAP+1 m. It also does not erode much during the January 13th storm and displays an offshore jump followed by a steady offshore migration that indicates accretion due to bar welding. The February 23rd storm then pushes the NAP+1.5 m. contour offshore by approximately 25 m., and the entire beach extension is eroded in combination with the March 1st storm. A small offshore jump occurs around the end of March, when a small sand bar once again starts welding to the beach. During the remainder of the research period, this bar is slowly eroded.

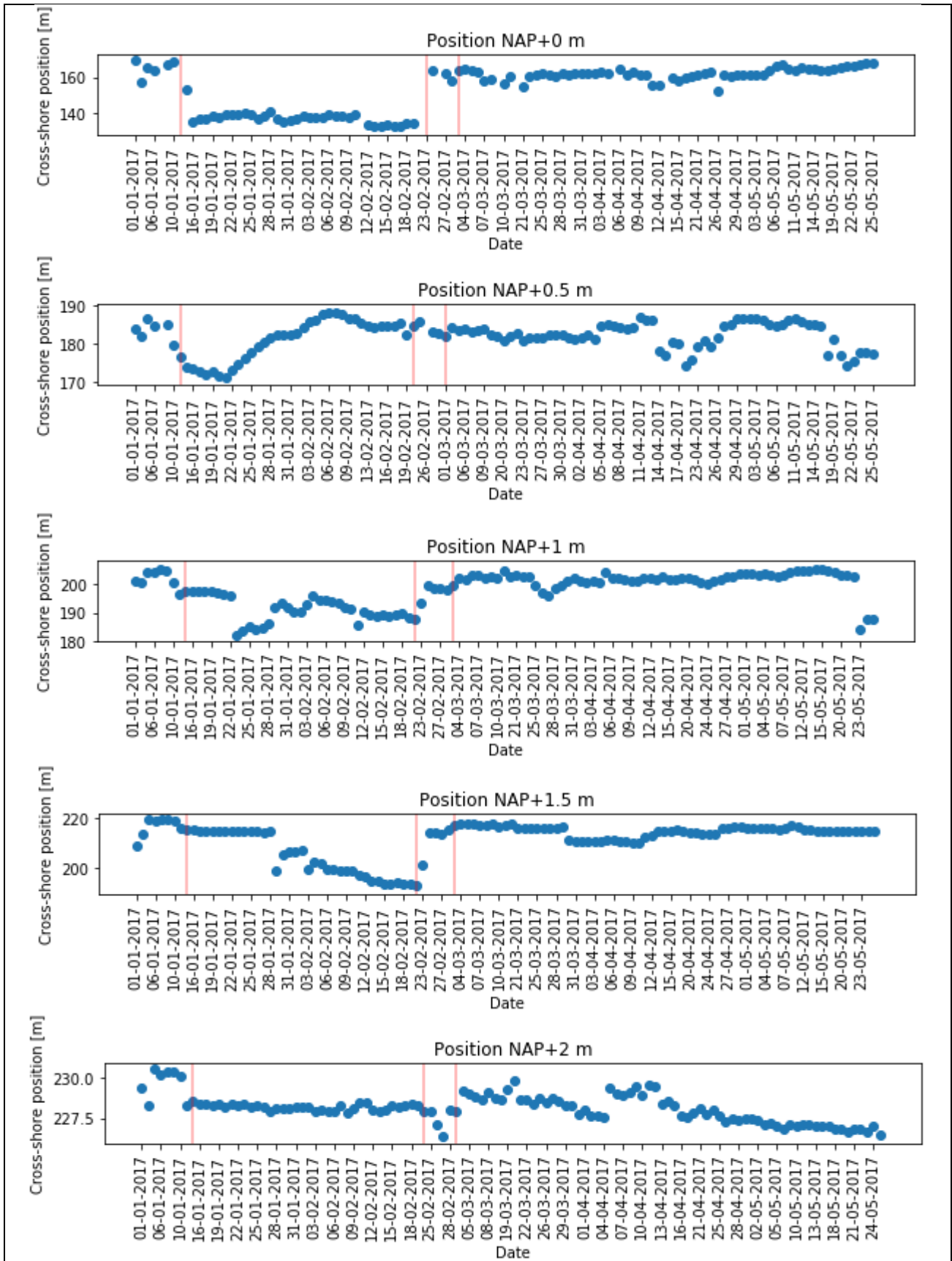


Figure 4-16: Cross-shore position of various elevation levels. Red lines indicate storms.

Starting from the NAP+2 m. contour and up until the NAP+2.5 m., the scale of the erosion and recovery effects becomes smaller and smaller. The NAP +2 m. contour does still show small changes (in the order of several meters) as response to storm erosion and beach growth. The NAP+3 m. and NAP+3.5 m. contours display an opposite response to the January 13th storm, where the positions of the contours move onshore by approximately 1 m., indicating erosion has occurred at these elevations. These observations follow the beach erosion theory of Vellinga (1982). Contours from NAP+4 m. and up once again show slight offshore movement, indicating the possibility of accretion by run up during the storm.

The behaviour observed in Figure 4-16 illustrates both different responses to individual storms over the entire profile, as well as differences in response during a single storm between the various depth contours. The January 13th storm generally moved all the contours below NAP+2.5 m. offshore, whereas the following storms moved these contours back onshore. The beach growth that occurs after storms can be observed clearly by the shifting contour positions in time. Various accretion rates can be observed both within the same period of recovery, and between separate recovery periods. The storm erosion that was observed higher up in the profile is of similar magnitude as was found on a French coast by Suanes et al (2012). High on the backshore, the profile moved onshore by 1 m. The foredune accretion during the storm that was found in the data was also observed in this article, though be it much larger than was observed in this research.

4.5.3. Beach volume distribution

The distribution of the volume in time has been computed for both the total cross-section and the zones of interest as indicated in Figure 4-14 (intertidal zone, backshore and foredune) by computing the area under the cross-section in the respective zones and multiplying it by 1 m. in longshore direction. The resulting distributions for these zones have been plotted in Figure 4-17. Storms are indicated by vertical red lines, linear trends by black lines. The uncertainty that was found in the measurement accuracy in section 4.1 in the form of a standard deviation translates to an uncertainty of +/- 11.71 m³ ($\sigma = 4.78$ cm.) in the computed volumes at the location of this transect (computed using the mean in time of all cross-sections at this location). During the January 13th storm, the intertidal zone does not lose much in volume at all. The incoming intertidal bars following the storm cause the volume in this area to increase in time, until a large bar is pushed onto the backshore, causing a drop in the intertidal volume. The February 23rd storm induces no erosion in this region, but rather leads to a short period of growth until the March 1st storm. After this storm, the volume remains fairly constant, displaying variations due to the minor incoming sand bars.

The backshore also does not display erosion during the January 13th storm. After the storm, it initially does not change much until January 27th, when the large bar from the intertidal zone starts entering the backshore. The two storms that follow cause significant erosion, completely eroding the gained volume of the bar. Until the end of the research period, the volume now remains quite stable. The foredune area displays a slight accretion during the January 13th storm. This confirms earlier observations of run up during the elevated water levels of the storm that has deposited sediment high up in the profile. The flattening of the foredune by bulldozer that occurred on February 6th caused a slight deviation in the volume (marked by the red box in the figure). During the following days, when the works had ended, the volume kept decreasing only to regain its pre-bulldozing volume after a week. The following storms have little effect on the foredune area and a slight positive trend continues until the end of the research period.

When regarding the cumulative volume of all three zones, the main features that stand out are the period of beach growth just before the February 23rd storm, and the decrease in volume due to this storm, which reduced the cross-sectional volume by about 25 m³. The general shape of the cumulative volume distribution has a similar shape to that of the backshore, stressing the influence of bar migration on the total volume of a transect. The small variations that are visible between the two distributions are the result of small incoming sand bars in the intertidal zone that influence the total volume.

The wellness of the fitted linear trends is indicated by R² values (Table 4-6). The values are all quite low, with a maximum of 0.28 (28% of the variance can be explained by linear trend). This indicates that in general, the variability of the volumes dominates over the plotted linear trend. In the graphs this is reflected by the majority of the data points not lying on or near the trend line. It appears that at this temporal scale, too much variability of the volume is present for a trend to exist. The many sand bars that come in to the beach have a large influence on the volume signal. These bars are however very dynamic, varying in migration speed and volume and are eroded by storms, removing large volumes instantaneously, causing a large variability of the signal. When regarding larger time scales, such as monthly for several consecutive years (Suarez et al, 2012) or yearly for several decades (de Vries, 2013), much higher levels of linearity are found. Performing analysis at such temporal scales does not allow for variation in the signal caused by individual intertidal bars or storms, thereby obtaining a temporal signal containing much lower levels of noise. Since no large linear trends were found, a check was performed to see if there were any higher order trends present in the volumes, which was not the case.

Region	R ² value
Intertidal zone	0.03
Backshore	0.10
Foredune	0.28
Cumulative	0.12

Table 4-6: R² values for the plotted linear trends.

The volumetric signals display some forms of wave-like motions, which is why a Fourier analysis was performed to get an impression of the cycle time of these motions. The resulting peak frequencies are presented in Table 4-7. Noteworthy points are the identical peak frequencies for the backshore, foredune and total volume, indicating their volumes change on the same time scale. The cycle time of the intertidal zone deviates from this frequency and is shorter. To observe if the cycle times of the volumes correspond to cycle times of the various boundary conditions, a Fourier analysis was also performed on the obtained wave, wind and tide data (Table 4-8). No immediate relations between the two tables appear to be present, however the cycle time obtained for the tidal elevation at least proves the used approach produces accurate results.

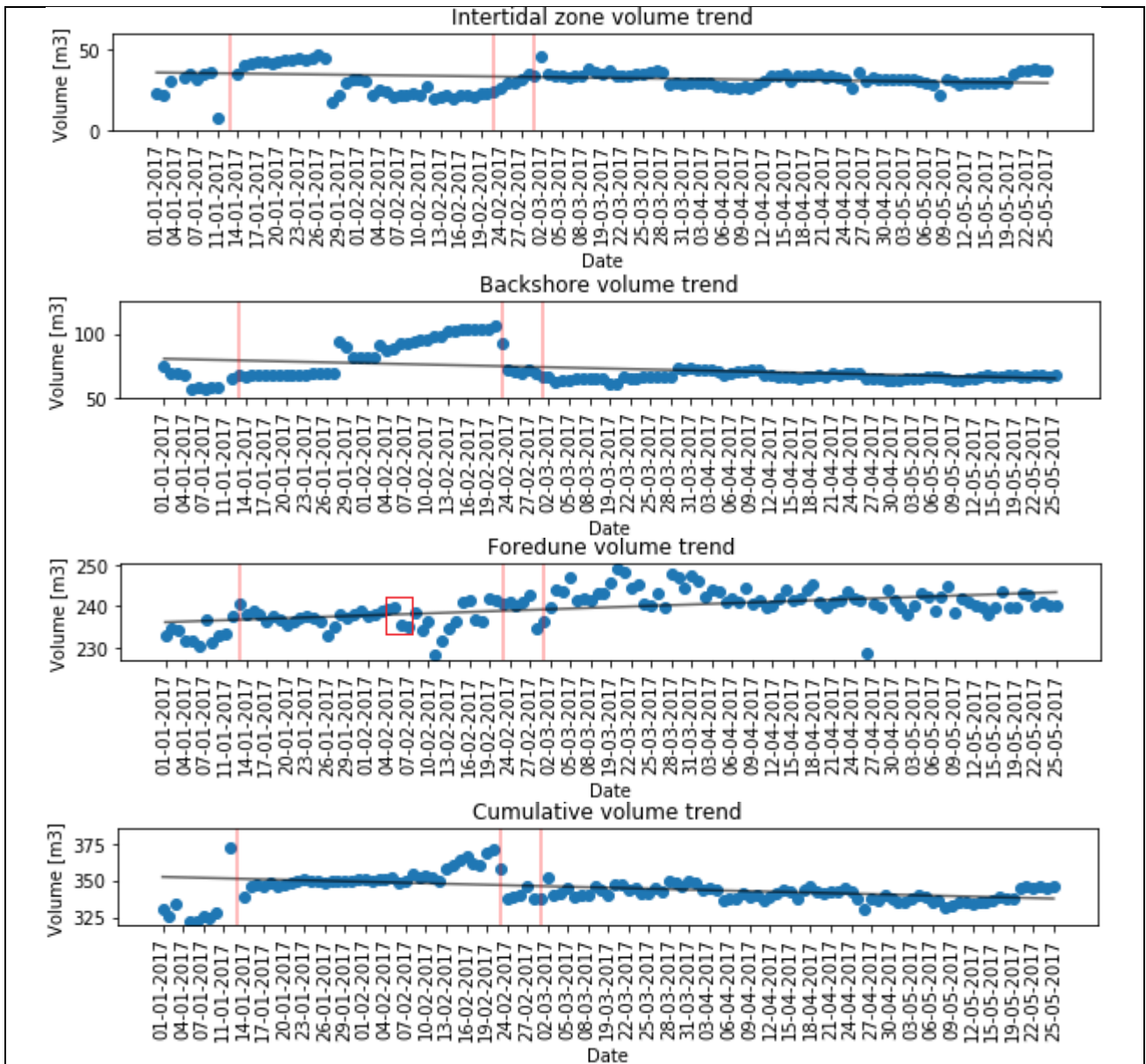


Figure 4-17: Volume distributions of the intertidal zone, backshore, foredune and the cross-sectional total. Red lines indicate storms. Black line indicates the linear trend. Red box indicates effect of bulldozing.

Region	Peak frequency [cycles/day]	Cycle time [days]
Intertidal zone	0.015	67
Backshore	0.0075	133
Foredune	0.0075	133
Cumulative	0.0075	133

Table 4-7: Results of Fourier analysis on the volume signals.

Variable	Peak frequency [cycles/day]	Cycle time [days]
Wave height	0.021	48
Wave direction	0.0069	145
Wave period	0.021	48
Wind velocity	0.041	24
Wind direction	0.021	48
Tide	1.93	0.52

Table 4-8: Results of Fourier analysis on the boundary conditions.

To further investigate the presence of relations between volume change and forcing, Pearson's correlations were computed between the rate of volumetric change and the boundary conditions (wave, wind and tide). No significant correlations were found (an example of a scatter plot is given in Figure 4-18). This is not unexpected since a wide variety of factors is responsible for beach growth. A combination of factors such as sediment availability, water depth and wave height would have a much larger influence on accretion rates than wave height by itself. Literature (such as Suanez et al, 2012) also finds no relation between accretion rates and boundary conditions and stresses the complex and dynamic nature of beach morphology that can hardly be linked to an isolated driving force. The data obtained by TLS is no exception to this. The lack of correlations to tide imply the tide is mainly responsible for displacement of the surf and swash zones on this individual transect. Since tide is described to have a larger influence on longshore transport, it is not unexpected to see this result for a single transect.

Correlations were also determined between the volumetric change rates of the different zones of interest (intertidal zone, backshore and foredune). Only one significant correlation was found, between the intertidal zone and the backshore. The value of the Pearson's correlation coefficient is -0.45, indicating a moderate correlation between the volumetric changes of these areas. This correlation is in line with observations of swash bars migrating out of the intertidal zone and onto the backshore.

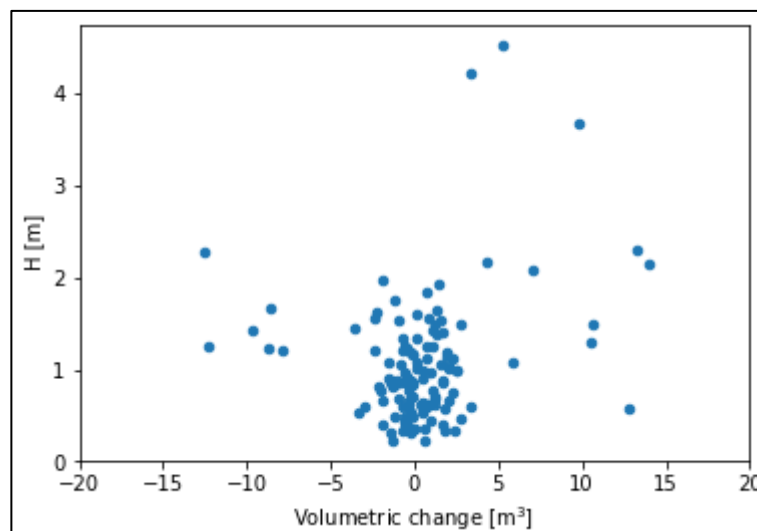


Figure 4-18: Scatter plot of volumetric change vs wave height H.

4.5.4. Results all transects.

The individual results of all transects as has just been elaborated for the first transect are available in appendix A. At all transect locations, bar migration can clearly be identified from the data, though there is a degree of variation. Key events such as the welding of the large bar and the bulldozing of the foredune are present at all transects, however variation occurs in the migration patterns of smaller bars and depth contours. To illustrate this variability, the longshore minimum and maximum position of several depth contours have been plotted in Figure 4-20. As can be seen, the depth contours do not migrate similar distances everywhere. Transect 2, which is located between two sand bars shows the smallest amount of variability, with an average migration distance of just over 20 m. The depth contours seem to migrate the most at transect 4, where distances are well over 30 m. The similar shape of the plots gives an impression of the shape of the beach and the variation of position of the waterline. The shortest transect is clearly transect 4, whereas the other transects extend further into the sea. This is also reflected in the cross-shore length of the different transects (Figure 4-19), where the cross-shore length of the profiles is determined within the upper and lower limits of the volume computation as has been defined in Figure 4-14 ($z=0$ and $z=5$). The mean cross-shore length of transect 4 is significantly lower than that of the remaining transects.

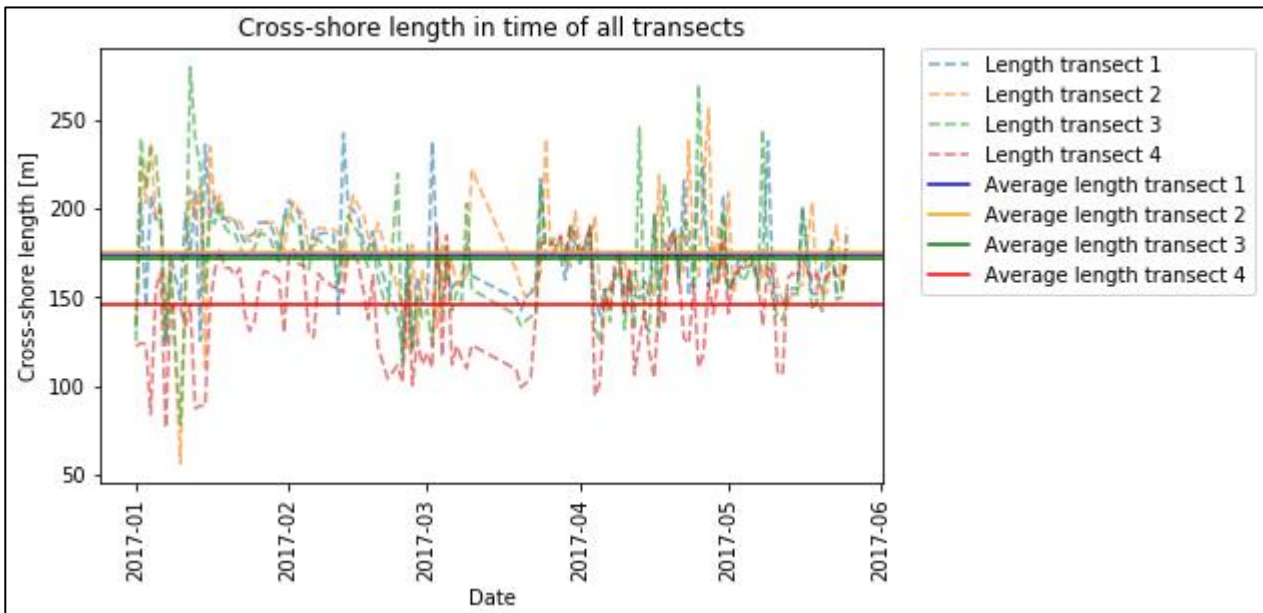


Figure 4-19: Cross-shore length in time of all transects, as well as the mean.

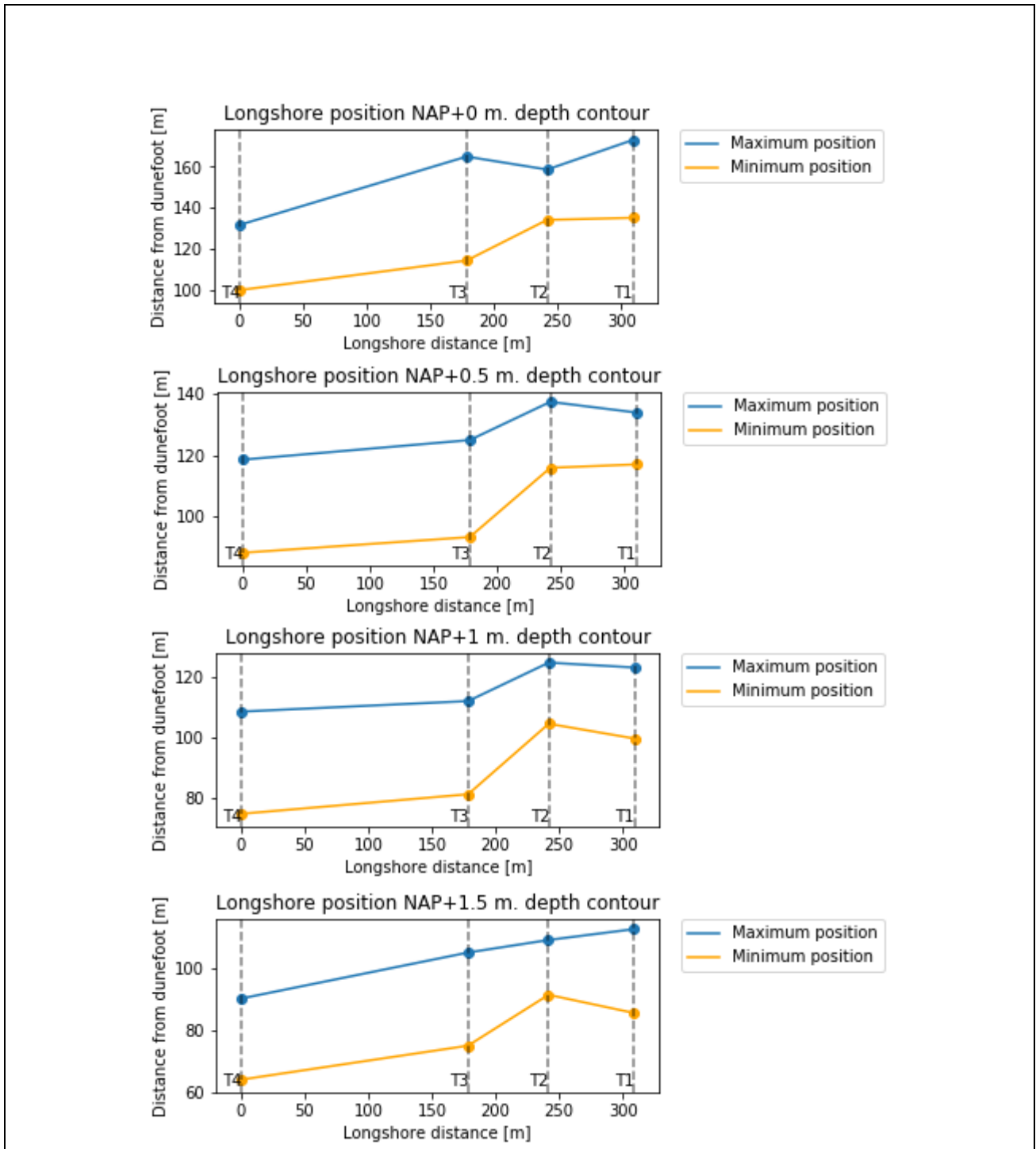


Figure 4-20: Longshore position of depth contours. Blue lines indicate the maximum offshore position. Orange lines indicate the minimum onshore position. Transects are indicated by dotted lines.

When comparing the volume distributions in time of the different transects, the reduced size of transect 4 as compared to the others is once again visible (Figure 4-21). It is however the only transect to display a moderate positive volumetric trend in time. Within this 300 m. stretch of beach, responses are quite variable. The growth observed prior to the February 23rd storm at transect 1 appears to otherwise only be present at transect 2. Transect 3 remains quite stagnant and transect 4 even displays erosion. Transects 1 and 2 lose a significant volume during the February 23rd storm, while transects 3 and 4 lose much less (as marked by D in Figure 4-21). A similar shape of the volume distribution is found for transects 1 and 2. Even though transect 3 is about the same distance from transect 2 as transect 1 is, it does not follow this shape. Starting in April, an ongoing erosion occurs at this location. The different volumetric distributions observed in these plots are an indication of the variability of the coast, and different responses to storms and recovery on this timescale. The degree to which growth occurs varies greatly. Whilst one transect is growing, a transect 100 m. further down the coast may even display erosion. When considering the mean of all transects it becomes clear that growth during this research period is mainly a local and temporary feature, that is reset during storms. Over the entire research period, there does not appear to be a large net difference in the mean volume. The mean profile has gained 2.6 m³ over the entire research period. Over the course of nearly six months, barely any net growth of the beach has occurred, despite the nearby Sand Motor providing sediment. The presence of the Sand Motor may however have contributed to limiting the net erosion as result of the occurring storms. During storms, the energetic and elevated water will sometimes be picked up by the laser scanner. These points are much higher than the level of the actual terrain, leading to spikes in the volume such as the ones marked by A and B in Figure 4-21. Some of the scans were found to have a lower quality, causing spatial holes in the data. These holes locally caused the volume to not be accurately measured, leading to lower values (as marked by C in Figure 4-21). In March, a system malfunction caused no measurements to be taken for eight consecutive days (marked by E in Figure 4-21), causing a temporal gap in the data.

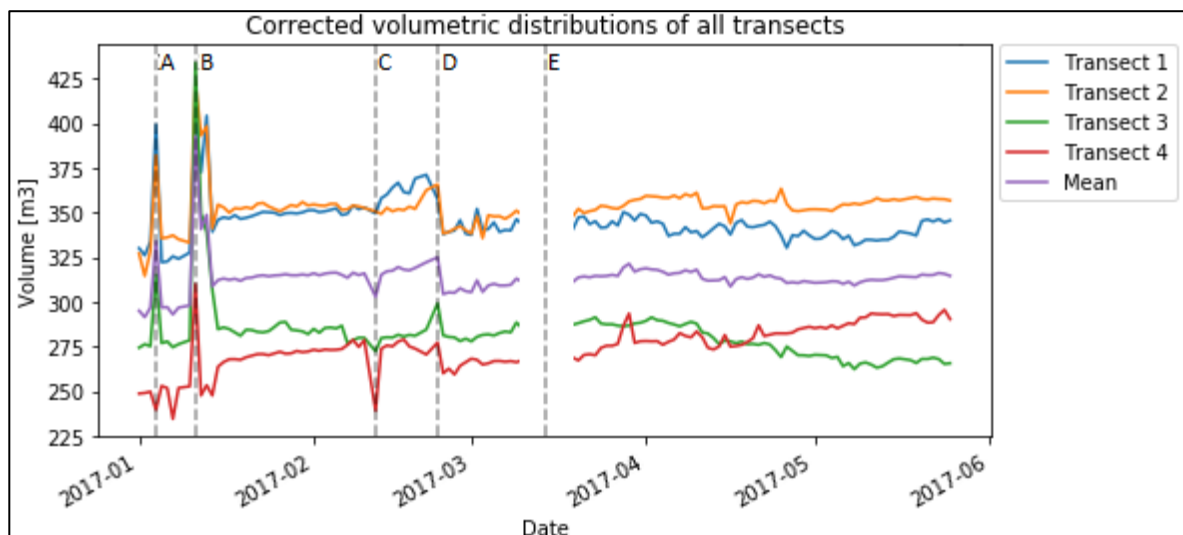


Figure 4-21: Volumetric distributions of all transects. Dashed vertical lines indicate events. A&B: Erroneous interpolation to points on sea surface during storm. C: Low quality scan causing large holes on some sections of the beach, less volume measured. D: Storm erosion. E: System bug lead to no measurements for eight days.

To illustrate the effects of the applied correction method, Figure 4-21 has been reproduced without applying the correction in Figure 4-22. As can be seen, the signals contain more fluctuations, but the order of magnitude of the volume and the general trend remain the same for each transect.

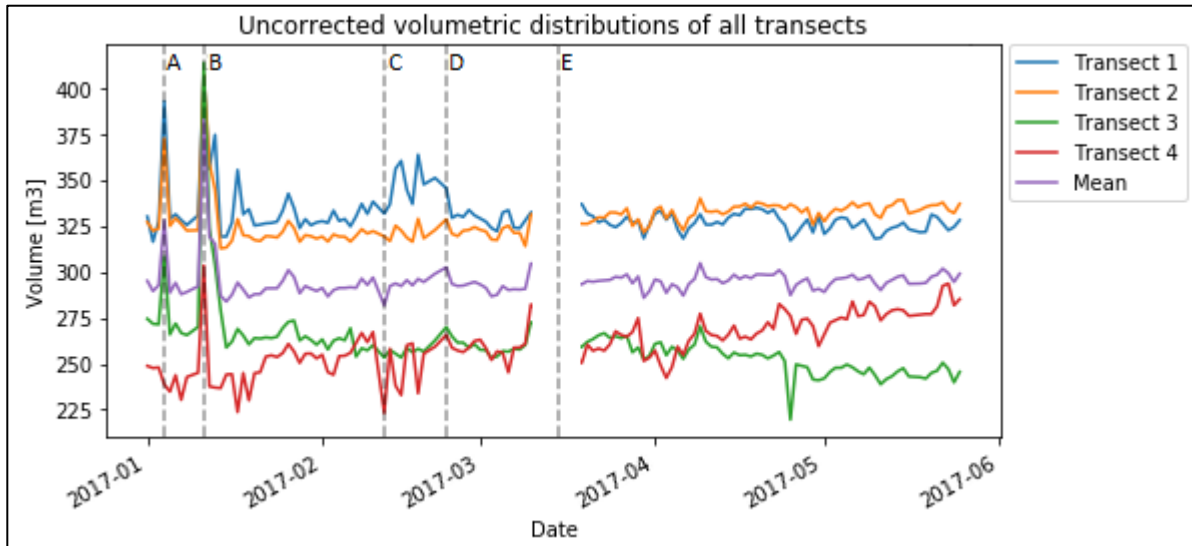


Figure 4-22: Uncorrected volumetric distributions of all transects. Dashed vertical lines indicate events. A&B: Erroneous interpolation to points on sea surface during storm. C: Low quality scan causing large holes on some sections of the beach, less volume measured. D: Storm erosion. E: System bug lead to no measurements for eight days.

When regarding the quality of the fitted linear trends for the corrected distributions in Figure 4-21 (Table 4-9), transects 1 through 3 all display poor linear behaviour, indicating dominance of morphologic variability over trend. However, transect 4 does display moderate linear growth. This transect started out shorter than the other transects and has been growing throughout the period, even during periods when other transects did not. By the end of the research period, around 45 m³ has accreted at this transect as compared to January 1st.

Region	Transect 1	Transect 2	Transect 3	Transect 4
Intertidal zone	0.031	0.0023	0.13	0.55
Backshore	0.10	0.063	10 ⁻⁶	0.83
Foredune	0.28	0.15	0.34	0.24
Cumulative	0.12	0.034	0.17	0.59

Table 4-9: R² values of the linear trend fitted for all transects.

Comparing the results of the Fourier analysis that was performed on the volume distributions of all transects (Table 4-10) it stands out that only a few different magnitudes are present. The most frequently occurring motion is a slow one, with a cycle time of around 133 days. Even though the transects respond differently, only 3 main motions seem to occur.

Region	Transect 1 [days]	Transect 2 [days]	Transect 3 [days]	Transect 4 [days]
Intertidal zone	67	67	45	133
Backshore	133	134	45	133
Foredune	133	67	67	133
Cumulative	133	67	67	133

Table 4-10: Results of Fourier analysis for all transects. Values indicate cycle time in days of the peak frequency motion in the volumetric distribution.

Similar to transect 1, not many significant correlations were found between the volume changes and boundary conditions. More significant correlations were found between volume changes between the different regions (Table 4-11). A significant negative correlation is often found between the intertidal zone and backshore, once again confirming the link between the two. Correlations higher up in the profile are more rarely found. In this case, this is possibly a result of the applied correction method, however not applying any correction would also lead to a lack of correlation due to the unpredictable, unnatural and rapid increase and decrease of the volume caused by the instability of the laser. Only when a correction method is applied that compensates for the instability can the behaviour in the upper profile be accurately studied.

Region	Transect 1	Transect 2	Transect 3	Transect 4
Intertidal zone – Backshore	-0.45	-0.54	-0.70	
Intertidal zone – Foredune		-0.85		
Backshore – Foredune		0.35		-0.25

Table 4-11: Significant (p -value < 0.05) Pearson correlation coefficients between volumetric changes between zones of interest.

5. Conclusions, discussion and recommendations

5.1. Conclusions

In this thesis, the growth of a South Holland beach was studied on sub-annual timescale using data obtained from a terrestrial laser scanner. From this data, timeseries of one low tide scan per day for 132 consecutive days were extracted. The most important conclusions that can be drawn from this report are presented in this paragraph.

After investigation of various processing techniques, a framework for the processing of the TLS data was developed that includes noise detection and removal, object filtering, interpolation and subsampling. These steps were found necessary to be able to extract clean cross-sections that only represent terrain from the point clouds, as the point clouds especially contained many objects. Using timeseries of these cross-sections, morphological change can be accurately observed. During processing of the data, a rotational instability of the scanner was found and corrected. The correction method did however not allow for further study of aeolian effects and thereby limited growth study of backshore and foredune. The measurement accuracy that was found (standard deviation of 1.51 cm. at 86 m.) is suitable to map beach morphology changes (migration rates of up to 8 m. in a day).

By studying the timeseries and volumetric distributions, it was found that patterns of bars and troughs are present throughout the dataset and are the primary driver of beach growth on the regarded time scale. These patterns emerge during calm conditions and are reset during storm events. When a bar enters the intertidal zone, the total volume of a transect increases by the amount of sediment in the bar. As the bar continues to grow, the total volume grows. Especially when bars weld to the beach, a significant volumetric growth occurs through accretion of the seaward slope. The erosion caused by a large storm that occurred during the research period was quite significant and could clearly be observed, with an erosion pattern that is in line with that of Vellinga (1982).

Attempts to link volumetric changes to changes in wave, wind and tidal properties through correlation and Fourier analysis did not produce any results. The data obtained by the TLS is no exception as literature also fails to correlate these factors (Suanez et al, 2012). However, by further examining the data, some observations regarding these processes can still be made. An instance of a migrating swash bar was studied which migrated onshore during the tidal cycle from neap to spring tide and welded to the beach during spring tide (as was also found by Kroon & Masselink, 2002). After the tidal range started decreasing again, this bar no longer migrated as it was no longer exposed to marine conditions, but instead continued expanding in offshore direction due to swash effects and significantly influenced the total volume of the beach. This particular bar migrated and grew much faster than a different swash bar which migrated onshore during the spring to neap tidal cycle. This observation showcases the role of tide in the migration of swash bars, and thereby beach growth. It also shows that despite a daily decrease in tidal range, a swash bar can still continue migrating if wave and wind conditions are strong enough for overtopping of the bar to occur. Due to the correction method that was applied on the rotational instability of the scanner, accretion of backshore and foredune could no longer be accurately studied. The small fluxes of aeolian transport ($O(\text{mm-cm})$) are outweighed by the elevation corrections that were applied.

Due to the great level of morphological variability on this time scale, hardly any significant linear or higher order trends were found in the volumetric distributions of the different transects. This is not in line with studies that use monthly (Suarez et al, 2012) or annual (de Vries, 2013) data. Even though periods of beach growth were observed, over the entire research period only a small amount of beach growth occurred. The mean volumetric distribution of all transects had gained $2.6 \pm 0.29 \text{ m}^3$ over the entire research period of nearly six months, whereas one particular transect gained $20 \pm 2.2 \text{ m}^3$ in less than one month. Due to the various storms that occurred throughout the research period, this accretion was however largely eroded. In longshore direction, response to incoming bars and storms varied significantly. Even whilst one transect may be accreting, a transect 150 m. downcoast can be eroding. Two of the researched transects did not experience a significant net change in volume or cross-shore length during the research period, indicating these transects may have reached an equilibrium. One transect that started out with smaller cross-shore length than the others, gained more volume throughout the research period and lost less volume during storms, whereas the longer transects often had their gained volume completely eroded.

5.2. Discussion

Based on prior testing (Vos et al, 2017), it was expected that the accuracy of the laser would be high enough to capture morphological change. The accuracy found in this report is however lower. The method used to determine the standard deviation is a simplified one, and leaves room for improvement. A method needs to be used to accurately determine the relation between standard deviation and distance from the scanner. The standard deviation found in this report is not perceived to be unsuitable to investigate change in beach morphology due to its magnitude relative to the observed morphological change. Further improvement of the standard deviation can be reached by utilizing a more accurate correction of the found rotational instability of the scanner. The method that was used in this report allows for the study of especially the intertidal zone, but limits study on the upper profile. It also artificially introduces deviations in the terrain that will lead to a higher standard deviation.

It is important to quantify the uncertainty in the obtained measurements. In the analysis of transect 1, the standard deviation of 1.51 cm. at 86 m. was translated to 4.78 cm., which in turn lead to an uncertainty in volume of $\pm 11.71 \text{ m}^3$ (3.4% of the mean total volume of transect 1). This mean volume does however still include the unreliable data below $z=0$, which was not included in the total volume of the transect. The real volumetric uncertainty would therefore be smaller if this effect is considered. Since transect 1 is located the furthest from the laser scanner, the standard deviations for the remaining transects are smaller (T2: $\sigma = 3.93 \text{ cm.}$, T3: $\sigma = 3.73 \text{ cm.}$, T4: $\sigma=4.39 \text{ cm.}$) and will therefore lead to a smaller uncertainty in the obtained volumes. Besides uncertainty caused by the standard deviation of the measurement, the applied method of processing will also influence the final result and thereby introduce uncertainties. The effects of interpolation, subsampling and the correction method were therefore also quantified. By comparing the obtained volume of the chosen method of interpolation to the mean volume of all compared methods, it was found that the chosen method differs by 1.4 %. The effect of the chosen level of subsampling was already quantified in the report and amounted $1.6 \cdot 10^{-4} \%$. To quantify the effect of the correction method, the mean volumes of all transects were determined before and after correction. The differences between these volumes was less than 10 % in all cases (T1: 4.06 %, T2: 6.82 %, T3: 8.16 %, T4: 5.45 %). The

combined volumetric uncertainties of standard deviation, interpolation, subsampling and correction range from 8.86 % for transect 1 to 13.46 % for transect 3. These values translate to volumes in the order of magnitude of 30-40 m³. It is however believed that the actual uncertainty is lower than this, as the uncertainty in the correction method also contains the natural variation of the backshore, the volumetric uncertainty due to standard deviation still includes the unreliable reach below z=0, and the standard deviation found in this report is larger than the one found by Sander Vos (1 cm. per 100 m. in longshore direction).

Considering the location of the study site, just north of the Sand Motor, one could reasonably expect to see some form of net beach growth. The fact that this has not occurred is noteworthy. It is possible that without the presence of the Sand Motor, the beach would have eroded. This erosion could now have been compensated by the presence of the Sand Motor. A net accretion of less than 5 m³ over a six-month period is however still very small. These observations regarding beach growth could possibly be improved by regarding (many) more transects along the beach. This would also improve correlation results and allow for verification of individual cross-sections by comparing them to their close neighbours.

In this thesis, a 3D data set was used to perform a 2D analysis. This simplification means a loss of potential information. To evaluate the extent to which this happens, the events that were researched in the volumetric distribution (Figure 4-21) are further examined in the 3D point clouds. It was found that these large and relevant events (erroneous data points on water due to storms, low quality scans and storm erosion) are accurately captured in 2D. When intertidal bars approach the coastline, they often appear in multiple transects. Storm erosion is simultaneously visible at all transects. These events all have a cross-shore component and can therefore be measured by taking cross-sections. Longshore transport can however not be monitored in this fashion. This includes longshore migration of bars, as well as their shape and size, and longshore sediment transport. These will influence the volumetric distributions at location of the cross-sections, but their effects are not distinguishable from cross-shore transport when only regarding cross-shore transects.

The observed migration of intertidal bars generally followed observations made in the literature. An unexpected result was however the onshore migration of a sand bar in the spring to neap tidal cycle. Due to descending water levels, one would expect the migration to come to a halt as the bar is no longer submerged. The combination of elevated wind and wave action seem to have caused a situation in which the top of the bar was still overtopped, continuing the onshore movement. To accurately determine if the wave height was indeed high enough to overtop the bar, the nearshore wave conditions at 11 m. water depth that were used in this report should have been translated to a shallower water depth using wave models such as SWAN.

5.3. Recommendations

The biggest improvement of the scan results can be made by accurately correcting the rotational instability of the scanner. This would lead to a more accurate representation of reality, unlike the artificial correction utilised in this report. Checking the accuracy of the TLS after this correction will likely lead to a smaller standard deviation, as stationary objects that can be used for this check now display less variation in position. To fully map the accuracy of the device, reflectors should be placed, or stationary objects should be selected at various ranges. This allows for the effect of

distance on the standard deviation to be studied, so that it can be accounted for when taking more distant cross-sections from the scans. A check of the data versus GPS which was not performed in this thesis should also be made to validate the TLS measurements.

In this report it was investigated why extracted cross-sections were not all of the same length. The data was of lower quality in the lower intertidal zone, displaying either lack of data or erroneous data. No explanation for this phenomenon was found, however to increase information gain from the TLS in the future, it may be interesting to further investigate why this occurs and if it can be improved upon.

An analysis using many more cross-sections would provide stronger conclusions and insight into beach morphology on this time scale. Taking a cross-section for every 1 m. width of the beach would capture nearly all morphological change that occurs. Observing behaviour in larger numbers will increase support for conclusions and allow for verification of individual transect results by comparing them to neighbours. By using the approach prescribed in this thesis, cross-sections can be extracted from the data at will, allowing for such an analysis if sufficient computational power is available.

This report has made use of low resolution hourly TLS data. The CoastScan project was set up with the analysis of this data in mind. However, a daily high-resolution scan is also performed, at a fixed daily time. Since these high-resolution scans are more detailed and therefore contain more information than the low-resolution scans, it may be interesting to time these high-resolution scans to be performed during low tide. A longer stretch of coast is then measured, possibly providing more insight and information. If odd behaviour is discovered in the low-resolution scans, it can then be checked versus the high-resolution scans to possibly discover the source of this disturbance. Performing the entire analysis using the high-resolution data will however require much more computational power.

The observations made in this thesis open doors to many other analyses. Data can be clustered in time or space to be studied in more detail. The three dimensional behaviour of bars in the intertidal zone can accurately be monitored, with great temporal and spatial resolution. Though the dunes were not analysed in this thesis, they have been measured and can therefore be investigated. Monitoring of works performed on the beach such as the bulldozing of the dune foot can be performed and quantified to investigate if works are accurate, effective or stay within the legal limits. The many objects that are present in this data set can also be studied. Especially larger objects that are present for a longer period of time will influence transport of sand towards the dunes. If trapped volumes become too large, this sand is often removed and dumped elsewhere. Studies can be performed to determine where this sand should be dumped to contribute to beach/dune growth. The dataset does however include many months during the stormy season and relatively few during the calmer season. To fully investigate beach resilience it may be interesting to extend the research period to at least one year, so that a complete image of both erosive and accretive periods is reached. The effect of storms on the beach is clearly visible. The Dutch coast however experiences relatively mild storms as the North Sea is sheltered by Great Britain. It may therefore be interesting to relocate the laser scanner to a beach that is exposed to an ocean, to further study storm erosion and recovery.

In this thesis, an attempt was made to link volumetric change on the beach to boundary conditions. This was however done using all the data over the entire research period. The same was done when attempting to fit linear trends. Almost no significant correlations, matching peak frequencies or strong linear trends were found. Some preliminary tests have however displayed more promising results when clustering the data in time before attempting to compute correlations, peak frequencies and fitted trends. Distinction can be made by identifying calm and energetic periods from the data, or periods of accretion/erosion or little to no change. It may therefore be interesting for future study to perform these tests on clustered data.

Bibliography

AHN. (2017). *Elevation map of the Netherlands*. Last visited February 15, 2018, from

<https://ahn.arcgisonline.nl/ahnviewer/?extent=-126585.9771%2C333617.466%2C428557.5332%2C583147.5651%2C28992>

Angelopoulou, E., & Wright Jr, J. R. (1999). Laser scanner technology.

Bagnold, R.A., 1941. *The Physics of Blown Sand and Desert Dunes*. Methuen, London, 256 pp.

Bauer, B. O., & Davidson-Arnott, R. G. (2003). A general framework for modelling sediment supply to coastal dunes including wind angle, beach geometry, and fetch effects. *Geomorphology*, 49(1-2), 89-108.

Boehler, W., Vicent, M. B., & Marbs, A. (2003). Investigating laser scanner accuracy. *The International Archives of Photogrammetry, Remote Sensing and Spatial Information Sciences*, 34(Part 5), 696-701.

Bosboom, J., Stive, J.F. (2015). *Coastal dynamics I. Lecture notes CIE4305*. Delft, the Netherlands: Delft Academic Press.

K. L. Brodie, B. Raubenheimer, Steve Elgar, R. K. Slocum, J. E. McNinch, "Lidar and Pressure Measurements of Inner-Surfzone Waves and Setup", *Journal of Atmospheric and Oceanic Technology*, vol. 32, pp. 1945, 2015, ISSN 0739-0572.

Castelle, B., Bujan, S., Ferreira, S., & Dodet, G. (2017). Foredune morphological changes and beach recovery from the extreme 2013/2014 winter at a high-energy sandy coast. *Marine Geology*, 385, 41-55.

CBS. (February 9, 2018). *Gemiddelde bevolking; geslacht, leeftijd, burgerlijke staat en regio*. Last visited February 15, 2018, from

[http://statline.cbs.nl/Statweb/publication/?VW=T&DM=SLNL&PA=70233NED&D1=0&D2=0&D3=0-101&D4=\(1-6\)-I&HD=180215-1415&HDR=T,G3&STB=G1,G2](http://statline.cbs.nl/Statweb/publication/?VW=T&DM=SLNL&PA=70233NED&D1=0&D2=0&D3=0-101&D4=(1-6)-I&HD=180215-1415&HDR=T,G3&STB=G1,G2)

Cowell, P. J., Stive, M. J., Niedoroda, A. W., de Vriend, H. J., Swift, D. J., Kaminsky, G. M., & Capobianco, M. (2003). The coastal-tract (part 1): a conceptual approach to aggregated modeling of low-order coastal change. *Journal of Coastal Research*, 812-827.

Davidson-Arnott, R. G.D., & Law, M. N. (1990). Seasonal patterns and controls on sediment supply to coastal foredunes, Long Point, Lake Erie. *Coastal dunes: form and process*, 177-200.

Davidson-Arnott, R.G.D., Yang, Y., Ollerhead, J., Hesp, P. a., Walker, I.J., 2008. The effects of surface moisture on aeolian sediment transport threshold and mass flux on a beach. *Earth Surf. Process. Landforms* 33, 55–74.

De Vries, S., 2013. *Physics of Blown Sand and Coastal Dunes*.

Durán, O., Claudin, P., & Andreotti, B. (2011). On aeolian transport: Grain-scale interactions, dynamical mechanisms and scaling laws. *Aeolian Research*, 3(3), 243-270.

Elfrink, B., & Baldock, T. (2002). Hydrodynamics and sediment transport in the swash zone: a review and perspectives. *Coastal Engineering*, 45(3-4), 149-167.

Esri. (2018). *Classify LAS noise*. Last visited July 23, 2018, from <http://pro.arcgis.com/en/pro-app/tool-reference/3d-analyst/classify-las-noise.htm>

- Hejbudzka, K., Lindenbergh, R. C., Soudarissanane, S. S., & Humme, A. (2010). Influence of atmospheric conditions on the range distance and number of returned points in Leica ScanStation 2 point clouds. In *Proceedings ISPRS Commission V Mid-Term Symposium? Close Range Image Measurement Techniques?, Newcastle upon Tyne, UK, 21-24 June 2010; IAPRS, XXXVIII (5), 2010*. International Society of Photogrammetry and Remote Sensing (ISPRS).
- Hoefel, F., & Elgar, S. (2003). Wave-induced sediment transport and sandbar migration. *Science*, 299(5614), 1885-1887.
- Höfle, B., & Pfeifer, N. (2007). Correction of laser scanning intensity data: Data and model-driven approaches. *ISPRS journal of photogrammetry and remote sensing*, 62(6), 415-433.
- Hofton, M. A., Minster, J. B., & Blair, J. B. (2000). Decomposition of laser altimeter waveforms. *IEEE Transactions on geoscience and remote sensing*, 38(4), 1989-1996.
- Houser, C. (2009). Synchronization of transport and supply in beach-dune interaction. *Progress in Physical Geography*, 33(6), 733-746.
- Houser, C., Greenwood, B., & Aagaard, T. (2006). Divergent response of an intertidal swash bar. *Earth Surface Processes and Landforms: The Journal of the British Geomorphological Research Group*, 31(14), 1775-1791.
- Houser, C., Hapke, C., & Hamilton, S. (2008). Controls on coastal dune morphology, shoreline erosion and barrier island response to extreme storms. *Geomorphology*, 100(3-4), 223-240.
- Houser, C., Wernette, P., Rentschlar, E., Jones, H., Hammond, B., & Trimble, S. (2015). Post-storm beach and dune recovery: Implications for barrier island resilience. *Geomorphology*, 234, 54-63.
- Hsu, T. J., Elgar, S., & Guza, R. T. (2006). Wave-induced sediment transport and onshore sandbar migration. *Coastal Engineering*, 53(10), 817-824.
- Iversen, J. D., Rasmussen, K. R., 1994. The effect of surface slope on saltation threshold. *Sedimentology* 41 (4), 721-728.
- Kawamura, R. (1951). Study on sand movement by wind (Relationship between sand flow and wind friction, and vertical density distribution of sand). *Tokyo Daigaku Rikogaku Kenkyusho Hokoku*, (Tokyo), 5(3), 95-112.
- Kersten, T. P., Sternberg, H., & Mechelke, K. (2005). Investigations into the accuracy behaviour of the terrestrial laser scanning system Mensi GS100. *Proc. in the Optical 3D Measurement Techniques*, 1, 122-131.
- Kroon, A., & Masselink, G. (2002). Morphodynamics of intertidal bar morphology on a macrotidal beach under low-energy wave conditions, North Lincolnshire, England. *Marine geology*, 190(3-4), 591-608.
- Lichti, D. D., & Jamtsho, S. (2006). Angular resolution of terrestrial laser scanners. *The photogrammetric record*, 21(114), 141-160.
- Lindenbergh, R.C., Soudarissanane, S., de Vries, S., Gorte, B., and de Schipper, M., (2011): "Aeolian Beach Sand Transport Monitored by Terrestrial Laser Scanning", *Photogrammetric Record*, 26(136): pp. 384–399 (December 2011), DOI: 10.1111/j.1477-9730.2011.00659.x.

- Masselink, G., & Gehrels, R. (2014). *Coastal environments and global change*. Retrieved from <https://ebookcentral-proquest-com.tudelft.idm.oclc.org>
- Masselink, G., & Hughes, M. (1998). Field investigation of sediment transport in the swash zone. *Continental Shelf Research*, 18(10), 1179-1199.
- Masselink, G., & Puleo, J. A. (2006). Swash-zone morphodynamics. *Continental Shelf Research*, 26(5), 661-680.
- Masselink, G., & Short, A. D. (1993). The effect of tide range on beach morphodynamics and morphology: a conceptual beach model. *Journal of Coastal Research*, 785-800.
- Morton, R. A., Paine, J. G., & Gibeaut, J. C. (1994). Stages and durations of post-storm beach recovery, southeastern Texas coast, USA. *Journal of Coastal Research*, 884-908.
- Pfeifer, N., Stadler, P., & Briese, C. (2001, March). Derivation of digital terrain models in the SCOP++ environment. In Proceedings of OEEPE Workshop on Airborne Laserscanning and Interferometric SAR for Detailed Digital Terrain Models, Stockholm, Sweden (Vol. 3612).
- Riegl Laser Measurement systems GmbH. (December 18, 2017). Riegl-VZ2000i. Last visited March 9, 2018, from www.riegl.com/vz-2000i
- Rijkswaterstaat. (2018a). *Kustonderhoud*. Last visited April 25, 2018, from <https://www.rijkswaterstaat.nl/water/waterbeheer/bescherming-tegen-het-water/maatregelen-om-overstromingen-te-voorkomen/kustonderhoud/index.aspx>
- Rijkswaterstaat. (2018b). *Tidal wave at Hoek van Holland*. Last visited April 25, 2018, from https://getij.rws.nl/getij_resultaat.cfm?location=HOEKVHLD
- Ruessink, B. G. and Jeuken, M. C. J. L. (2002), Dunefoot dynamics along the Dutch coast. *Earth Surf. Process. Landforms*, 27: 1043–1056. doi:10.1002/esp.391
- Ruessink, B. G., Pape, L., & Turner, I. L. (2009). Daily to interannual cross-shore sandbar migration: observations from a multiple sandbar system. *Continental Shelf Research*, 29(14), 1663-1677.
- Sedgwick, P. (2012). Pearson's correlation coefficient. *BMJ: British Medical Journal (Online)*, 345.
- Soudarissanane, S., Lindenbergh, R., Menenti, M., & Teunissen, P. (2011). Scanning geometry: Influencing factor on the quality of terrestrial laser scanning points. *ISPRS Journal of Photogrammetry and Remote Sensing*, 66(4), 389-399.
- Southgate, H. N., 2011. Data-based yearly forecasting of beach volumes along the dutch North Sea coast. *Coastal Engineering* 58 (8), 749 { 760.
- Suarez, S., Cariolet, J. M., Cancouët, R., Arduin, F., & Delacourt, C. (2012). Dune recovery after storm erosion on a high-energy beach: Vougot Beach, Brittany (France). *Geomorphology*, 139, 16-33.
- The Hague Marketing Bureau. Kijkduin. Last visited on April 25, 2018, from <https://denhaag.com/nl/kijkduin>.
- Van der Wal, D. (1999). *Aeolian transport of nourishment sand in beach-dune environments*. Amsterdam University.
- Vellinga, P. (1982). Beach and dune erosion during storm surges. *Coastal Engineering*, 6(4), 361-387.

Voisin, S., Fougou, S., Truchetet, F., Page, D. L., & Abidi, M. A. (2007). Study of ambient light influence for three-dimensional scanners based on structured light. *Optical Engineering*, 46(3), 030502.

Vos, S. E., Lindenbergh, R. C., de Vries, S. (2017). Coastscan: Continuous monitoring of coastal change using terrestrial laser scanning. *Coastal Dynamics 2017*.

Vosselman, G., 2000. Slope based filtering of laser altimetry data. *International Archives of Photogrammetry and Remote Sensing*, XXXII, 153–159.

Vosselman, George Maas, Hans-Gerd. (2010). *Airborne and Terrestrial Laser Scanning*. Whittles Publishing.

Wang, Q., Wu, L., Xu, Z., Tang, H., Wang, R., & Li, F. (2014, July). A progressive morphological filter for point cloud extracted from UAV images. In *Geoscience and Remote Sensing Symposium (IGARSS), 2014 IEEE International (pp. 2023-2026)*. IEEE.

Wiberg, P. L., Drake, D. E., & Cacchione, D. A. (1994). Sediment resuspension and bed armoring during high bottom stress events on the northern California inner continental shelf: measurements and predictions. *Continental Shelf Research*, 14(10-11), 1191-1219.

Wiggs, G.F.S., Baird, a. J., Atherton, R.J., 2004. The dynamic effects of moisture on the entrainment and transport of sand by wind. *Geomorphology* 59, 13–30.

Zhang, K., Chen, S. C., Whitman, D., Shyu, M. L., Yan, J., & Zhang, C. (2003). A progressive morphological filter for removing nonground measurements from airborne LIDAR data. *IEEE Transactions on Geoscience and Remote Sensing*, 41(4 PART I), 872-882. <http://doi.org/10.1109/TGRS.2003.810682>

Zhuang, H., & Roth, Z. S. (1995). Modeling gimbal axis misalignments and mirror center offset in a single-beam laser tracking measurement system. *The International Journal of Robotics Research*, 14(3), 211-224.

Appendix A: Individual analysis results transects 2-4.

Transect 2.

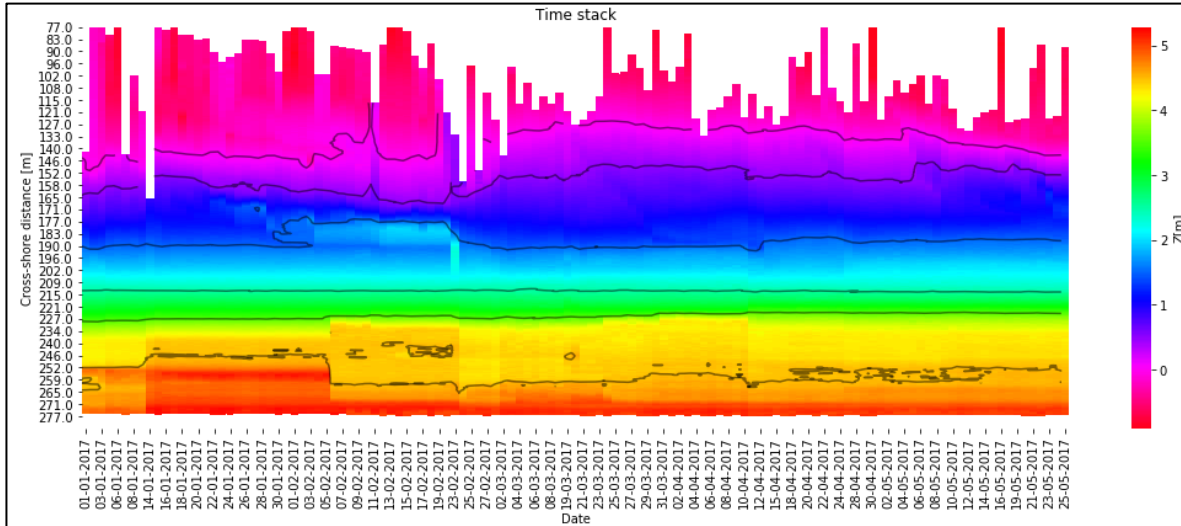


Figure 0-1: Time stack of all cross-sections. Colour scale represents elevation. Contour lines have been added in black, at NAP +0 m., NAP+0.5 m., NAP+1.5 m., NAP+2.5 m., NAP+3.5 m. and NAP +4.5 m.

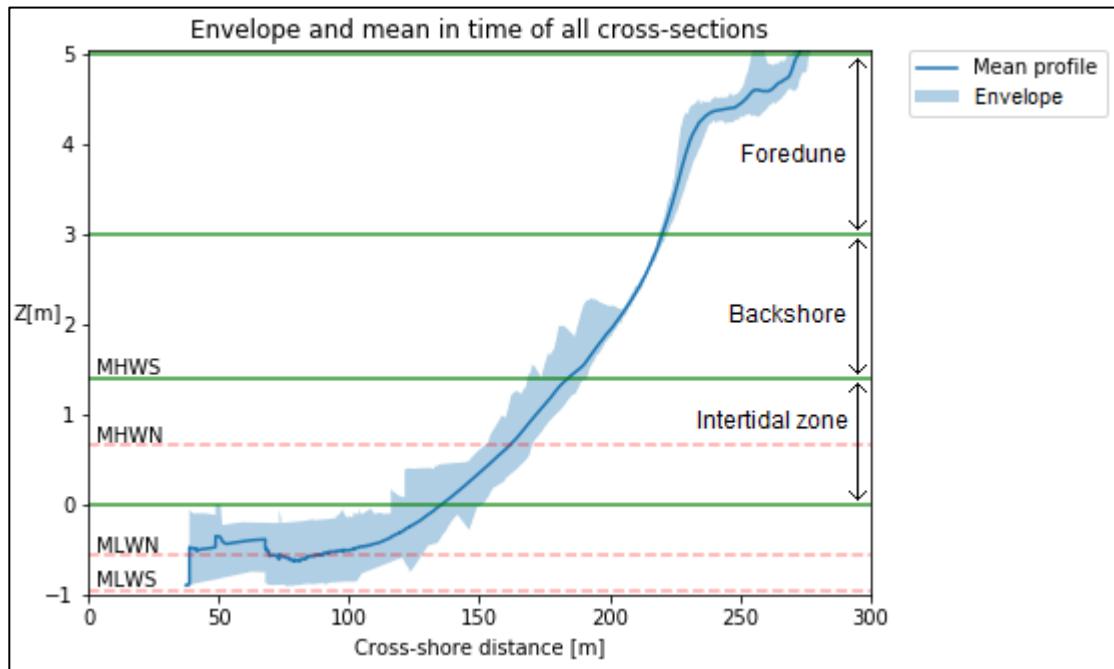


Figure 0-2: Mean in time and envelope of all cross-sections. The green lines divide the cross-section into intertidal zone, backshore and foredune. The lower region of the intertidal zone (below $z=0$) is discarded due to low data quality. Red dotted lines indicate various water levels.

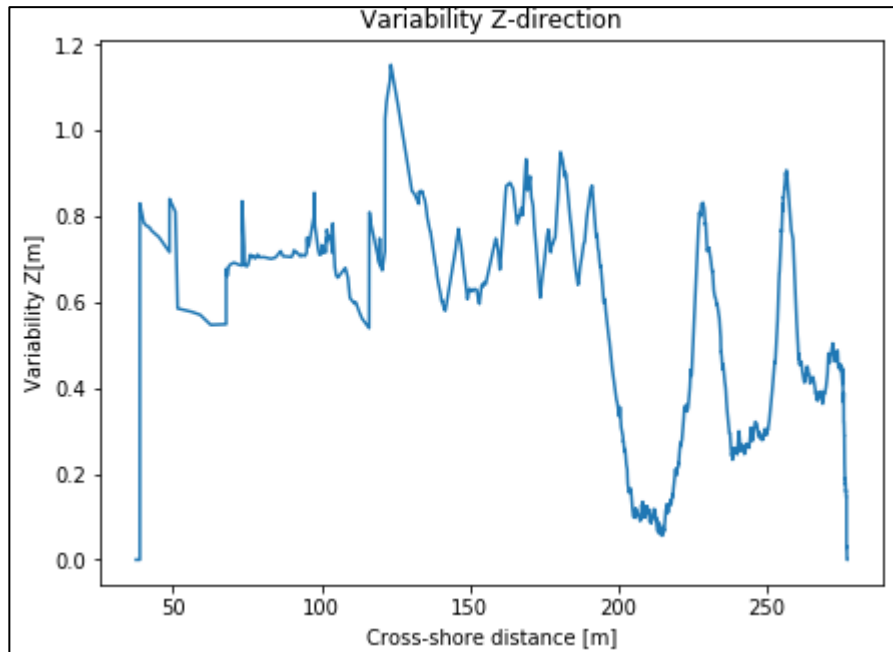


Figure 0-3: Variability plot of the beach at the chosen location.

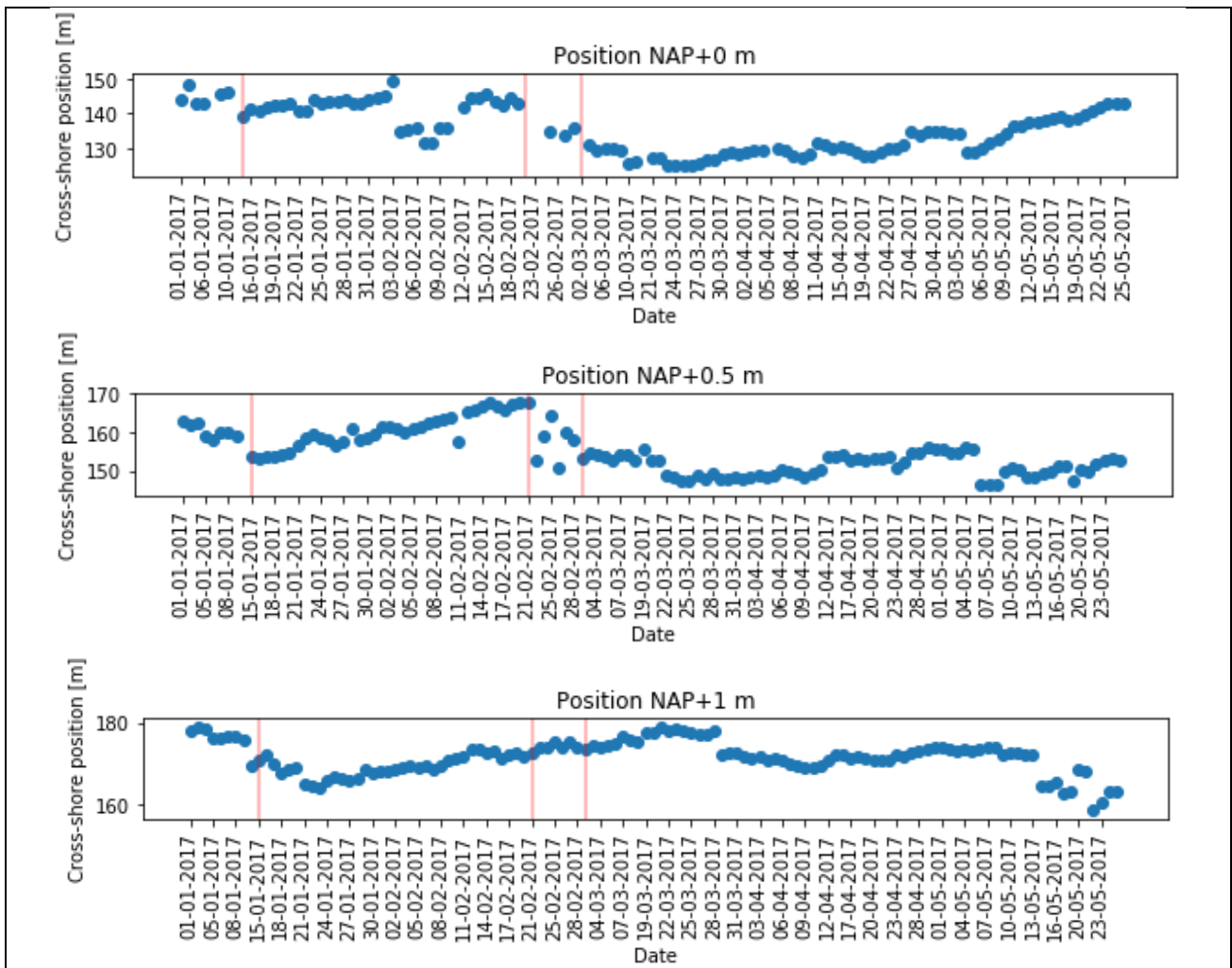


Figure 0-4: Cross-shore position of various elevation levels. Red lines indicate storms.

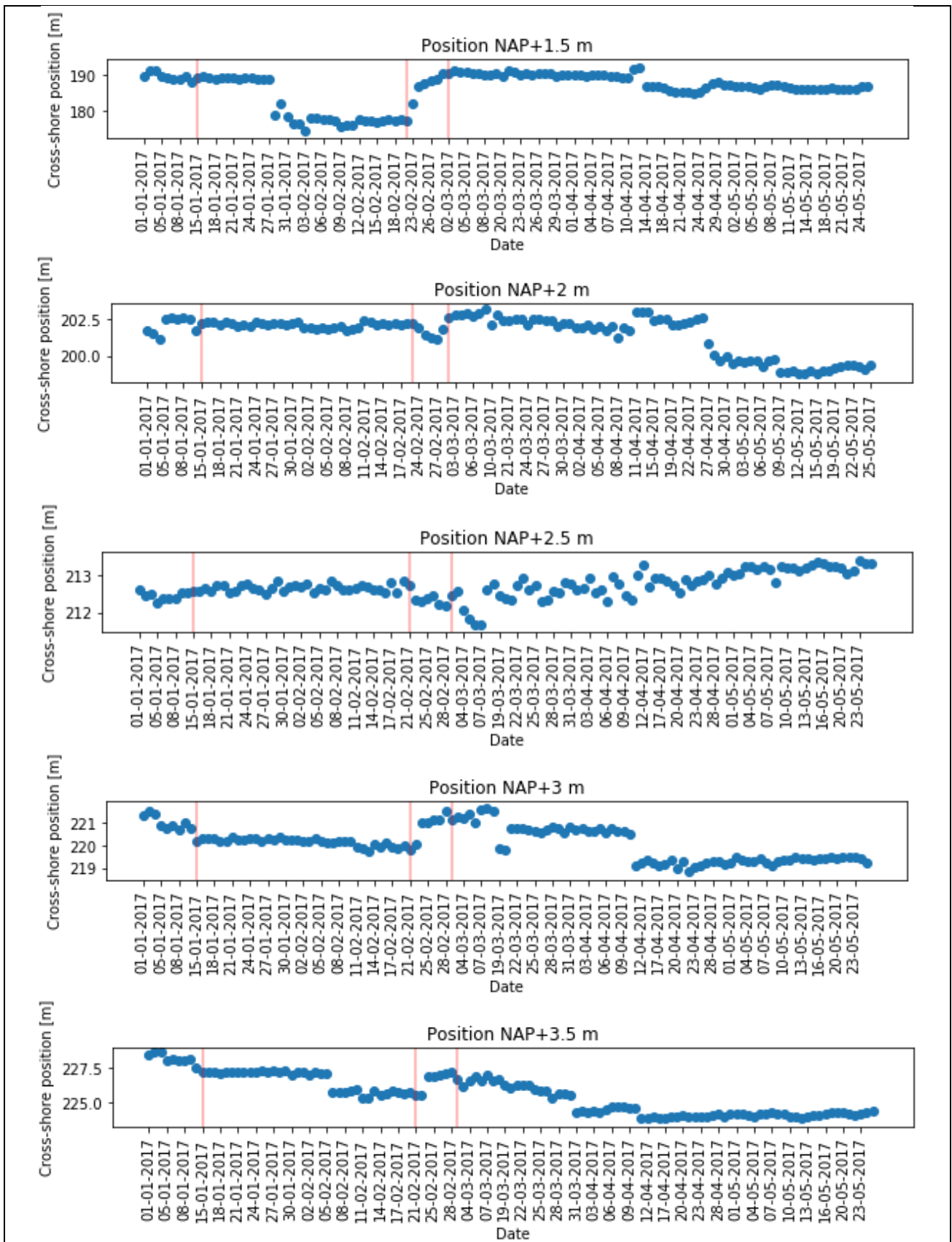


Figure 0-5: Cross-shore position of various elevation levels. Red lines indicate storms.

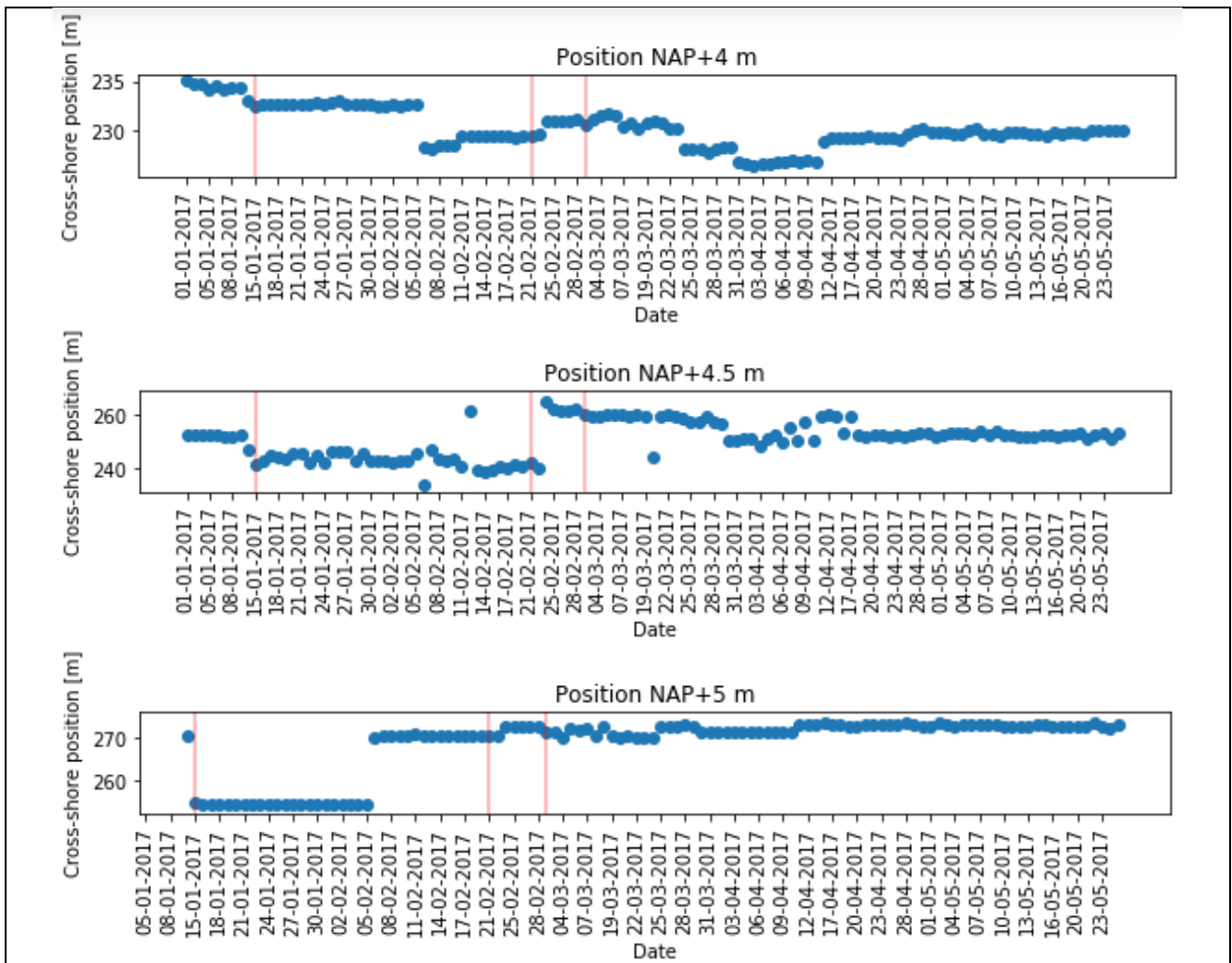


Figure 0-6: Cross-shore position of various elevation levels. Red lines indicate storms

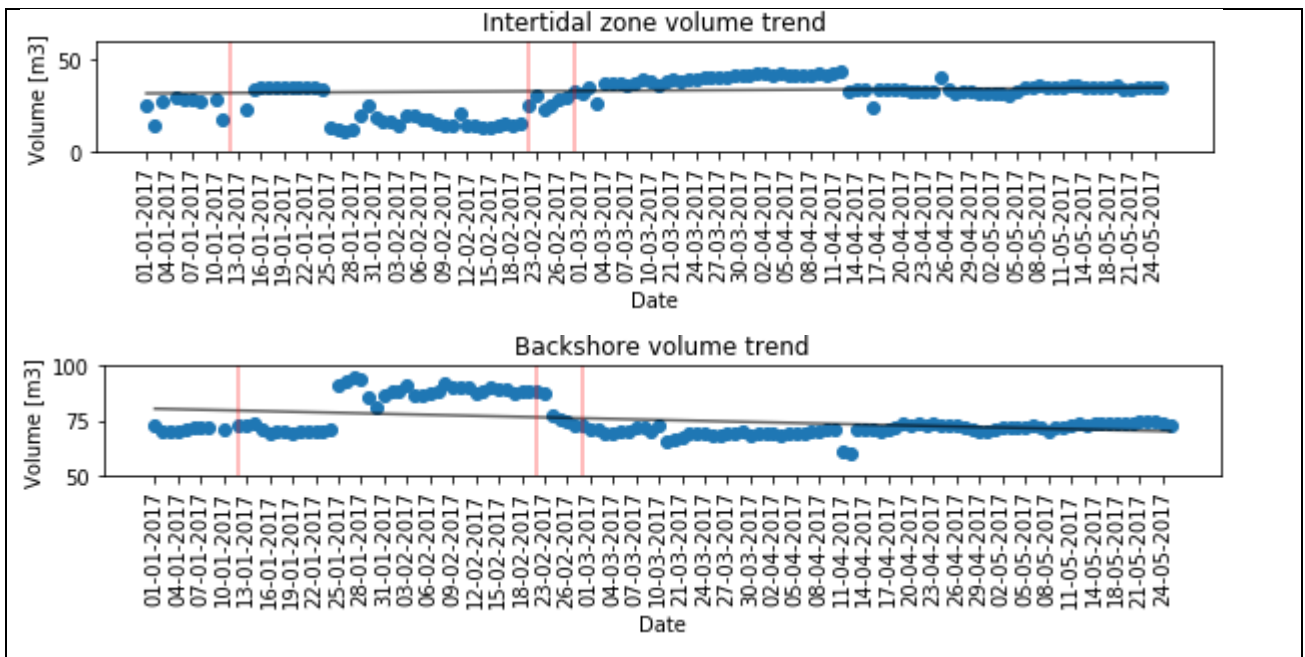


Figure 0-7: Volume distributions of the intertidal zone and backshore. Red lines indicate storms. Black line indicates the linear trend.

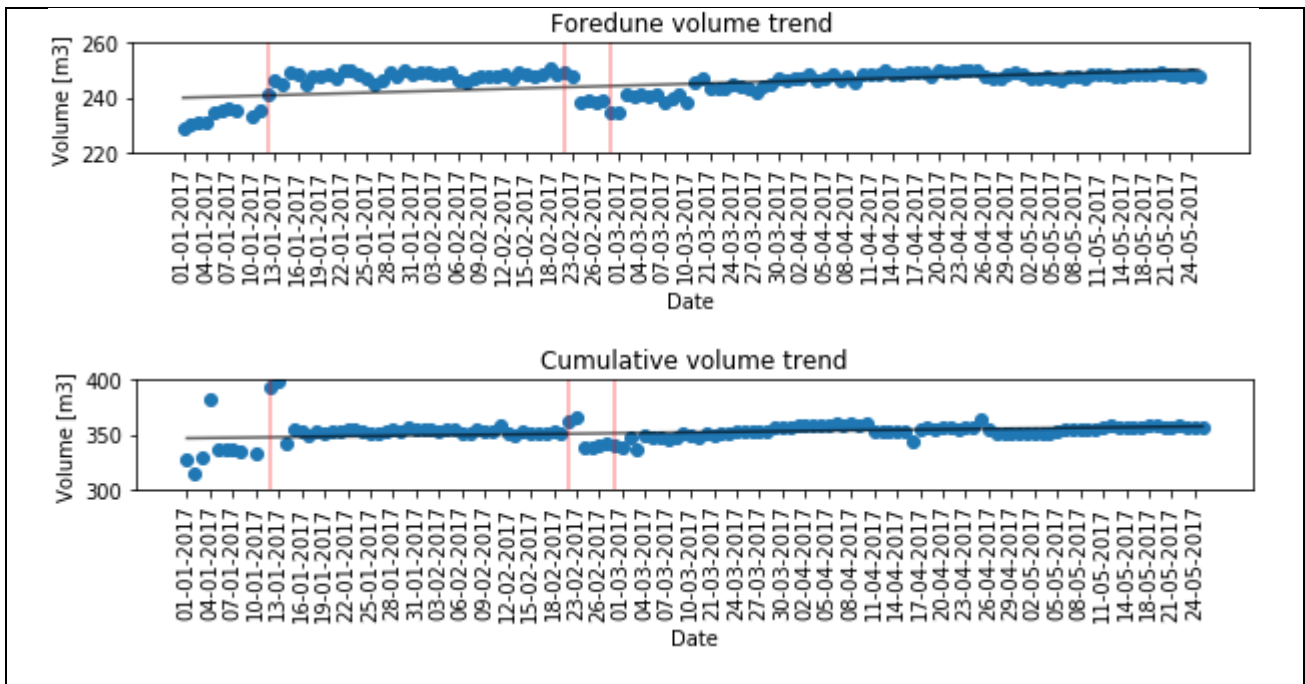


Figure 0-8: Volume distributions of the foredune and the cross-sectional total. Red lines indicate storms. Black line indicates the linear trend.

Region	R ² value
Intertidal zone	0.0023
Backshore	0.063
Foredune	0.15
Cumulative	0.034

Table 0-1: R² values for the plotted linear trends.

Region	Peak frequency [cycles/day]	Cycle time [days]
Intertidal zone	0.015	67
Backshore	0.0075	134
Foredune	0.015	67
Cumulative	0.015	67

Table 0-2: Results of Fourier analysis on the volume signals.

Variable	Peak frequency [cycles/day]	Cycle time [days]
Wave height	0.020689	48
Wave direction	0.006896	145
Wave period	0.020689	48
Wind velocity	0.041678	24
Wind direction	0.020839	48
Tide	1.931126	0.52

Table 0-3: Results of Fourier analysis on the boundary conditions.

Mapping sub-annual beach growth using terrestrial laser scanning: Appendix A: Individual analysis results transects 2-4.

Region	Wave height	Wave period	Wave direction	Wind velocity	Wind direction	Tide
Intertidal zone	No significant correlations					
Backshore						
Foredune						
Cumulative						

Table 0-4: Significant (p -value < 0.05) Pearson correlation coefficients between volumetric change rates and boundary conditions. No significant correlations were found.

Region	Pearson's correlation coefficient.
Intertidal zone – Backshore	-0.54
Intertidal zone – Foredune	-0.85
Backshore – Foredune	0.35

Table 0-5: Significant (p -value < 0.05) Pearson correlation coefficients between volumetric change rates per zone of interest.

Transect 3.

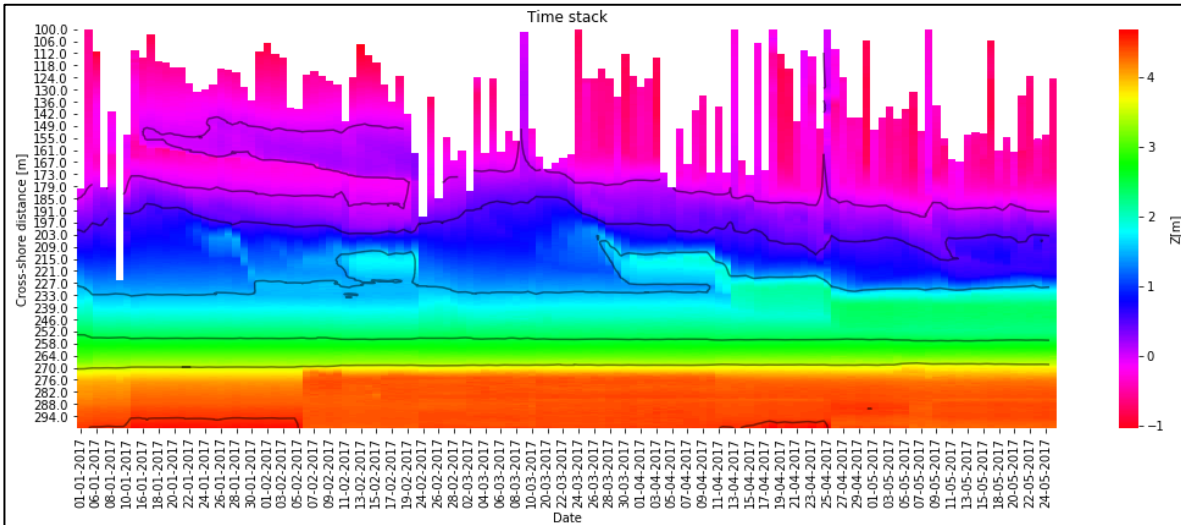


Figure 0-9: Time stack of all cross-sections. Colour scale represents elevation. Contour lines have been added in black, at NAP +0 m., NAP+0.5 m., NAP+1.5 m., NAP+2.5 m., NAP+3.5 m. and NAP +4.5 m.

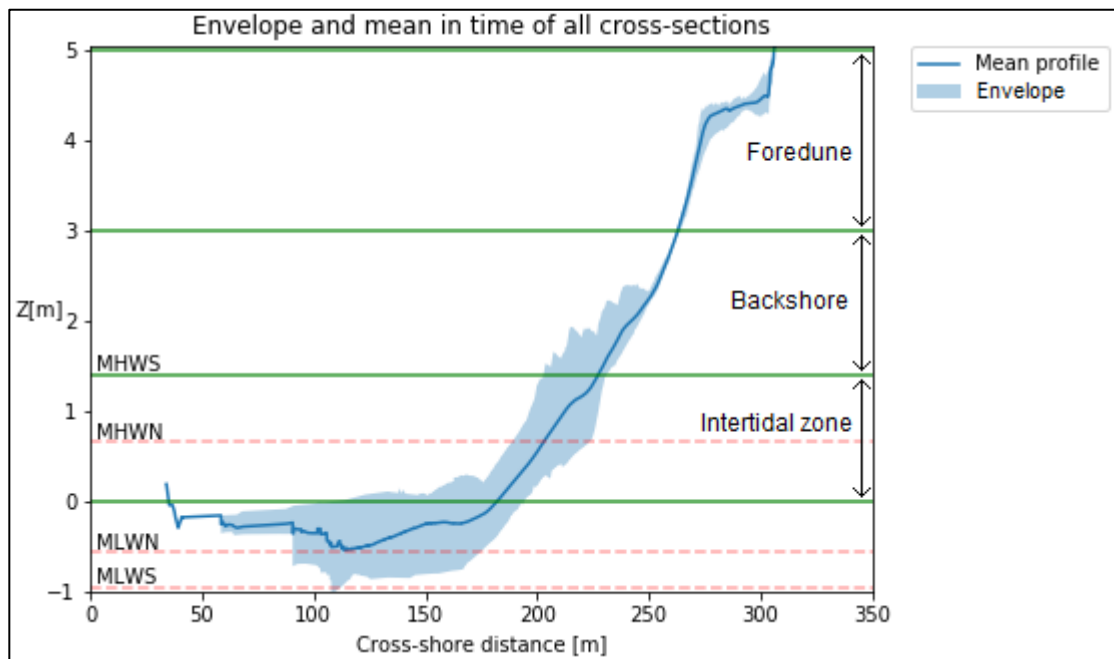


Figure 0-10: Mean in time and envelope of all cross-sections. The green lines divide the cross-section into intertidal zone, backshore and foredune. The lower region of the intertidal zone (below $z=0$) is discarded due to low data quality. Red dotted lines indicate various water levels.

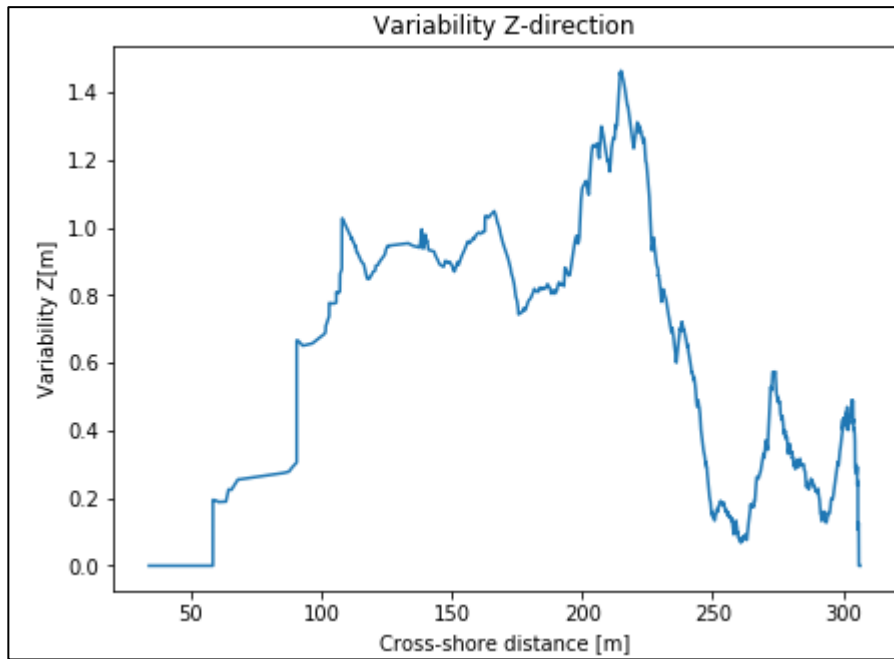


Figure 0-11: Variability plot of the beach at the chosen location.

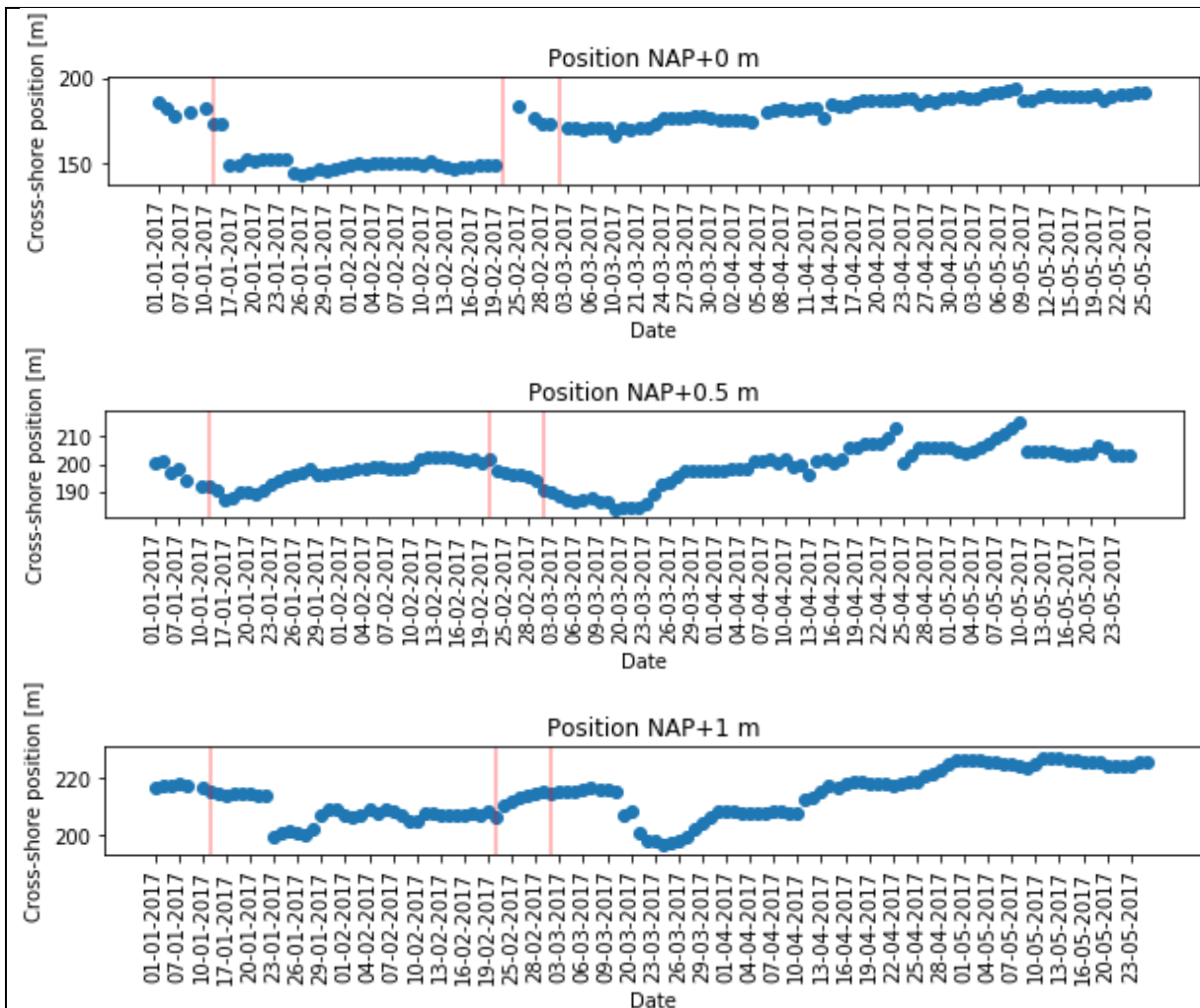


Figure 0-12: Cross-shore position of various elevation levels. Red lines indicate storms.

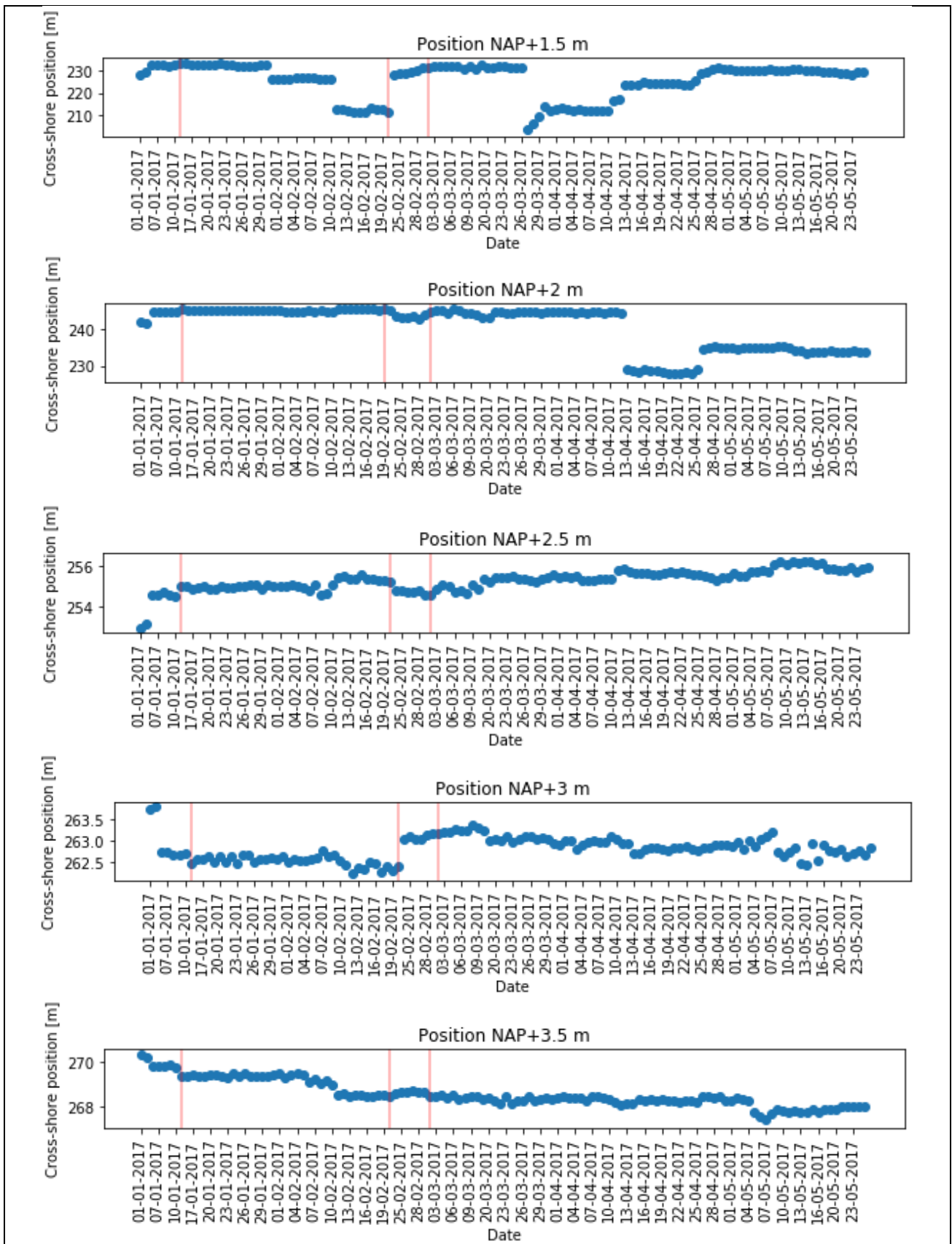


Figure 0-13: Cross-shore position of various elevation levels. Red lines indicate storms.

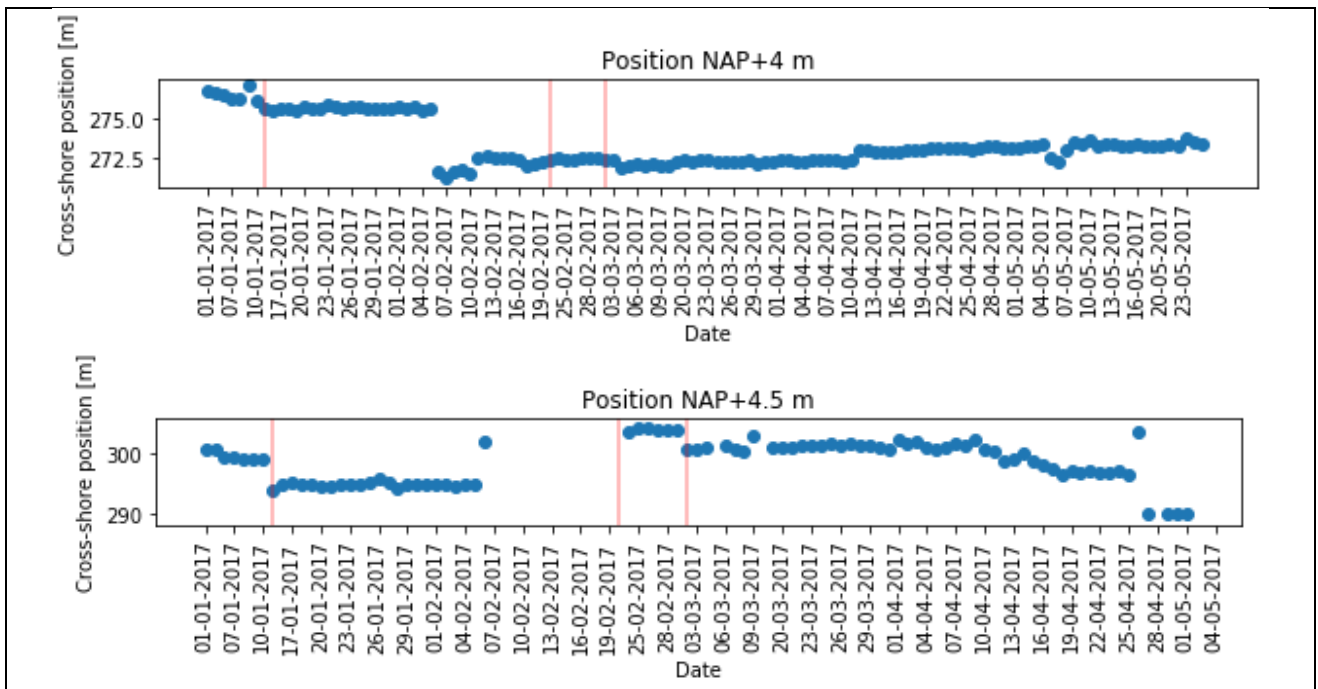


Figure 0-14: Cross-shore position of various elevation levels. Red lines indicate storms.

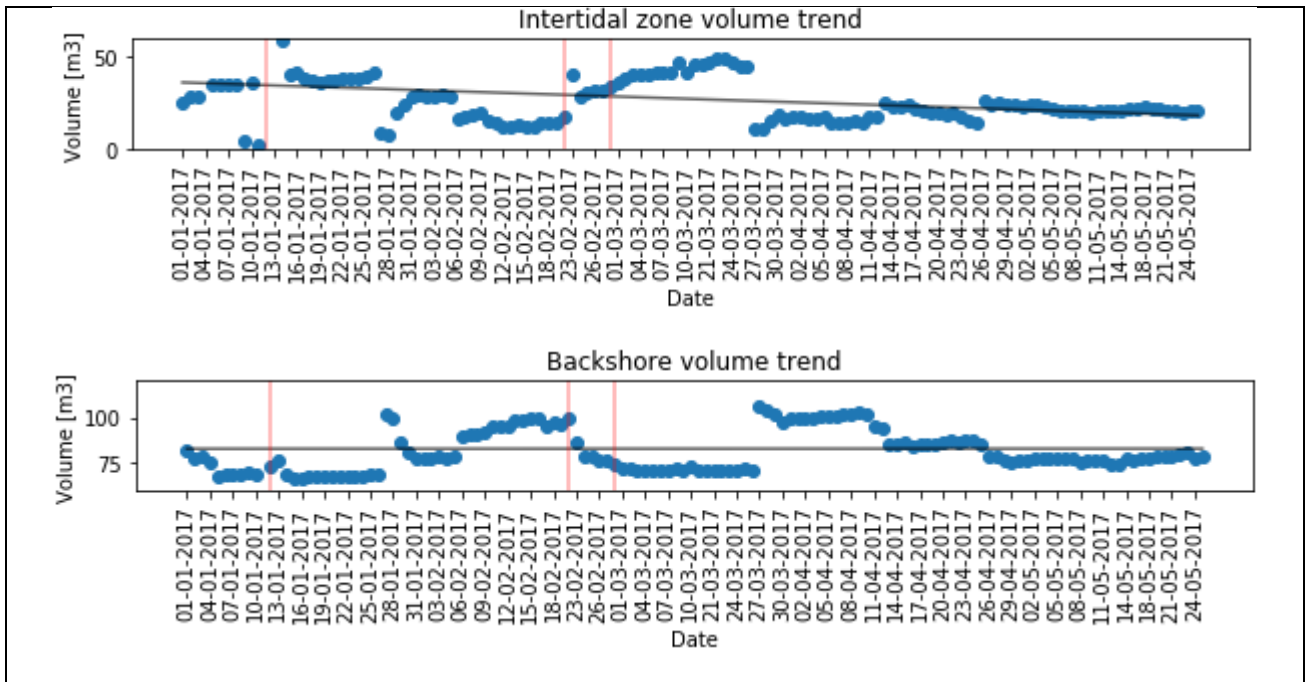


Figure 0-15: Volume distributions of the intertidal zone and backshore. Red lines indicate storms. Black line indicates the linear trend.

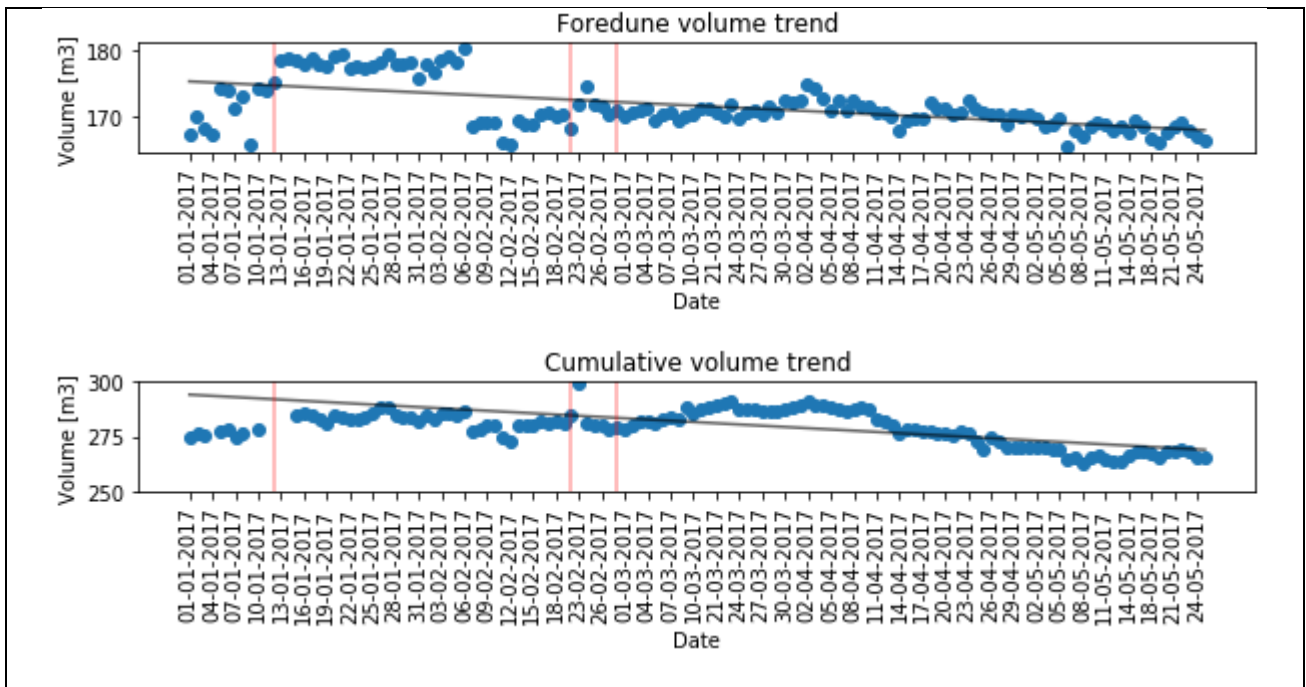


Figure 0-16: Volume distributions of the foredune and the cross-sectional total. Red lines indicate storms. Black line indicates the linear trend.

Region	R ² value
Intertidal zone	0.13
Backshore	10 ⁻⁶
Foredune	0.34
Cumulative	0.17

Table 0-6: R² values for the plotted linear trends.

Region	Peak frequency [cycles/day]	Cycle time [days]
Intertidal zone	0.022	45
Backshore	0.022	45
Foredune	0.015	67
Cumulative	0.015	67

Table 0-7: Results of Fourier analysis on the volume signals.

Variable	Peak frequency [cycles/day]	Cycle time [days]
Wave height	0.020689	48
Wave direction	0.006896	145
Wave period	0.020689	48
Wind velocity	0.041678	24
Wind direction	0.020839	48
Tide	1.931126	0.52

Table 0-8: Results of Fourier analysis on the boundary conditions.

Mapping sub-annual beach growth using terrestrial laser scanning: Appendix A: Individual analysis results transects 2-4.

Region	Wave height	Wave period	Wave direction	Wind velocity	Wind direction	Tide
Intertidal zone						
Backshore						
Foredune	0.19		0.19		0.20	
Cumulative						

Table 0-9: Significant (p -value < 0.05) Pearson correlation coefficients between volumetric change rates and boundary conditions.

Region	Pearson's correlation coefficient.
Intertidal zone – Backshore	-0.70
Intertidal zone – Foredune	
Backshore – Foredune	

Table 0-10: Significant (p -value < 0.05) Pearson correlation coefficients between volumetric change rates per zone of interest.

Transect 4.

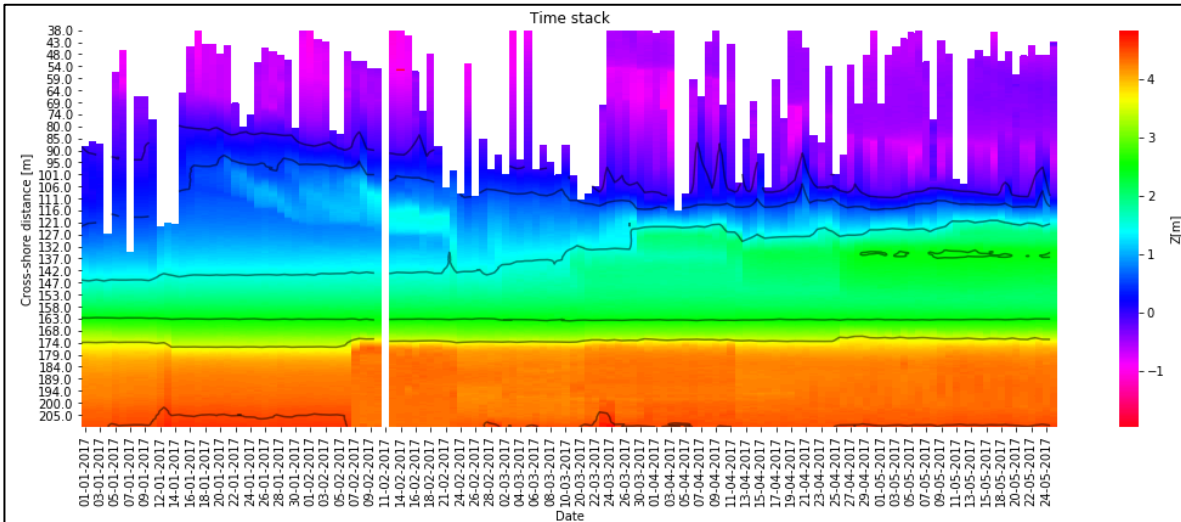


Figure 0-17: Time stack of all cross-sections. Colour scale represents elevation. Contour lines have been added in black, at NAP +0 m., NAP+0.5 m., NAP+1.5 m., NAP+2.5 m., NAP+3.5 m. and NAP +4.5 m.

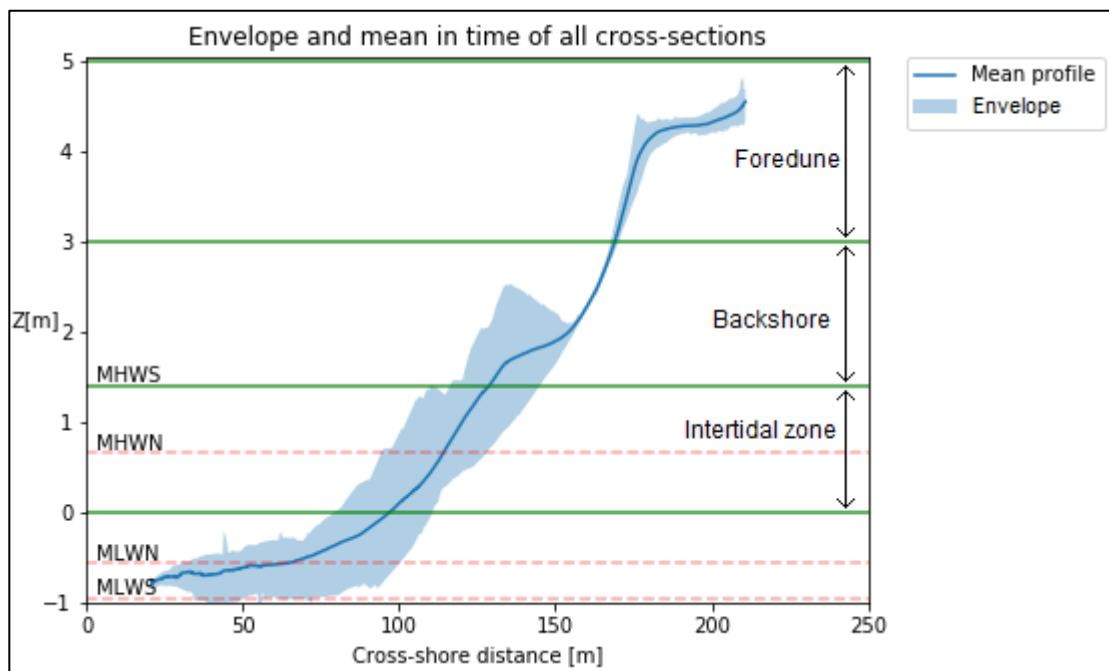


Figure 0-18: Mean in time and envelope of all cross-sections. The green lines divide the cross-section into intertidal zone, backshore and foredune. The lower region of the intertidal zone (below $z=0$) is discarded due to low data quality. Red dotted lines indicate various water levels.

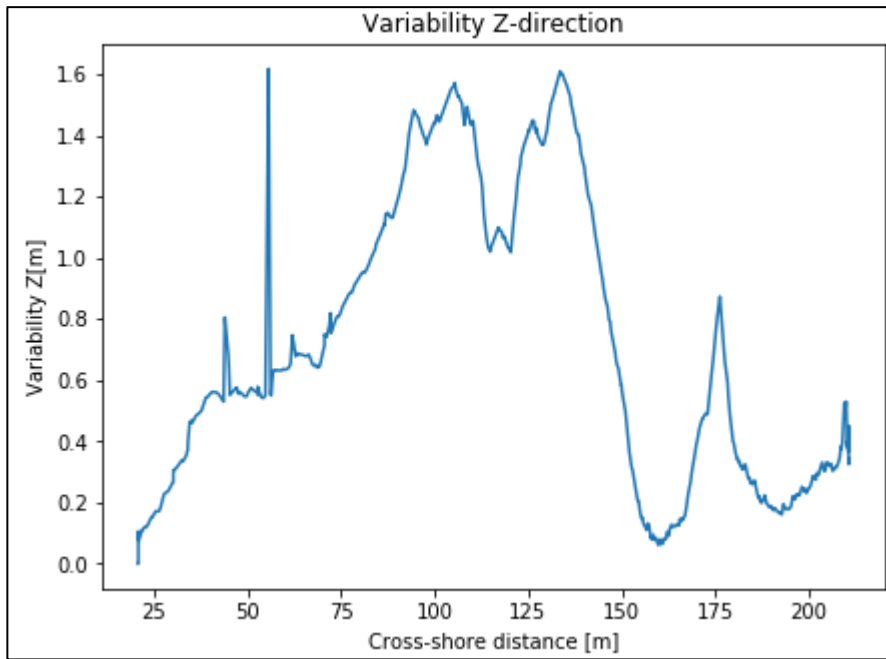


Figure 0-19: Variability plot of the beach at the chosen location.

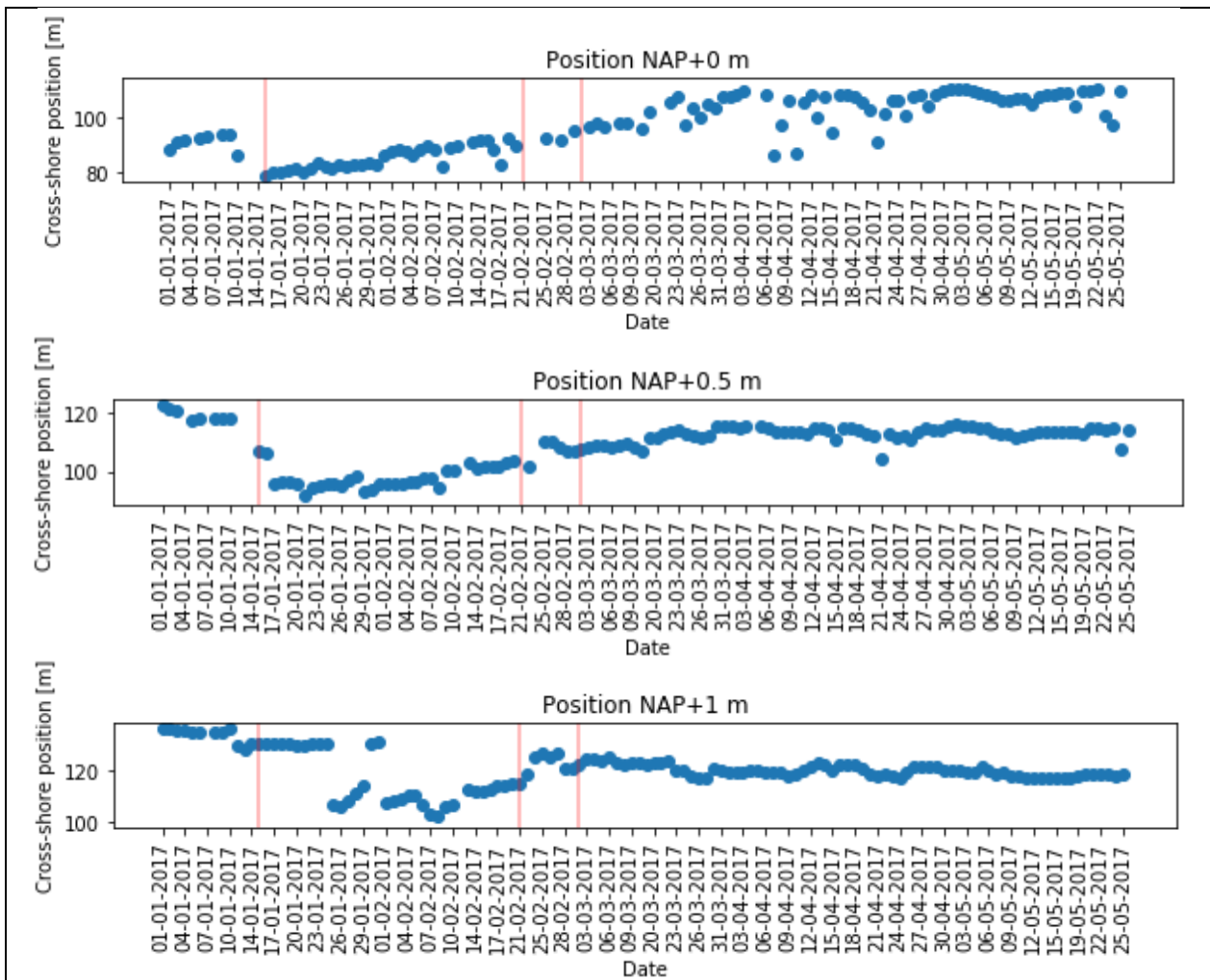


Figure 0-20: Cross-shore position of various elevation levels. Red lines indicate storms.

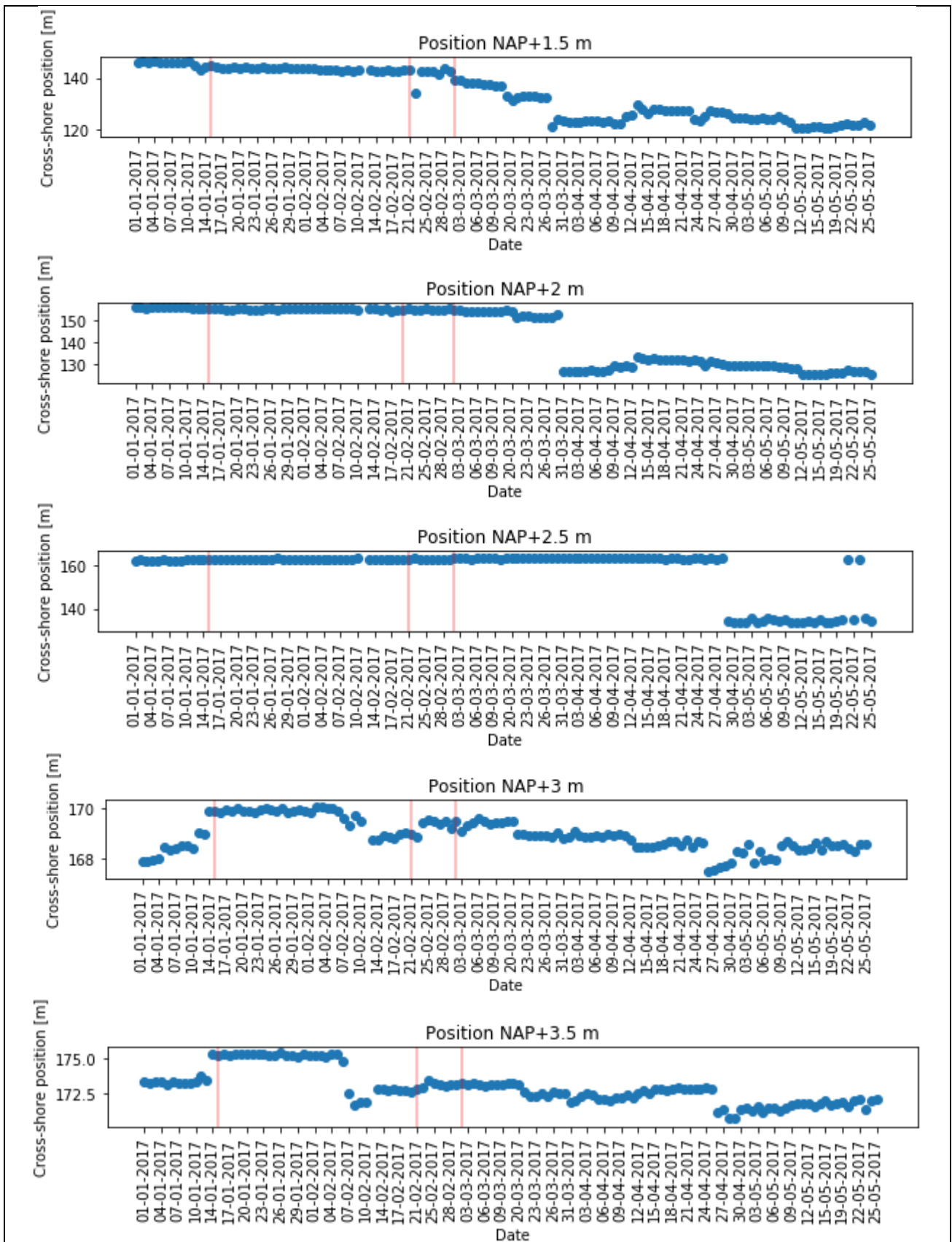


Figure 0-21: Cross-shore position of various elevation levels. Red lines indicate storms.

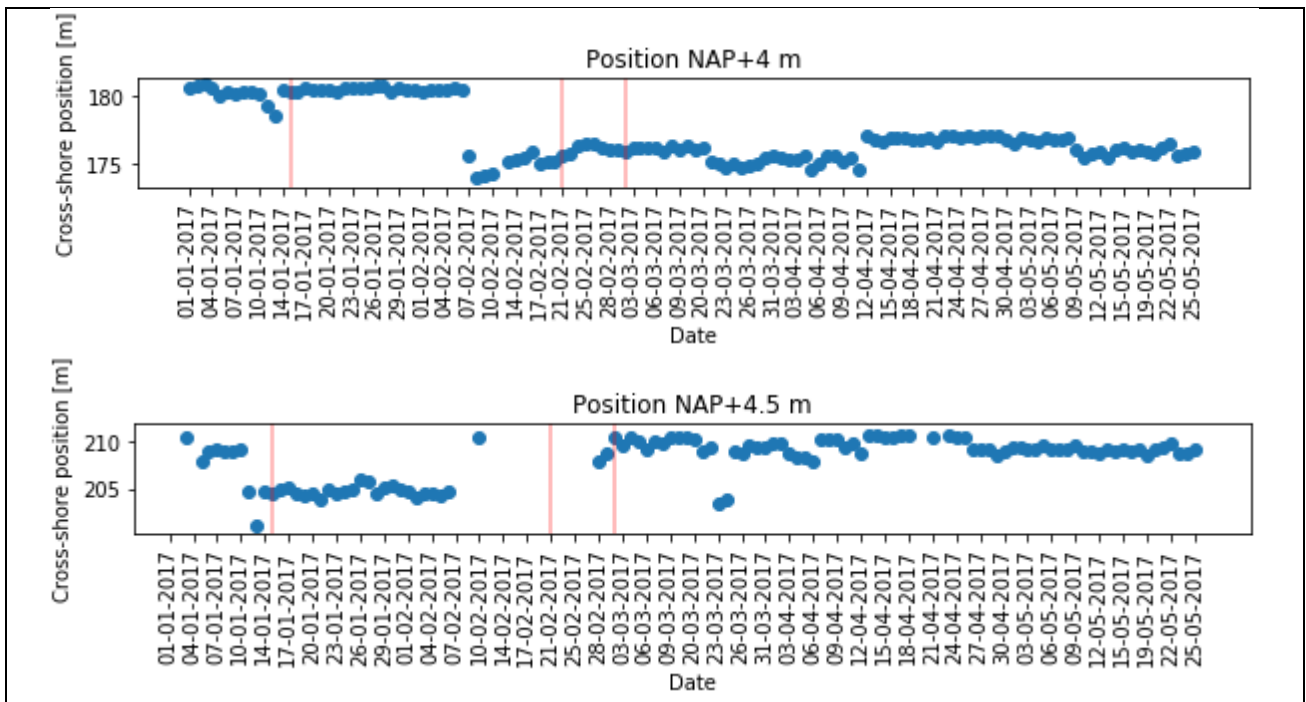


Figure 0-22: Cross-shore position of various elevation levels. Red lines indicate storms.

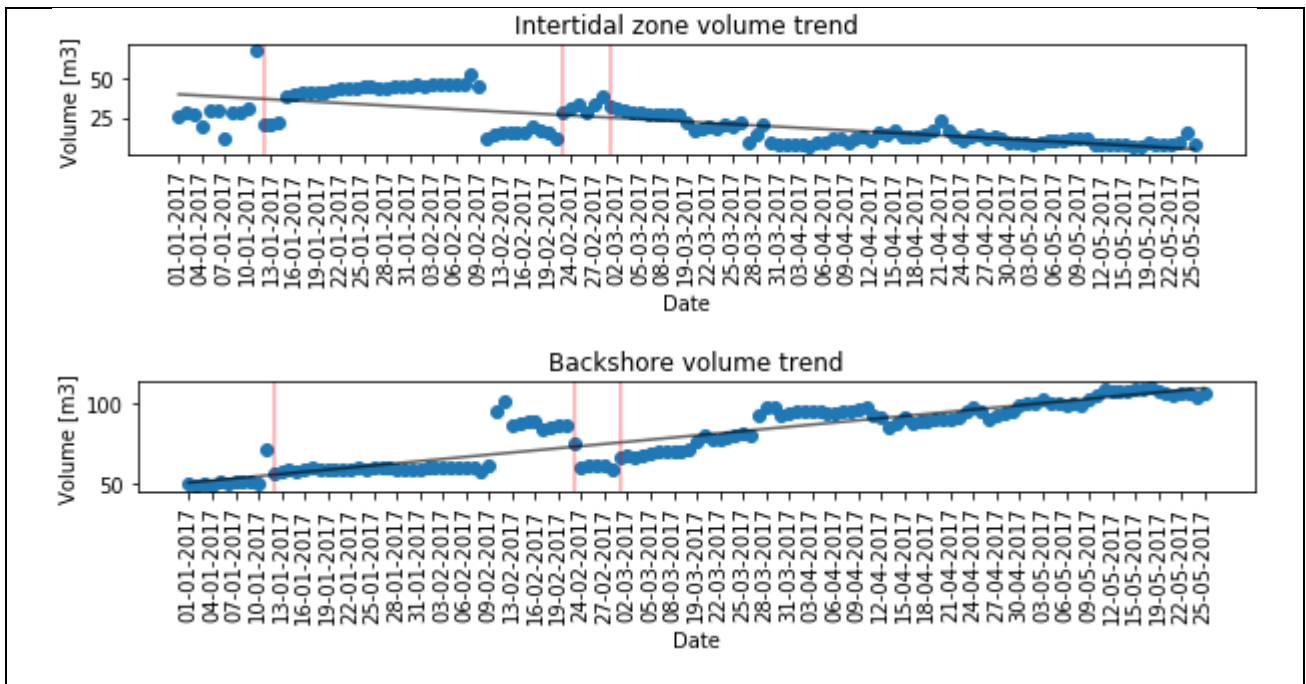


Figure 0-23: Volume distributions of the intertidal zone and backshore. Red lines indicate storms. Black line indicates the linear trend.

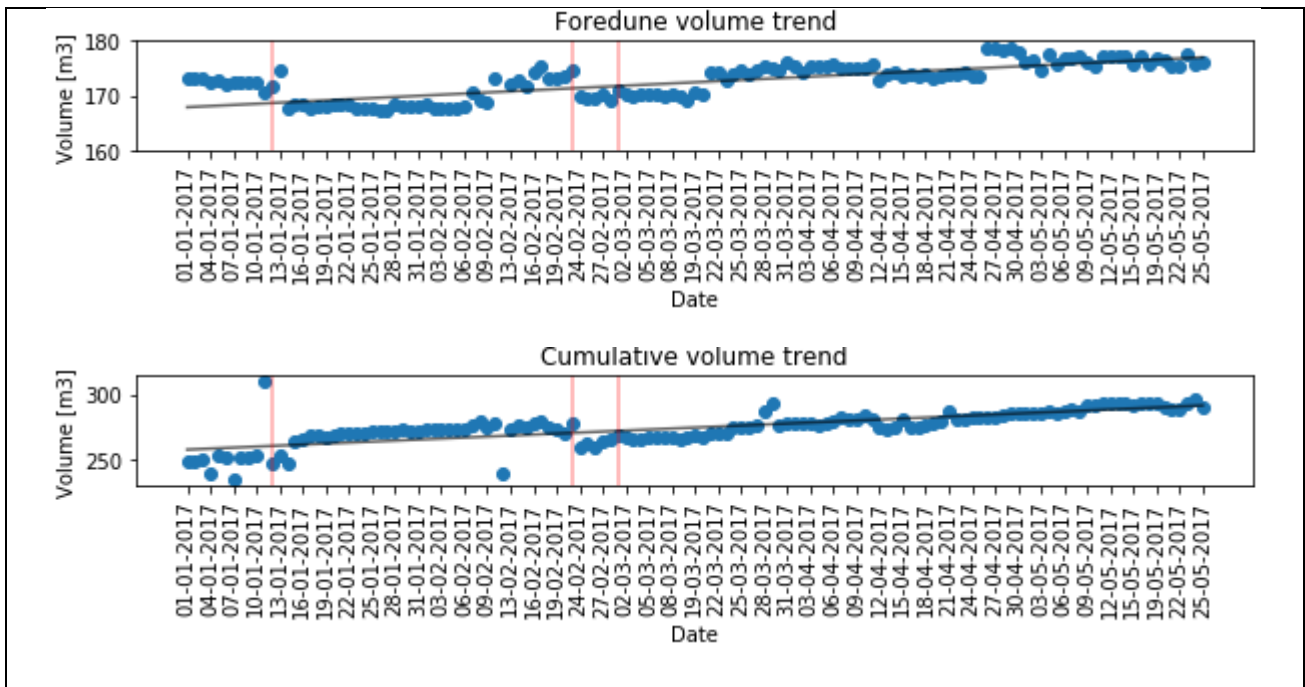


Figure 0-24: Volume distributions of the foredune and the cross-sectional total. Red lines indicate storms. Black line indicates the linear trend.

Region	R ² value
Intertidal zone	0.55
Backshore	0.83
Foredune	0.24
Cumulative	0.59

Table 0-11: R2 values for the plotted linear trends.

Region	Peak frequency [cycles/day]	Cycle time [days]
Intertidal zone	0.0075	133
Backshore	0.0075	133
Foredune	0.0075	133
Cumulative	0.0075	133

Table 0-12: Results of Fourier analysis on the volume signals.

Variable	Peak frequency [cycles/day]	Cycle time [days]
Wave height	0.020689	48
Wave direction	0.006896	145
Wave period	0.020689	48
Wind velocity	0.041678	24
Wind direction	0.020839	48
Tide	1.931126	0.52

Table 0-13: Results of Fourier analysis on the boundary conditions.

Mapping sub-annual beach growth using terrestrial laser scanning: Appendix A: Individual analysis results transects 2-4.

Region	Wave height	Wave period	Wave direction	Wind velocity	Wind direction	Tide
Intertidal zone						
Backshore			-0.20			
Foredune						
Cumulative						

Table 0-14: Significant (p -value < 0.05) Pearson correlation coefficients between volumetric change rates and boundary conditions.

Region	Pearson's correlation coefficient.
Intertidal zone – Backshore	
Intertidal zone – Foredune	
Backshore – Foredune	-0.25

Table 0-15: Significant (p -value < 0.05) Pearson correlation coefficients between volumetric change rates per zone of interest.